

AD-A056 292

PENNSYLVANIA STATE UNIV UNIVERSITY PARK APPLIED RESE--ETC F/6 20/1  
DIFFRACTION EFFECTS OF BAFFLES ON ACOUSTIC DIRECTIVITY PATTERNS--ETC(U)  
NOV 77 W J HUGHES  
TM-77-304

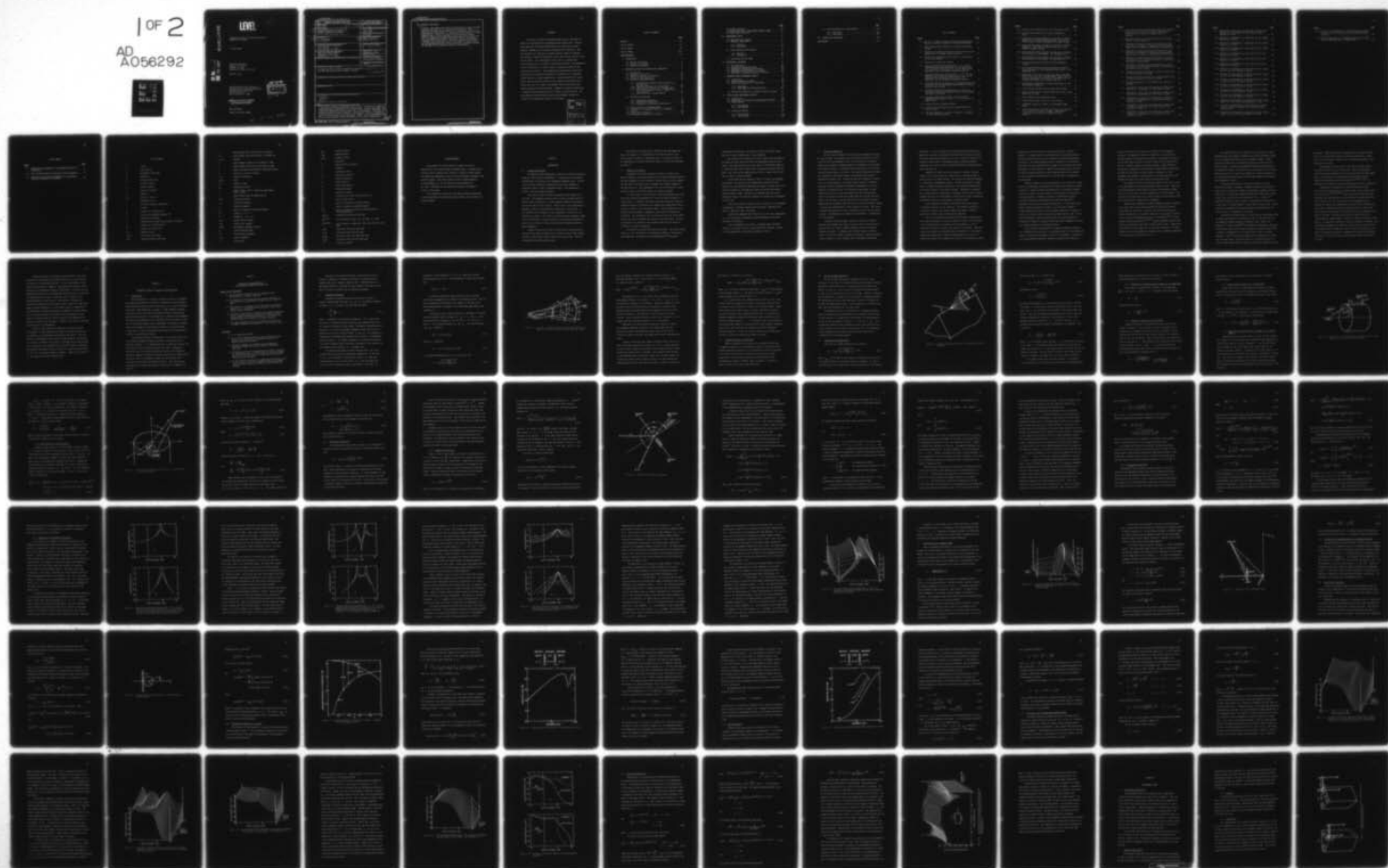
N00017-73-C-1418

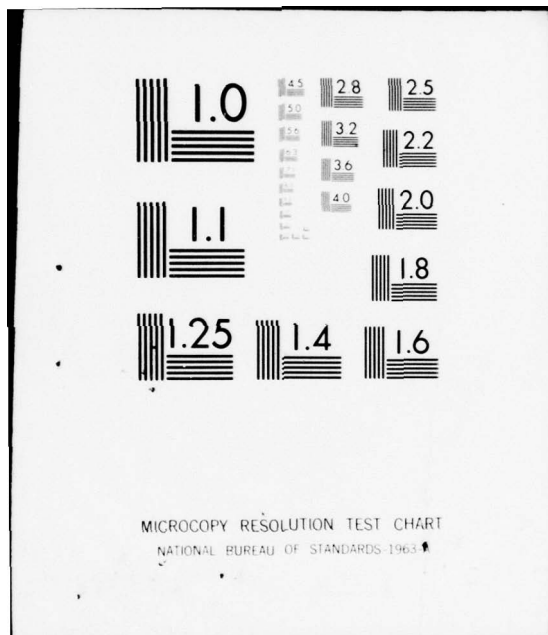
NL

UNCLASSIFIED

1 of 2

AD  
A056292







AD A 056292

LEVEL II

(12)  
B.S.

DIFFRACTION EFFECTS OF BAFFLES ON ACOUSTIC  
DIRECTIVITY PATTERNS

W. Jack Hughes

Technical Memorandum  
File No. TM 77-304  
November 12, 1977  
Contract No. N00017-73-C-1418

Copy No. 10

The Pennsylvania State University  
Institute for Science and Engineering  
APPLIED RESEARCH LABORATORY  
Post Office Box 30  
State College, PA 16801

DDC  
RECEIVED  
JUL 14 1978  
A

APPROVED FOR PUBLIC RELEASE  
DISTRIBUTION UNLIMITED

NAVY DEPARTMENT

NAVAL SEA SYSTEMS COMMAND

78 07 14 051

AD No. \_\_\_\_\_  
DDC FILE COPY

UNCLASSIFIED

SECURITY CLASSIFICATION OF THIS PAGE (When Data Entered)

14 REPORT DOCUMENTATION PAGE		9 READ INSTRUCTIONS BEFORE COMPLETING FORM
1. REPORT NUMBER TM-77-304	2. GOVT ACCESSION NO.	3. RECIPIENT'S CATALOG NUMBER Doctoral thesis
4. TITLE (and Subtitle) DIFFRACTION EFFECTS OF BAFFLES ON ACOUSTIC DIRECTIVITY PATTERNS.		5. TYPE OF REPORT & PERIOD COVERED Ph.D. Thesis March 1978
7. AUTHOR(s) W. Jack/Hughes		6. PERFORMING ORG. REPORT NUMBER TM 77-304
9. PERFORMING ORGANIZATION NAME AND ADDRESS Applied Research Laboratory P. O. Box 30 State College, PA 16801		8. CONTRACT OR GRANT NUMBER(s) N00017-73-C-1418
11. CONTROLLING OFFICE NAME AND ADDRESS Naval Sea Systems Command Department of the Navy Washington, D. C. 20362		10. PROGRAM ELEMENT, PROJECT, TASK AREA & WORK UNIT NUMBERS 11 12 Nov-77
14. MONITORING AGENCY NAME & ADDRESS (if different from Controlling Office)		12. REPORT DATE November 12, 1977
		13. NUMBER OF PAGES 171 pages & figures
		15. SECURITY CLASS. (of this report) Unclassified, Unlimited
		15a. DECLASSIFICATION/DOWNGRADING SCHEDULE
16. DISTRIBUTION STATEMENT (of this Report) Approved for public release, distribution unlimited, per NSSC (Naval Sea Systems Command), 12/22/77. 13 171P.		
17. DISTRIBUTION STATEMENT (of the abstract entered in Block 20, if different from Report)		
18. SUPPLEMENTARY NOTES		
19. KEY WORDS (Continue on reverse side if necessary and identify by block number) acoustics diffraction baffles Geometrical Theory of Diffraction		
20. ABSTRACT (Continue on reverse side if necessary and identify by block number) The acoustic diffraction phenomena which occur at the edges of a baffle is investigated both experimentally and theoretically. Various sharp-edged and cylindrical-edged baffles were constructed in which geometry, impedance, and structural resonances were controlled. Data were obtained as a function of incident pressure, angle of incidence, and frequency, using two transducers, one in the far field and one on the baffle surface. Also investigated is the effect of placing small scattering barriers at the edge of rigid baffle		

DD FORM 1473  
1 JAN 73

EDITION OF 1 NOV 65 IS OBSOLETE

UNCLASSIFIED

SECURITY CLASSIFICATION OF THIS PAGE (When Data Entered)

UNCLASSIFIED

SECURITY CLASSIFICATION OF THIS PAGE(When Data Entered)

20. ABSTRACT (Continued)

surfaces. The Geometrical Theory of Diffraction is used to develop a theoretical model for the calculation of patterns. Both Sommerfeld and Malyuzhinets diffraction coefficients are discussed along with the utilization of a transition region function to remove singularities. Patterns obtained with rigid baffle surfaces exhibited ripples in the insonified region while soft baffles gave rise to a smooth "bell-shaped" directivity pattern with highly attenuated diffraction fields. Asymmetric patterns resulted when a transducer was positioned close to one edge of a finite baffle. The good agreement obtained between theory and experiment confirms the validity of the Geometrical Theory of Diffraction.

UNCLASSIFIED

SECURITY CLASSIFICATION OF THIS PAGE(When Data Entered)

## ABSTRACT

The acoustic diffraction phenomena which occur at the edges of a baffle is investigated both experimentally and theoretically. Various sharp-edged and cylindrical-edged baffles were constructed in which geometry, impedance, and structural resonances were controlled. Data were obtained as a function of incident pressure, angle of incidence, and frequency, using two transducers, one in the far field and one on the baffle surface. Also investigated is the effect of placing small scattering barriers at the edge of rigid baffle surfaces. The Geometrical Theory of Diffraction is used to develop a theoretical model for the calculation of patterns. Both Sommerfeld and Malyuzhinets diffraction coefficients are discussed along with the utilization of a transition region function to remove singularities. Patterns obtained with rigid baffle surfaces exhibited ripples in the insonified region while soft baffles gave rise to a smooth 'bell-shaped' directivity pattern with highly attenuated diffraction fields. Asymmetric patterns resulted when a transducer was positioned close to one edge of a finite baffle. The good agreement obtained between theory and experiment confirms the validity of the Geometrical Theory of Diffraction.

ABSTRACT NO.	
DTIC	WFO Section <input checked="" type="checkbox"/>
DOC	OW Section <input type="checkbox"/>
UNANNOUNCED	<input type="checkbox"/>
JUSTIFICATION	
BY	
DISTRIBUTION AVAILABILITY CODES	
Dist.	AVAIL. UNCL. OR SPECIAL
A	



## TABLE OF CONTENTS

	<u>Page</u>
ABSTRACT . . . . .	iii
LIST OF FIGURES . . . . .	vii
LIST OF TABLES . . . . .	xii
LIST OF SYMBOLS . . . . .	xiii
ACKNOWLEDGEMENTS . . . . .	xvi
I. INTRODUCTION . . . . .	1
1.1 General Introduction . . . . .	1
1.2 Problem to be Studied . . . . .	2
1.3 Historical Background . . . . .	4
II. GEOMETRICAL THEORY OF ACOUSTICS AND DIFFRACTION . . . . .	11
2.1 Introduction . . . . .	11
2.2 Geometrical Acoustics . . . . .	13
2.3 Geometrical Theory of Diffraction . . . . .	17
2.4 The Law of Edge Diffraction . . . . .	18
2.5 Geometrical Spreading Factor . . . . .	18
2.5.1 Plane Wave or Cylindrical Wave Incident on a Straight Edge . . . . .	21
2.5.2 Plane Wave Incident on a Curved Edge . . . . .	21
2.5.3 Spherical Wave Incident on a Straight Edge . . . . .	22
2.5.4 Point Source Located on Axis of Symmetry of a Circular Baffle . . . . .	22
2.5.5 Point Source on a Circular Baffle . . . . .	24
2.6 Diffraction Coefficient . . . . .	27
2.6.1 Sommerfeld Coefficient . . . . .	28
2.6.2 Malyuzhinets Coefficient . . . . .	35
2.6.3 Comparison of Diffraction Coefficients . . . . .	38
2.7 Reflection From an Impedance Wedge . . . . .	46
2.8 Attenuation of Progressive Waves on an Impedance Surface . . . . .	50
2.9 Finite Size of Receiver . . . . .	50
2.10 Transmission Properties of a Baffle . . . . .	53

	<u>Page</u>
2.11 Baffle Vibration . . . . .	58
2.12 Diffraction From a Single-Edge Impedance Wedge . . . . .	61
2.13 Multi-Edge Diffraction . . . . .	71
III. EXPERIMENTAL SETUP . . . . .	77
3.1 Hydrophone and Projector . . . . .	77
3.2 Impedance Wedge Baffle . . . . .	77
3.2.1 Material . . . . .	78
3.2.2 Description . . . . .	78
3.3 Finite Rigid and Soft Baffles . . . . .	80
3.3.1 Material . . . . .	80
3.3.2 Description . . . . .	80
3.4 Scattering Bars and Rings . . . . .	83
IV. EXPERIMENTAL PROCEDURE . . . . .	86
4.1 Test Facilities . . . . .	86
4.2 Transmission Measuring System . . . . .	86
4.3 Experimental Technique and Procedure . . . . .	89
4.4 Hydrophone Position Relative to Surface . . . . .	90
4.5 Experimental Problems and Sources of Errors . . . . .	93
V. IMPEDANCE WEDGE EXPERIMENTAL RESULTS . . . . .	96
5.1 Introduction . . . . .	96
5.2 Surface Impedance of Baffle . . . . .	96
5.3 Directivity Patterns for a Sharp Edge . . . . .	99
5.3.1 Sharp Edge . . . . .	99
5.3.2 Sharp Edge With Scattering Strip . . . . .	103
5.4 Directivity Patterns for a Wedge of Finite Curvature . . . . .	103
VI. FINITE BAFFLE EXPERIMENTAL RESULTS . . . . .	109
6.1 Introduction . . . . .	109
6.2 Comparison of Theoretical and Experimental Results . . . . .	118
6.3 Planar Baffles . . . . .	122
6.3.1 Rigid Baffles . . . . .	122
6.3.2 Soft Baffles . . . . .	130
6.4 Cylindrical Baffles . . . . .	134
6.4.1 Rigid End-Cap . . . . .	134
6.4.2 Soft End-Cap . . . . .	134

	<u>Page</u>
6.5 Scattering Rings on a Rigid Surface . . . . .	141
6.5.1 Rigid Ring . . . . .	141
6.5.2 Soft Ring . . . . .	141
VII. SUMMARY AND CONCLUSIONS . . . . .	148
BIBLIOGRAPHY . . . . .	152

## LIST OF FIGURES

<u>Figure</u>		<u>Page</u>
2.1	Ray Tube. A Caustic Occurs at Those Points where One or Both of the Radii of Curvature of the Wavefront Vanish . .	15
2.2	Edge Diffracted Rays Formed by an Incident Ray Grazing an Edge . . . . .	19
2.3	Diffraction of Spherical Waves from a Point Source on the Symmetry Axis of a Right Circular Cylinder . . . . .	23
2.4	Geometry for Determining the Ray Path of a Point Source on a Circular Baffle . . . . .	25
2.5	Geometry for Diffraction Problems . . . . .	30
2.6	Calculated Directivity Patterns with $\phi = 0^\circ$ for the Sommerfeld Diffraction Coefficient for the Hard Edge in (a), and Keller's Coefficient for the Soft Edge in (b). Comparison is With and Without Transition Function . . . .	39
2.7	Calculated Directivity Patterns with $\phi = 30^\circ$ for the Sommerfeld Hard Diffraction Coefficient in (a), and the Sommerfeld Soft Diffraction Coefficient in (b). Comparison is With and Without Transition Function . . . .	41
2.8	Calculated Directivity Patterns of the Sommerfeld Hard (a) and Keller Soft (b) Diffraction Coefficients for Several Distances from the Edge . . . . .	43
2.9	Calculated Directivity Patterns with $\phi = 30^\circ$ as a Function of the Surface Impedance Using the Malyuzhinets Diffraction Coefficient . . . . .	45
2.10	Calculated Directivity Patterns with Both Surface Impedance Ratios Equal to $Z/\rho c = 1.5$ as a Function of Source Angle . . . . .	47
2.11	Reflection from an Impedance Wedge . . . . .	49
2.12	Circular Cross-Sectional Area of a Receiver Near the Baffle Surface . . . . .	52
2.13	Pressure Response of a Receiver of Radius $a$ Adjacent to a Soft and Rigid Surface . . . . .	54



<u>Figure</u>	<u>Page</u>
2.14 Insertion Loss Properties for a 1/8" Thick Layer of Air .	56
2.15 Insertion Loss Properties for Various Thickness of Steel . . . . .	59
2.16 Calculated Directivity Patterns as a Function of Surface Impedance for a Single Diffraction Edge. Point Source is Near Surface and Four Wavelengths from Edge (20 kHz). .	64
2.17 Calculated Directivity Patterns as a Function of Surface Impedance. Point Source is Near Surface and 12 Wavelengths from Edge (60 kHz) . . . . .	66
2.18 Calculated Directivity Patterns as a Function of Distance from the Edge on a Rigid Wedge. The Wavelength is 3" . .	67
2.19 Calculated Directivity Patterns as a Function of Distance from the Edge on a Soft Wedge. The Wavelength is 3" . . .	69
2.20 Calculated Directivity Patterns for Mixed Impedance Surfaces . . . . .	70
2.21 Calculated Far-Field Directivity Patterns for Various Source Positions on a Two-Dimensional Rigid Baffle. The Wavelength is 3" . . . . .	74
2.22 Comparison of the Directivity Patterns from a Four-Edge Model (solid line) and a Two-Edge Model (dashed line) for a Source Positioned in the Center of the Baffle (a) and One-Third Wavelength from the Right Edge (b) . . . . .	76
3.1 Wedge Baffle Configured to Study the Sharp Edge (a), and the Cylindrical Edge (b) . . . . .	79
3.2 Probe Mounting Assembly with the Rigid Square Baffle . . .	82
3.3 Cross-Sectional View of a Rigid Baffle with a Bar or Ring Mounted at its Edge . . . . .	85
4.1 Block Diagram of the Experimental Setup . . . . .	88
4.2 Standing Wave Formed in Front of a Soft Baffle . . . . .	92
5.1 Attenuation Along the Surface of the Impedance Wedge Baffle . . . . .	98
5.2 Directivity Patterns at 10 kHz and 20 kHz of a Transducer on the Surface of a Sharp 75° Wedge. Experimental (solid line) and Theoretical (dashed line) are Compared . . . . .	100

<u>Figure</u>	<u>Page</u>
5.3 Directivity Patterns at 30 kHz and 60 kHz of a Transducer on the Surface of a Sharp 75° Wedge. Experimental (solid line) and Theoretical (dashed line) are Compared . . . . .	101
5.4 Calculated Directivity Pattern Variation for Different Source to Surface Distances . . . . .	102
5.5 Comparison of Measured Directivity Patterns at 10 kHz and 20 kHz for a Sharp 75° Wedge With a Scattering Bar (dashed line) and Without a Scattering Bar (solid line) .	104
5.6 Comparison of Measured Directivity Patterns at 30 kHz and 60 kHz for a Sharp 75° Wedge With a Scattering Bar (dashed line) and Without a Scattering Bar (solid line) .	105
5.7 Comparison of Measured Directivity Patterns at 10 kHz and 20 kHz for a 30° Cylindrical Wedge of 6" Radius With and Without Scattering Bars . . . . .	106
5.8 Comparison of Measured Directivity Patterns at 30 kHz and 60 kHz for a 30° Cylindrical Wedge of 6" Radius With and Without Scattering Bars . . . . .	107
6.1 Measured Directivity Patterns for a Center Mounted Probe on Different Baffles at 20 kHz . . . . .	110
6.2 Measured Directivity Patterns for a Center Mounted Probe on Different Baffles at 15 kHz and 30 kHz . . . . .	113
6.3 Hydrophone Responses for Soft Baffles as a Function of Position . . . . .	117
6.4 Experimental (solid line) and Theoretical (dashed line) Patterns for a Hydrophone on a Rigid Disk at 20 kHz . . .	119
6.5 Experimental (solid line) and Theoretical (dashed line) Patterns for a Hydrophone on a Soft Disk at 20 kHz . . . .	120
6.6 Experimental (solid line) and Theoretical (dashed line) Patterns for a Hydrophone on a Rigid End-Cap, Rigid Cylinder at 20 kHz . . . . .	121
6.7 Experimental (solid line) and Theoretical (dashed line) Patterns for a Hydrophone on a Rigid End-Cap, Soft Cylinder at 20 kHz . . . . .	123
6.8 Experimental (solid line) and Theoretical (dashed line) Patterns for a Hydrophone on a Soft End-Cap, Soft Cylinder at 20 kHz . . . . .	124

<u>Figure</u>	<u>Page</u>
6.9 Experimental (solid line) and Theoretical (dashed line) Patterns for a Hydrophone on a Soft End-Cap, Rigid Cylinder at 20 kHz . . . . .	125
6.10 Patterns of a Hydrophone on a Rigid Disk (a) and a Rigid Square (b) at 15 kHz . . . . .	127
6.11 Patterns of a Hydrophone on a Rigid Disk (a) and a Rigid Square (b) at 20 kHz . . . . .	128
6.12 Patterns of a Hydrophone on a Rigid Disk (a) and a Rigid Square (b) at 30 kHz . . . . .	129
6.13 Patterns of a Hydrophone on a Soft Disk (a) and a Soft Square (b) at 15 kHz . . . . .	131
6.14 Patterns of a Hydrophone on a Soft Disk (a) and a Soft Square (b) at 20 kHz . . . . .	132
6.15 Patterns of a Hydrophone on a Soft Disk (a) and a Soft Square (b) at 30 kHz . . . . .	133
6.16 Patterns of a Hydrophone on a Rigid End-Cap with a Rigid (a) and a Soft (b) Cylinder at 15 kHz . . . . .	135
6.17 Patterns of a Hydrophone on a Rigid End-Cap with a Rigid (a) and a Soft (b) Cylinder at 20 kHz . . . . .	136
6.18 Patterns of a Hydrophone on a Rigid End-Cap with a Rigid (a) and a Soft (b) Cylinder at 30 kHz . . . . .	137
6.19 Patterns of a Hydrophone on a Soft End-Cap with a Rigid (a) and a Soft (b) Cylinder at 15 kHz . . . . .	138
6.20 Patterns of a Hydrophone on a Soft End-Cap with a Rigid (a) and a Soft (b) Cylinder at 20 kHz . . . . .	139
6.21 Patterns of a Hydrophone on a Soft End-Cap with a Rigid (a) and a Soft (b) Cylinder at 30 kHz . . . . .	140
6.22 Patterns of a Hydrophone on a Rigid Disk (a) and a Rigid Square (b) with a Steel Scattering Bar at 20 kHz . . . . .	142
6.23 Patterns of a Hydrophone on a Rigid End-Cap on a Rigid (a) and a Soft (b) Cylinder with a Steel Scattering Ring at 20 kHz . . . . .	143
6.24 Patterns of a Hydrophone on a Rigid Disk (a) and a Rigid Square (b) with a Soft Scattering Bar at 20 kHz . . . . .	144

<u>Figure</u>	<u>Page</u>
6.25 Patterns of a Hydrophone on a Rigid End-Cap with a Rigid (a) and a Soft (b) Cylinder with a Soft Scattering Ring at 20 kHz . . . . .	145
6.26 Pattern Comparisons for a Hydrophone Mounted Near a Rigid and Soft Scattering Bar on a Rigid Square . . . . .	147

## LIST OF TABLES

<u>Table</u>		<u>Page</u>
2.1	Principles and Advantages of the Geometrical Theory of Diffraction . . . . .	12
3.1	List of Baffle Geometries and Their Surface Impedances. . .	84
6.1	Diffraction Lobe Level and Beamwidth for a Hydrophone Centrally Positioned on the Baffle . . . . .	115



## LIST OF SYMBOLS

$Q$	a point
$c$	sound velocity
$dS$	incremental path length
$A$	amplitude
$d\sigma$	cross-sectional area
$\rho$	distance, density
$\rho_c$	caustic distance
$\rho_e$	radius of curvature
$s$	distance
$\phi(Q)$	phase at a point $Q$
$k$	wavenumber ( $= \omega/c$ )
$\omega$	circular frequency (radians/sec)
$P$	pressure
$P_R$	pressure of a reflected ray
$j$	positive unit imaginary number, $\sqrt{-1}$
$R_\xi$	reflection coefficient
$\xi$	angle between incident ray and normal to surface
$P_d$	pressure of a diffracted ray
$P_i$	pressure of incident ray
G.F.	geometric factor
$D(\phi, \phi')$	diffraction coefficient
$D'(\phi)$	slope-diffraction coefficient

$\phi$	angle between plane and direction of observer
$\phi'$	angle between plane and direction of incident ray
$\ell, r, R$	distance
$\beta$	angle between incident ray and tangent to edge
$\delta$	angle between diffracted ray and normal to edge
$\theta$	angle of incidence from normal of insonified surface
$a$	radius of a circle or cylinder
$x, y, z$	Cartesian coordinates
$\phi_T, \phi_S$	angle
$\ell_p$	primary ray path
$\ell_d$	diffracted ray path
$\eta$	quantity where $(2-\eta)\pi$ equals the wedge angle (also $= 2\Phi/\pi$ )
$\Phi$	angle between plane and wedge bisector
$F(x)$	transition function
$\tau, t$	integration variable
$L$	distance parameter
$a^+$	measure of distance from shadow boundary
$N^+$	integer of 0 or 1
$N^-$	integer of -1, 0, or 1
$C(x)$	Fresnel cosine integral
$S(x)$	Fresnel sine integral
$\Psi_\phi(\alpha)$	Malyuzhinets impedance function
$\theta_\pm$	grazing Brewster angle
$\rho_c$	characteristic impedance
$Z, Z_\pm$	surface impedance
$\sigma$	surface area

$P_{ave}$	average pressure
$P_{max}$	maximum pressure
$m_1, m_2$	impedance ratios
$\lambda$	wavelength
$J_0$	Bessel function of order 0
$f$	frequency
$h$	thickness of plate
$c_B$	bending wave velocity
$\mu$	Poisson contraction
$\lambda_E$	Young's modulus
$c_p$	plate sound velocity
$\lambda_B$	bending wavelength
$f_r$	resonance frequency
$P_o$	pressure due to direct and reflected rays
$P_t$	total pressure field
$\phi_r$	angle of reflection ray shadow boundary
$\phi_i$	angle of incident ray shadow boundary
$P/P_o$	ratio of pressure received with baffle present to free-field pressure
$D_s(\phi, \rho)$	Sommerfeld Diffraction Coefficient
$P_i^{(R), (L)}$	field incident at right, (R), and left, (L), edge
$P_i^{(RB), (LB)}$	field incident at right-back, (RB), and left-back, (LB), edge
$P_R(\phi)$	diffracted field from right edge
$P_L(\phi)$	diffracted field from left edge
$P_{RB}(\phi)$	diffracted field from right-back edge
$P_{LB}(\phi)$	diffracted field from left-back edge
$H$	height of cylinder



## ACKNOWLEDGEMENTS

With pleasure the author wishes to express his sincere appreciation to his thesis advisor, Professor Eugen J. Skudrzyk and to Professor Paul M. Kendig and Dr. Francis H. Fenlon for their helpful discussions and suggestions, and for their encouragement throughout this research program. The author would also like to thank Professor William Thompson, Jr. for his support and encouragement and Mr. Dale J. Sackrider for his assistance during the experimental portion of this study.

This research was supported by the Applied Research Laboratory at The Pennsylvania State University under contract with the Naval Sea Systems Command.

## CHAPTER I

### INTRODUCTION

#### 1.1 General Introduction

The generation and propagation of sound in an infinite isovelocity medium is a well understood phenomenon. If boundaries are introduced, standing waves, diffraction, and transmission phenomena arise. Diffraction is usually considered a modification that sound undergoes in passing the edges of rigid or impedance bodies. This phenomenon is present in any wave analysis problem.

The study of sound in fluids has generally been limited to air and water. The impedance characteristics of these two media differ by several orders of magnitude. A large impedance mismatch is required to obtain good rigid or soft surfaces. Since air has a low characteristic impedance, almost any solid material constitutes a rigid surface. A soft surface is very difficult, if not impossible, to achieve in air. Conversely, in water, a soft surface is easily produced, whereas a rigid surface is difficult to achieve because the characteristic impedance of water is only a factor of thirty less than that of materials with the highest impedance.

Because of the relative ease of testing, most investigations of diffraction have been performed in air on objects such as rigid spheres, cylinders, disks, square plates, cubes, and circular cones. Very few investigations have been made in water.

The literature contains various theories, both approximate and exact, but because of the complexities of diffraction theory, their validity must be checked by experimental data. Of special interest is the approximate but powerful Geometrical Theory of Diffraction developed by Keller.<sup>15</sup>

### 1.2 Problem to be Studied

Transducer arrays, which typically consist of several piezoelectric elements, are usually positioned in a support mechanism (baffle). The array designer is often troubled by the fact that the array elements near the edge of the baffle have an asymmetrically higher response in the edge direction. This phenomenon is due to the diffraction of sound around the edge of the baffle nearest the transducer element.

It is the object of this research to obtain experimental data that define the diffraction phenomena for a source (receiver) mounted on a finite baffle. In addition, directivity patterns computed by using the Geometrical Theory of Diffraction are compared with experimental data to check the validity of the theoretical model. Various baffles were constructed in which geometry, impedance, and structural resonances are controlled. Two transducers, one in the far field and one on the baffle surface, are used to generate and to monitor the sound field. The data are obtained as a function of the incident pressure and the angle of incidence for various frequencies.

The thesis is divided into three main sections. The first section, Chapter II, is a description of the Geometrical Theory of Diffraction. Both Sommerfeld, see Reference 19, and Malyuzhinets<sup>28</sup> diffraction

coefficients are discussed. The effect of using a transition region function to remove singularities is also discussed.

The second section, Chapters III and IV, deals with the design of the wedge and finite baffles and with the experimental setup and procedure. The wedge baffle has two long, sharp  $75^\circ$  diffraction edges and a cylindrical edge, each of which can be acoustically isolated from the other. The finite baffle geometries are a disk, a square, and the end-cap of a short, circular cylinder.

In the third section, Chapters V and VI, the data are presented and analyzed. An analysis for the wedge baffle requires only the inclusion of one diffraction edge since the purpose of these tests is to check the validity of the Geometrical Theory of Diffraction using a single diffraction edge. Data were also gathered using the curved cylindrical edge of the structure; however, the theory was not developed for this case.

Each finite baffle was tested in both a rigid and a soft impedance configuration. Although extensive data were taken, comparison with theory is limited to only a few cases.

Chapter VII summarizes the results for all the cases investigated, i.e., for all baffles, frequencies, surface impedances, and source positions on the baffle.

Also investigated is the effect of placing small scattering barriers at the edge of rigid or semi-rigid baffle surfaces. Results of these experiments are included in Chapters V and VI.

### 1.3 Historical Background

The first wave treatment of the diffraction phenomenon was given by Young in 1800. He postulated that the diffracted waves are of local character since the phenomenon occurs in the vicinity of the shadow boundary (the geometric boundary between the illuminated and the shadow areas behind an object). Cylindrical wave fields appear to be emitted from the straight edge of the object. The observed interference fringes are explained as interference between the diffracted wave and the unobstructed incident wave. Fresnel rejected this treatment of diffraction as a local phenomenon. Utilizing concepts implicit in Huygens' principle, Fresnel considered the diffraction phenomenon to be a consequence of interference due to an infinitely large number of waves radiated from virtual sources distributed over the entire aperture surface (the aperture surface being subdivided into circular half-wave zones). On the basis of the wave theory which he developed, Fresnel demonstrated the remarkable fact that there is an axial brightspot behind a circular disk illuminated by a point source on its axis. This result is historically important in that it provided a test of the wave theory of light. Lord Rayleigh later observed it acoustically. See Reference 27 for more detail.

Kirchhoff utilized Huygens' principle to derive an integral equation that expresses the value of the wave field at points within a region of space in terms of assumed boundary values on the surface bounding the region. In general, this integral equation cannot be solved. In the early 1900's, Rubinowicz and Kottler reduced Kirchhoff's surface integral to a line integral which considerably facilitates



calculation. It also illustrates the differences between physical and geometrical acoustics and indicates that diffraction around an obstacle arises from waves which originate at its rim. As shown in Reference 34, Kirchhoff's theory fails to distinguish between different boundary conditions (e.g., hard or soft) and between differently shaped obstacles having the same rim.

Sommerfeld in 1896 was the first person to develop a rigorous solution for the diffraction of a plane wave by a rigid half-plane (a special case of the wedge problem). His solution has long been regarded as a milestone in mathematical physics. He used an extension of image theory to deduce an integral solution for this problem and showed that his solution reduces to the Fresnel integral. MacDonald, by applying the classical method of separation of variables, was the first to obtain complete solutions for the problems of diffraction of plane, cylindrical, and spherical waves by a rigid wedge of arbitrary angle.

Since Sommerfeld's analysis, diffraction theory has received considerable attention in the literature. The inherent difficulty of the subject, however, has severely limited the number of possible geometries for which exact solutions may be obtained.

Most of the classical scattering and diffraction problems which have been solved exactly are those in which the surface of the obstacle can be identified with a coordinate surface belonging to a set of coordinates for which the scalar wave equation is separable. There are eleven such systems of coordinates given in Reference 30. The prolate spheroid may range from a slightly elongated sphere to a thin rod. Spence and Granger<sup>42</sup> have presented the results of calculations in these

coordinates for the scattering of a plane sound wave by a prolate spheroid. A rigorous theory of the diffraction of plane sound waves by circular disks and apertures can be obtained by using oblate spheroidal coordinates. The limiting spheroid may be considered as an infinitely thin disk, while the hyperboloid may be taken as an infinitely thin plane containing a circular aperture. Spence<sup>40</sup> has developed exact solutions for sound at normal incidence on oblate spheroids which can be applied to cases in which the disk radius is of the same order of magnitude as the wavelength.

Numerical results for the sound pressure on the surface of a rigid disk of zero thickness for perpendicular incidence has also been obtained by Wiener.<sup>47</sup> Spence<sup>41</sup> compares the predictions of Kirchhoff's approximation with those of the exact theory for the problem of diffraction by a circular aperture. Numerical solutions of steady-state acoustic radiation problems have been applied by Copley<sup>5</sup> and Schenck<sup>36</sup> to essentially three distinct integral formulations: (1) The Simple Source Method, adapted from potential theory; (2) the Surface Helmholtz Integral Equation, obtained from the integral expression for pressure in the field in terms of surface pressure and normal velocity; and (3) the Interior Helmholtz Integral Relation, where the surface pressure is determined by making the integral vanish identically throughout the source free volume enclosed by the vibrating surface.

Quite arbitrary baffle shapes and impedance boundary conditions can be handled with this method. An alternative method is the Geometrical Theory of Diffraction developed by Keller.<sup>15</sup> This method, in contrast to the integral-equation approach, becomes increasingly more useful and

accurate as the size of the structure, relative to the wavelength, increases. The Geometrical Theory of Diffraction is an extension of classical geometrical acoustics which permits a description not only of the reflection and refraction of acoustic waves but their diffraction as well. Classical geometric acoustics provides a simple method for describing the propagation and scattering of high-frequency sound waves. According to this theory, acoustic energy is regarded as a local phenomenon that depends on the character of the scattering body in the immediate vicinity of the point where the scattering occurs.

The Geometrical Theory of Diffraction admits a new class of rays to the description of scattering phenomena, diffracted rays. These rays are produced whenever high-frequency acoustic waves impinge on edges, corners, or tips, or are incident tangentially on curved surfaces. Once the diffraction coefficient for an edge is known, the description of the diffracted field is a simple matter of geometry.

Complex baffle geometries and mixed impedance boundary conditions can be dealt with by this method provided the required diffraction coefficients can be deduced. Moreover, the theory has been used to analyze diffraction by a cylinder of arbitrary cross section,<sup>12</sup> diffraction by a smooth three-dimensional object of any shape,<sup>16,24</sup> and other complex diffraction problems.<sup>13,17,50</sup> Excellent agreement between these results and previously known exact results has been found. Although the fields deduced in this manner are not the exact solutions of the field equations, they are presumably the leading terms of asymptotic expansions of such solutions for large values of  $k$ .



The Geometrical Theory of Diffraction for an aperture at small wavelengths has been compared in Reference 14 with the Kirchhoff method, its two customary modifications, and W. Braunbek's method. Keller generally concluded that the geometrical theory is as good or better than the others. Hutchins and Kouyoumjian<sup>9</sup> describe an application of the Geometrical Theory of Diffraction to the calculation of the far-zone radiation pattern of a linear array mounted in a rigid rectangular box. The theoretical patterns obtained by this method compare very favorably with experimental results.

Literature concerned with theoretical analyses of various diffraction problems is abundant. Barakat<sup>2</sup> studied the diffraction of plane waves by an elliptic cylinder via expansions in Mathieu functions. Diffraction of a plane small amplitude sound wave incident upon a semi-infinite thin elastic plate was investigated by G. L. Lamb, Jr.<sup>20</sup> Lyamshev<sup>26</sup> obtained an exact solution for the problem of diffraction of a plane wave in a moving medium by a semi-infinite elastic plate. Horton and Karal<sup>7</sup> investigated the problem of plane wave diffraction by the convex surface of a paraboloid of revolution.

Diffraction of sound around a circular disk was investigated using the Maggi transformation for distances not far off the axis, and near the geometrical shadow boundary by Primakoff, Klein, Keller, and Garstensen.<sup>34</sup> Again, Twersky<sup>44,45</sup> considered the nonspecular reflection of plane waves from certain surfaces composed of absorbent bosses (semi-cylinders or hemispheres) on an infinite plane of zero or infinite impedance. Popov<sup>33</sup> analyzed the problem of the diffraction of a plane wave traveling along a rigid half-plane that is smoothly joined to a convex cylinder whose radius of curvature is large in comparison with the

wavelength. Heaps<sup>6</sup> theoretically investigated the acoustical pressure field at a few wavelengths behind a plane disk irradiated by a plane wave of sound at oblique incidence and of wavelength comparable to the dimensions of the disk.

The problems of diffraction by "soft" and by "mixed" boundary conditions have been tried in recent years. Exact and approximate solutions have been developed for the "soft" half-plane and right-angled wedge. Other diffraction problems using various kinds of exotic boundaries and impedances have been examined.<sup>4,22,23,35,37,38</sup> An extensive list of these and other pertinent papers is given by Hutchins.<sup>8</sup>

Experimental investigations of sound diffraction by rigid obstacles have included spheres, cylinders, disks, square plates, cubes, and circular cones.<sup>21,46,47,48,49</sup> Many interesting results have been uncovered, but, unfortunately, the vast majority of published work has been conducted in air with either sound or electromagnetic waves. Reference 34 reports some experimental tests which were conducted under water where a hydrophone probed the diffraction field at various distances behind the disk along a line through the axis and parallel to the plane of the disk. The disks under test were rather thick and of (unnecessarily?) complex design to simulate a rigid and a pressure relief baffle. The qualitative features of the sound field were confirmed. Good quantitative agreement with theoretical predictions were found for the first minima from the bright spot, and the level of the pressure at the edge of the geometrical shadow. Agreement with the peak of the bright spot was poor and could be due to the non-ideal boundary conditions of the disk.

A theoretical study by Kouyoumjian and Hutchins<sup>18</sup> at Ohio State University has investigated the radiation pattern of a point source on the surface of a three-dimensional box. In this investigation, three analytical techniques are compared: the eigenfunction solution, Pauli's equation, and the Geometrical Theory of Diffraction. Of these, only the eigenfunction solution can be applied when the point source is less than 0.5 wavelengths from an edge, a constraint that is central to the problem addressed in this research. The problem of computing the radiation and diffraction pattern from a source located on a right-angle wedge is highly complicated. An even greater degree of complexity is introduced when the right-angled wedge is replaced by a curved surface. This is because diffraction can arise from the discontinuity in the radius of curvature where the finite curvature of the edge meets the infinite curvature of the flat plane. Whether or not this is a practical problem has yet to be determined.

There are other reports, see Reference 3, which concern the investigation of rather specific and complex structures but which are not germane to the investigation described in this thesis. Tests conducted on rigid geometries are valid in either medium but the response of a probe as a function of the angle of incidence has not been treated in the literature. One exception due to Wiener<sup>48</sup> involves a mapping of the pressure fluctuation across the surface of a disk at various values of  $ka$  for a few specific angles of incidence. However, his values of  $ka$  were smaller than those presented here.

## CHAPTER II

### GEOMETRICAL THEORY OF ACOUSTICS AND DIFFRACTION

#### 2.1 Introduction

When the geometry of an object is large in terms of a wavelength, scattering and diffraction are found to be essentially local phenomena identifiable with specific parts of the object, e.g., points of specular reflection, shadow boundaries, and edges. A high frequency technique developed by Keller and termed the Geometrical Theory of Diffraction employs diffracted rays in a systematic way to describe this phenomenon. The method is approximate, but in cases where the local radius of curvature is sufficiently greater than a wavelength, it provides the leading terms in the asymptotic high frequency solution of the wave equation. In many cases, it gives surprisingly good results for radiating objects as small as a wavelength in extent.

The Geometrical Theory of Diffraction is an extension of the ray trace method of geometric acoustics and adds a new class of rays to geometric acoustics. It is hypothesized that, in addition to direct rays and reflected rays, diffracted rays will also exist. Admission of diffracted rays to the theory provides one with the tools required to compute the complete interference patterns produced by the interaction of the direct field of a transducer element with the indirect field scattered from its baffle and housing structure. The principles and advantages of the Geometrical Theory of Diffraction are summarized in Table 2.1.

TABLE 2.1

PRINCIPLES AND ADVANTAGES OF  
THE GEOMETRICAL THEORY OF DIFFRACTION

Summary of the Principles

- A) The direction of diffracted rays is determined from a generalization of Fermat's Principle.
- B) The variation of the field intensity along a diffracted ray is governed by the conservation of power flow in a tube of rays.
- C) The variation of the phase of the field along a ray path is given by  $-ks$ , except when the ray crosses a caustic where a phase jump is introduced.
- D) The value of the field at a reference point where diffraction occurs is obtained by the solution of a canonical problem which provides a diffraction coefficient. The field at the reference point is, in effect, an initial condition.
- E) The simple expressions for the ray diffracted fields fail at shadow boundaries, and boundaries of the reflected field.

Advantages

- A) It is conceptually simple.
- B) We can treat radiating structures, which because of their shape or size in terms of a wavelength would make the problem intractable otherwise.
- C) Generally speaking, the solutions involve elementary functions in compact form, which keeps the computation costs low.
- D) We know the nature of the approximation involved in applying the Geometrical Theory of Diffraction; the solution becomes more accurate as the size of the radiating system increases relative to the wavelength.
- E) We can identify the radiation as emanating from specific parts of the structure; this is a valuable property when dealing with the inverse problem of producing a desired radiation pattern.



The power of the Geometrical Theory of Diffraction is that it provides a technique of analyzing scattering from complex bodies by breaking them up into simpler canonical forms. Although this is an approximate method for obtaining the terms dominant in acoustic scattering, it provides an insight into the physical mechanisms.

## 2.2 Geometrical Acoustics

According to classical geometrical acoustics, the flow of acoustic energy between two points  $Q_1$  and  $Q_2$  is governed by Fermat's principle, i.e., it follows a ray path which satisfies

$$\partial \int_{Q_1}^{Q_2} \frac{dS}{c(S)} = 0, \quad (2.1)$$

where  $\partial$  represents the variational derivative,  $c(S)$  is the sound velocity of the medium which may vary along the propagation path, and  $dS$  denotes an increment of path length. The physical interpretation of Equation (2.1) is that sound energy propagates along a path in such a manner that the time of transit between  $Q_1$  and  $Q_2$  is a minimum (i.e., extremum) of all possible paths between the two points. In homogeneous media (for which  $c$  is constant everywhere), it follows from Equation (2.1) that a minimum transit time path is equivalent to the shortest ray path between the two points; i.e., a straight line.

The equation describing the field strength along a ray can be derived from the principle of energy flux conservation in a ray tube. If  $A_0^2$  is the intensity of the pressure field at  $Q_1$ , where the cross-sectional area of the ray tube is  $d\sigma_0$ , then the energy flux  $A_0^2 d\sigma_0$  must be conserved at every cross-section of the tube. In

particular, if the intensity is  $A^2$  at  $Q_2$ , where the ray tube cross-sectional area is  $d\sigma$ , the conservation of energy flux requires that

$$A_o^2 d\sigma_o = A^2 d\sigma . \quad (2.2)$$

The theory assumes that regular surfaces reflect and that diffraction is generated at the edges of the diffraction body. The ray tube is generated by diffraction at an element of the edge of the diffracting body and is singular at the diffracting edge element that generates it.

This bundle of rays, shown in Figure 2.1, converges at two lines with the principal radii of curvature at  $Q_1$  of  $\rho_1$  and  $\rho_2$ . The principal radii of curvature at  $Q_2$  are thus  $\rho_1 + s$  and  $\rho_2 + s$ , where  $s$  is the distance between  $Q_1$  and  $Q_2$ . The cross-sectional area  $d\sigma_o$  is given by

$$d\sigma_o = \rho_1 d\phi_1 \rho_2 d\phi_2 , \quad (2.3)$$

while  $d\sigma$  is given by

$$d\sigma = (\rho_1 + s) d\phi_1 (\rho_2 + s) d\phi_2 . \quad (2.4)$$

It follows from Equations (2.2), (2.3), and (2.4) that

$$A = A_o \sqrt{\frac{\rho_1 \rho_2}{(\rho_1 + s)(\rho_2 + s)}} . \quad (2.5)$$

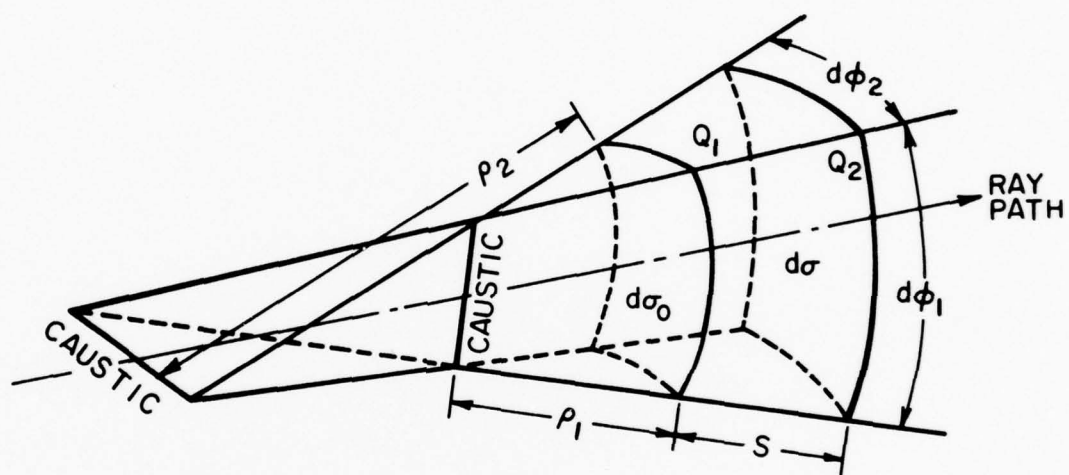


Figure 2.1 Ray Tube. A Caustic Occurs at Those Points where One or Both of the Radii of Curvature of the Wavefront Vanish.



Thus, the complete expression for the high frequency field at  $Q_2$ , including the phase  $\phi(Q_1)$  of the field at  $Q_1$  and the phase change  $ks$  along the rays, is given by

$$P(Q_2) = A(Q_2)e^{-jk\phi(Q_2)} = A_0 \sqrt{\frac{\rho_1 \rho_2}{(\rho_1 + s)(\rho_2 + s)}} e^{-jk[\phi(Q_1) + s]}. \quad (2.6)$$

From Equation (2.6), it can be seen that the geometric acoustics field becomes infinite at the points  $s = -\rho_1$  and  $s = -\rho_2$ , i.e., at the centers of curvature of the wavefront. Generally, examination of all the rays in the ray field shows that the geometrical acoustics field becomes infinite on surfaces which are the geometrical loci of all the centers of curvature of the wavefronts. These surfaces are called caustics. As the ray passes through a caustic line, the sign of  $(\rho + s)$  changes, and the correct phase shift of  $\pi/2$  is introduced.

Physically, the field actually observed on caustics is finite; the divergence predicted by Equation (2.6) simply means that the geometrical acoustics approximation becomes invalid at and in the vicinity of caustics, and that other means must be used to determine the field.

Applied to reflected rays, Fermat's principle states that in the case of ray paths connecting the points  $Q_1$  and  $Q_2$ , having one point of contact with a surface, sound energy travels along only that ray path on which the transit time is a minimum. This condition leads directly to the well-known law of reflection; namely, that the angle between the incident ray and the surface normal is equal to the angle between the normal and the reflected ray (angle of incidence = angle of reflection).

The field of a reflected ray is given by

$$P_R(Q_2) = R_\xi A_{\text{inc}}(Q) \sqrt{\frac{\rho_1 \rho_2}{(\rho_1 + s)(\rho_2 + s)}} e^{-jk[\phi_{\text{inc}}(Q) + s]}, \quad (2.7)$$

where  $R_\xi$  is the local reflection coefficient,  $A_{\text{inc}}(Q)$  is the amplitude of the incident field at  $Q$ , the point of specular reflection,  $\phi_{\text{inc}}(Q)$  being the phase of the incident field at  $Q$ .

If a curved surface has a shadow boundary, where the rays of the incident field are tangent to the surface, geometrical acoustics fails to account for the diffraction of energy into the shadow region. Again, if the surface has an edge, vertex, or corner, geometrical acoustics also fails to predict the accompanying diffraction. An examination of available asymptotic solutions for diffracted fields reveals that they contain fractional powers of  $\omega$ . It is apparent that in the presence of a reflecting body, geometric acoustics yields a high frequency approximation only for that portion of the scattered field which undergoes specular reflection. It does not predict scattering into shadow zones and does not allow for scattering by edges or vertices.

### 2.3 Geometrical Theory of Diffraction

Keller's extension of ray acoustics to include diffracted rays is commonly referred to as the Geometrical Theory of Diffraction (GTD). Although admittedly heuristic, it is in keeping with earlier extensions in the field of optics which introduced the wave nature of light, polarization, and the Fresnel reflection coefficients when this information was needed to describe light propagation. The basis of Keller's theory is the law of edge diffraction.

#### 2.4 The Law of Edge Diffraction

The law of edge diffraction is suggested by Snell's law of refraction. It follows in a modified form that may be stated as Fermat's principle for edge diffraction. An edge-diffracted ray between two points,  $Q_1$  and  $Q_2$ , is the curve of stationary path length between  $Q_1$  and  $Q_2$  with one point of the ray on the edge. Figure 2.2 indicates the diffraction of an incident ray from a wedge in a homogeneous medium. The diffracted rays form a cone whose angle is equal to the angle the incident ray makes with the edge. If the incident ray is normal to the edge, then the diffracted rays will form a disk.

The Geometrical Theory of Diffraction in a homogeneous medium gives the edge-diffracted contribution to the scattered field in terms of three factors: 1) a phase factor that accounts for the propagation of the ray over the length of the path,  $s$ , from  $Q_1$  to  $Q_2$ ; 2) a diffraction coefficient that expresses the ratio of the diffracted ray to the incident ray at the point of diffraction; and 3) a geometrical factor determined by the incident wave type (plane, spherical, or cylindrical) and the problem geometry.

#### 2.5 Geometrical Spreading Factor

The field on a single diffracted ray is given by

$$P_d = P_{\text{ref}} \sqrt{\frac{\rho_1 \rho_2}{(\rho_1 + s)(\rho_2 + s)}} e^{-jks}, \quad (2.8)$$

where  $P_{\text{ref}}$  is the field at some arbitrary reference point on the ray. By letting the edge be the reference point for computing  $P_d$  and by realizing that it must remain finite and be proportional to the incident

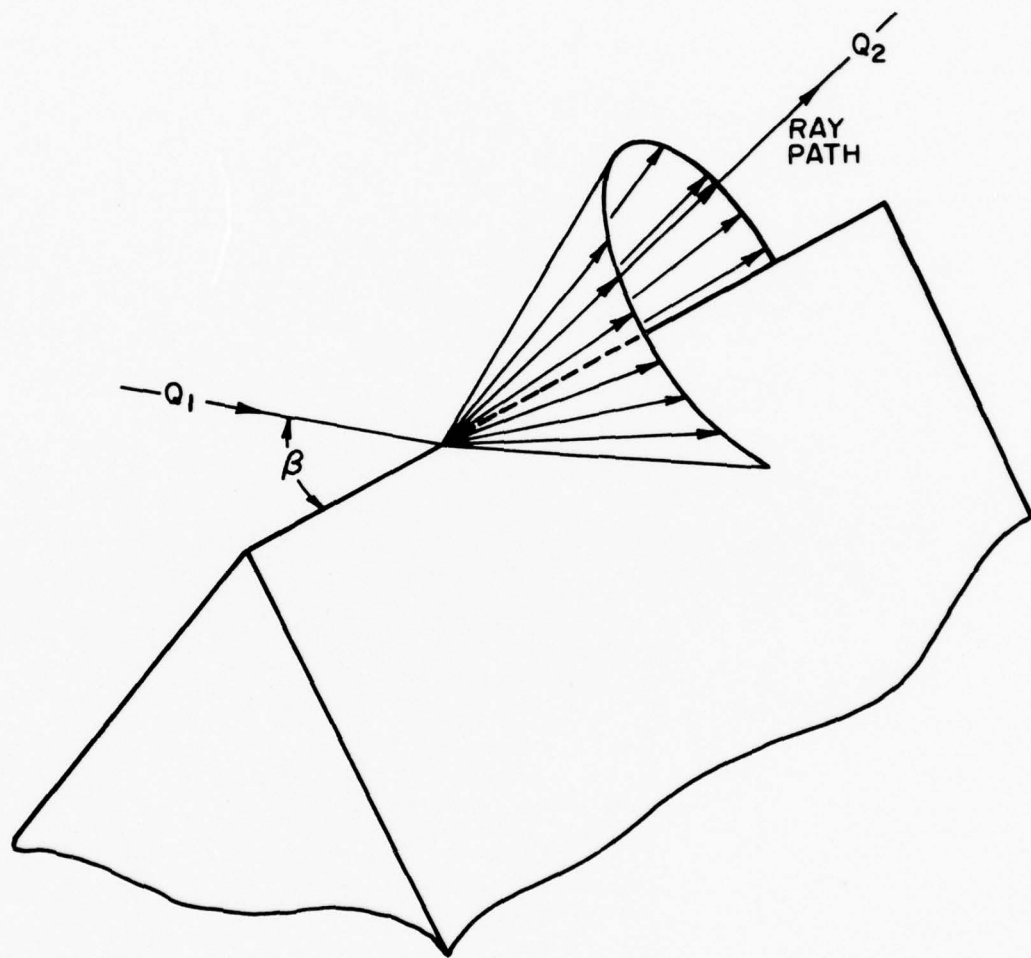


Figure 2.2 Edge Diffracted Rays Formed by an Incident Ray Grazing an Edge.

field at the edge,  $P_i$ , it follows that

$$P_d = P_i D(\phi, \phi') \sqrt{\frac{\rho_c}{(s + \rho_c)s}} e^{-jks} \quad (2.9)$$

The geometric factor

$$G.F. = \sqrt{\frac{\rho_c}{(s + \rho_c)s}} \quad (2.10)$$

describes the spreading out of the radiation from the point of diffraction, where  $s$  is the distance from the diffracting point to the field point, and  $\rho_c$  is the distance from the edge to the second caustic (or source). Note that the geometrical spreading factor does not take into account the geometrical spreading of the incident ray. This latter spreading must be included with  $P_i$ . The caustic distance  $\rho_c$  is obtained from differential geometry (see Reference 15, Appendix I) and is given by

$$\frac{1}{\rho_c} = \frac{\cos \delta}{\rho_e \sin^2 \beta} - \frac{1}{\sin \beta} \frac{d\beta}{d\ell}, \quad (2.11)$$

where  $\ell$  is the distance along the edge,  $\rho_e$  is the radius of curvature of the edge,  $\delta$  is the angle between the diffracted ray and the unit normal to the edge, and  $\beta$  is the angle between the incident ray and the tangent to the edge. The unit normal is chosen to point away from the center of curvature of the edge and to lie in the plane of the edge.

It is always instructive to present examples. The geometric factor, therefore, will be derived for several wave and edge geometries.



These examples are presented only for the desire to collect as many of the derived geometries as found in the literature.

### 2.5.1 Plane Wave or Cylindrical Wave Incident on a Straight Edge

For a plane or cylindrical wave incident on a straight edge,  $\frac{d\beta}{d\ell} = 0$  and  $\rho_e = \infty$ , so that  $\rho_c \approx \infty$ . Equation (2.10) thus becomes

$$G.F. = \frac{1}{\sqrt{s}}, \quad (2.12)$$

and the diffracted field is

$$P_d = P_i \frac{D(\phi, \phi')}{\sqrt{s}} e^{-jks}. \quad (2.13)$$

### 2.5.2 Plane Wave Incident on a Curved Edge

Suppose a plane wave is incident upon an edge with a finite radius of curvature. Since the edge is curved, the diffracted rays produced by two neighboring incident rays are not parallel. The projections back into the body of the scatterer intersect at a distance  $a$  from the point of diffraction. Thus, the wavefront at the diffraction point in one plane is  $s$  (the distance to the field point from the edge) plus the distance  $a/\cos \theta$ , where  $\theta$  is the angle formed at the diffracting edge between the radius of curvature and the plane wave ray. The resulting geometric spreading factor is

$$G.F. = \sqrt{\frac{-a/\cos \theta}{s(s - a/\cos \theta)}} = \frac{1}{\sqrt{s(1 - \frac{s \cos \theta}{a})}}, \quad (2.14)$$

which reduces to the straight edge case as the radius of curvature becomes infinite.

### 2.5.3 Spherical Wave Incident on a Straight Edge

A point source near a straight edge will generate an incident spherical wave for which the caustic distance is the distance from the source to the diffraction point. The geometrical factor is then simply

$$G.F. = \sqrt{\frac{\rho}{(\rho + s)s}} , \quad (2.15)$$

where  $\rho$  is the distance from the source to the diffraction point, and  $s$  is the distance to the field point. In the case of an incident spherical wave,  $P_i = e^{-jk\rho}/\rho$ , the diffracted field becomes

$$P_d = P_i D(\phi, \phi') \frac{\sqrt{\rho} e^{-jks}}{\sqrt{s(s + \rho)}} = \frac{e^{-jk(s + \rho)}}{\sqrt{\rho s(s + \rho)}} D(\phi, \phi') . \quad (2.16)$$

### 2.5.4 Point Source Located on Axis of Symmetry of a Circular Baffle

Consider one of the circular edges of a right circular cylinder, as in Figure 2.3, and the diffraction of spherical waves emanating from a point source lying on the axis of symmetry. A ray from this point source incident on the circular edge forms a right angle with the tangent to the edge, making  $\beta$  in Equation (2.11) always equal to  $\pi/2$ . The resulting cone of diffracted rays, therefore, degenerates to a plane disk. The  $z$ -axis is a caustic of the diffracted field since all the disks of diffracted rays produced at the edge of the baffle intersect the  $yz$ -plane along the axis and contribute to the far-zone field in that direction.

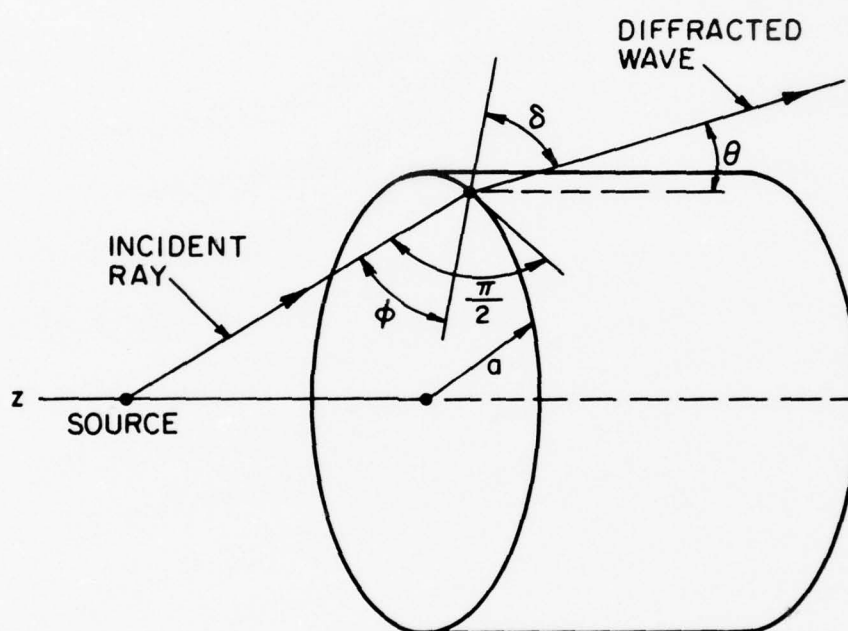


Figure 2.3 Diffraction of Spherical Waves from a Point Source on the Symmetry Axis of a Right Circular Cylinder.

Since  $\beta$  is always  $\pi/2$ , the term in Equation (2.11) proportional to  $d\beta/d\ell$  vanishes, i.e., the angle of incidence is independent of the location of the point of diffraction. The radius of curvature,  $\rho_e$ , is equal to  $a$ , the radius of the baffle, and  $\cos \delta = \sin \theta$ , where  $\theta$  is defined in Figure 2.3. Hence, the caustic distance is  $\rho_c = a/\sin \theta$ . The geometric energy spread factor for a point source at the center of a circular baffle becomes

$$\text{G.F.} = \sqrt{\frac{\rho_c}{(s + \rho_c)s}} = \frac{\sqrt{a}}{s \sqrt{a/s + \sin \theta}} \approx \frac{\sqrt{a}}{s \sqrt{\sin \theta}}. \quad (2.17)$$

When the observer distance is much greater than the radius of curvature, the last term of Equation (2.17) results.

#### 2.5.5 Point Source on a Circular Baffle

Consider a point source on a circular baffle as shown in Figure 2.4. In order to compute the field at point  $(R, \phi, \theta)$  due to the first-order diffraction of rays originating from the source at  $(\rho_s, \phi_s)$ , one must first solve Fermat's equation to obtain the caustic distance  $\rho_c$  which occurs in the geometrical spreading loss factor. Assuming the sound velocity to be constant in Equation (2.1), the ray path can be found by solving for the angle  $\phi_T$ . The value of  $\phi_T$  which satisfies Fermat's equation for the ray path lengths,  $\ell_p$  and  $\ell_d$ , will also satisfy the expression

$$\begin{aligned} \frac{\partial}{\partial \phi_T}(\ell_p + \ell_d) &= \frac{\partial}{\partial \phi_T} \left[ \{(a \cos \phi_T - \rho_s \cos \phi_s)^2 + (a \sin \phi_T - \rho_s \sin \phi_s)^2\}^{1/2} \right. \\ &\quad + \{(R \sin \theta \cos \phi - a \cos \phi_T)^2 + (R \sin \theta \sin \phi - a \sin \phi_T)^2 \\ &\quad \left. + z^2\}^{1/2} \right] = 0, \end{aligned} \quad (2.18)$$

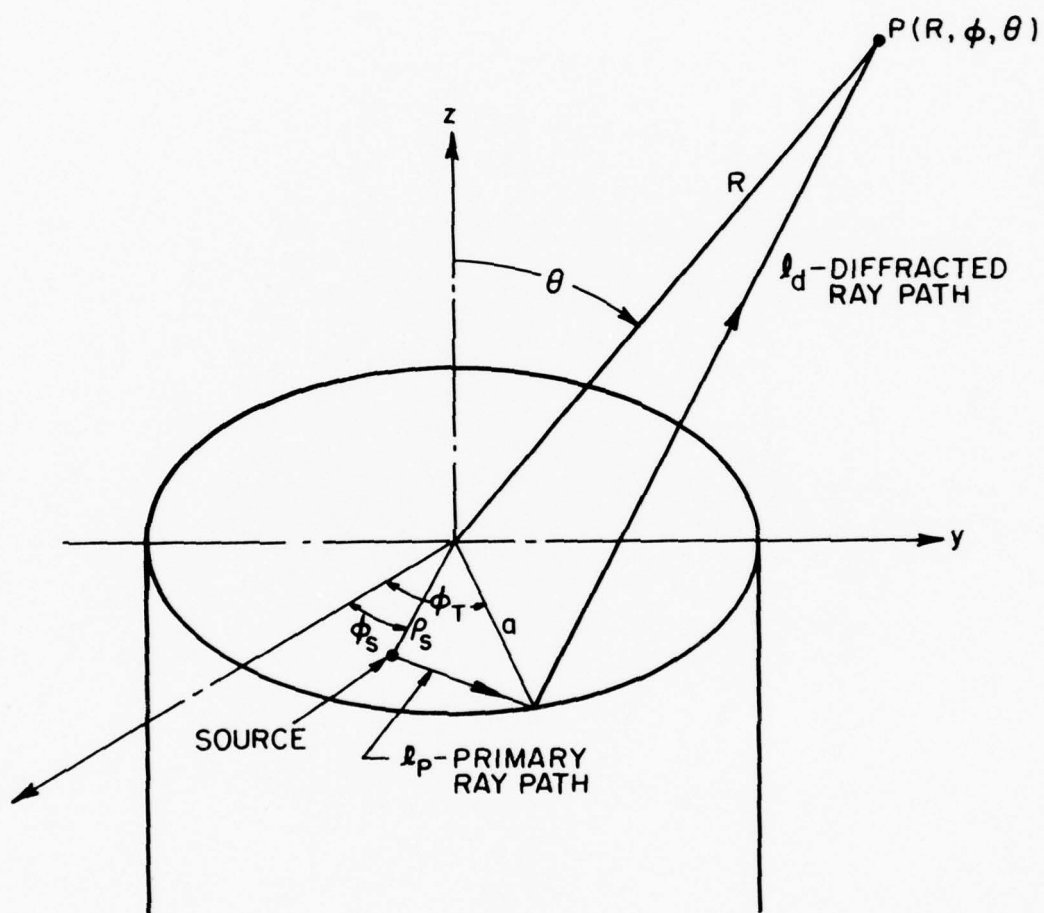


Figure 2.4 Geometry for Determining the Ray Path of a Point Source on a Circular Baffle.



where  $\ell_p$  and  $\ell_d$  have been written in terms of the distance between two points,

$$\ell^2 = (x_2 - x_1)^2 + (y_2 - y_1)^2 . \quad (2.19)$$

Knowing  $\phi_T$ , the angle  $\beta$  which the incident and diffracted rays make with the tangent to the edge can be expressed as,

$$\beta = \arccos \frac{\rho_s \sin(\phi_T - \phi_s)}{\ell_p} , \quad (2.20)$$

where

$$\ell_p = \sqrt{\rho_s^2 + a^2 - 2\rho_s a \cos(\phi_T - \phi_s)} . \quad (2.21)$$

As before, the caustic distance  $\rho_c$  is given by

$$\frac{1}{\rho_c} = \frac{\cos \delta}{\rho_e \sin^2 \beta} - \frac{1}{\sin \beta} \frac{d\beta}{d\ell} ,$$

where the radius of curvature  $\rho_e = a$ ,  $\cos \delta = \sin \phi_T \sin \theta$ ,

$$\frac{d\beta}{d\ell} = \frac{1}{a} \left. \frac{d\beta}{d\phi} \right|_{\phi=\phi_T} ,$$

and

$$\frac{d\beta}{d\ell} = \frac{\rho_s \cos(\phi_T - \phi_s)}{a\ell_p} \left[ 1 + \frac{\rho_s a \sin(\phi_T - \phi_s)}{\ell_p^2} \right] . \quad (2.22)$$

These relations can be simplified if the field is calculated in the yz-plane and, additionally, the source is rotated into the yz-plane. The source is now in the same plane as the field point, hence,

$\phi_T = \phi_s = \frac{\pi}{2}$ , giving  $\beta = 90^\circ$  and  $\ell_p = a - \rho_s$ . The caustic distance is

$$\frac{1}{\rho_c} = \frac{\sin \theta}{a} - \frac{\rho_s}{a\ell_p} \quad (2.23)$$

or

$$\rho_c = \frac{a\ell_p}{\ell_p \sin \theta - \rho_s} \quad (2.24)$$

Using Equation (2.10), the geometric factor for both the point source and the receiver lying in the yz-plane can be written as

$$G.F. = \frac{\sqrt{a}}{s\sqrt{\frac{a}{s} + \frac{\ell_p}{a}(\sin \theta + 1)} - 1}, \quad (2.25)$$

which reduces to Equation (2.17) when the source is moved to the axis of the circular baffle.

## 2.6 Diffraction Coefficient

It has already been shown that the field of a ray diffracted by an edge is given by the Geometrical Theory of Diffraction (GTD) in the form

$$P_d = P_i D(\phi, \phi') \sqrt{\frac{\rho}{s(\rho + s)}} e^{-jks} \quad (2.26)$$

The quantity  $D(\phi, \phi')$  is called the "diffraction coefficient" of the edge. These coefficients are obtained by comparison with canonical problems for various boundary conditions. It is the inadequacy of some diffraction coefficients for complex boundaries that proves to be the current limit on the usefulness of the GTD. The accuracy of GTD solutions is obviously limited by that of the canonical problems used to obtain the diffraction coefficients.

From the dimensions involved, it follows that the edge diffraction coefficients must have the dimension (distance)<sup>1/2</sup> or  $k^{-1/2}$ . Because the wavelength of the incident wave is assumed "small" (which, in this case, means small in terms of distance of that observation point from the edge), the incident wave "sees" only that portion of the edge in the vicinity of the diffraction point. This implies that scattering at the edge depends only on the local properties of the field, the wedge and the wedge geometry.

Assuming that only the local properties near the diffraction point are important, the diffraction coefficient can be determined from the solution of the simplest boundary value problem having these local properties. The appropriate canonical problem in this instance is the scattering of a plane wave by an infinite wedge of the same mechanical properties and with the same wedge angle.

#### 2.6.1 Sommerfeld Coefficient

When the field at the boundary is subject to the Dirichlet (i.e.,  $P = 0$ ) or Neumann (i.e.,  $\frac{\partial P}{\partial n} = 0$ ) conditions, the boundary conditions are referred to as soft and hard, respectively. Sommerfeld was the first to derive an exact solution of the wave equation for the problem of the diffraction of light by a wedge, limited by two perfectly reflecting planes. Using the Geometrical Theory of Diffraction, the diffracted field for Sommerfeld's (canonical) problem can be written as

$$P_d = P_i D(\phi, \phi') \frac{e^{-jks}}{s}, \quad (2.27)$$

which can be interpreted as a cylindrical wave going out from the edge

of the wedge with a characteristic amplitude dependent on  $\phi$ . Keller<sup>15</sup> compared his heuristic development to Sommerfeld's exact solution, asymptotically expanded for large values of  $kr$ , and obtained perfect agreement for

$$D(\phi, \phi') = \frac{e^{-j\pi/4} \sin \frac{\pi}{\eta}}{\eta \sqrt{2\pi k} \sin \beta} \left\{ \frac{1}{\cos \frac{\pi}{\eta} - \cos(\frac{\phi - \phi'}{\eta})} \pm \frac{1}{\cos \frac{\pi}{\eta} - \cos(\frac{\phi + \phi'}{\eta})} \right\}, \quad (2.28)$$

where the  $\{ \pm \}$  refers to the  $\begin{Bmatrix} \text{hard} \\ \text{soft} \end{Bmatrix}$  boundary conditions, the wedge angle equals  $(2 - \eta)\pi$ ,  $\phi$  is the angle between the plane and the direction of the observer,  $\phi'$  is the angle between the plane and the direction of the incident ray, and  $\beta$  is the acute angle between the incident ray and the tangent to the edge (see Figures 2.2 and 2.5). From Equation (2.28), it is observed that for  $\eta$ , such that  $\sin \frac{\pi}{\eta} = 0$ , the diffraction coefficient correctly vanishes.

The result is correct provided that

$$ks(\cos \frac{\pi}{\eta} - \cos \frac{\phi \pm \phi'}{\eta})^2 \gg 1.$$

It will fail, therefore, in the neighborhood of the shadow boundary, referred to as the transition region, where

$$\cos \frac{\pi}{\eta} = \cos \frac{(\phi \pm \phi')}{\eta}. \quad (2.29)$$

Sommerfeld tried to obtain an improved expression by modifying the path of integration. His results were not satisfactory because the neglected

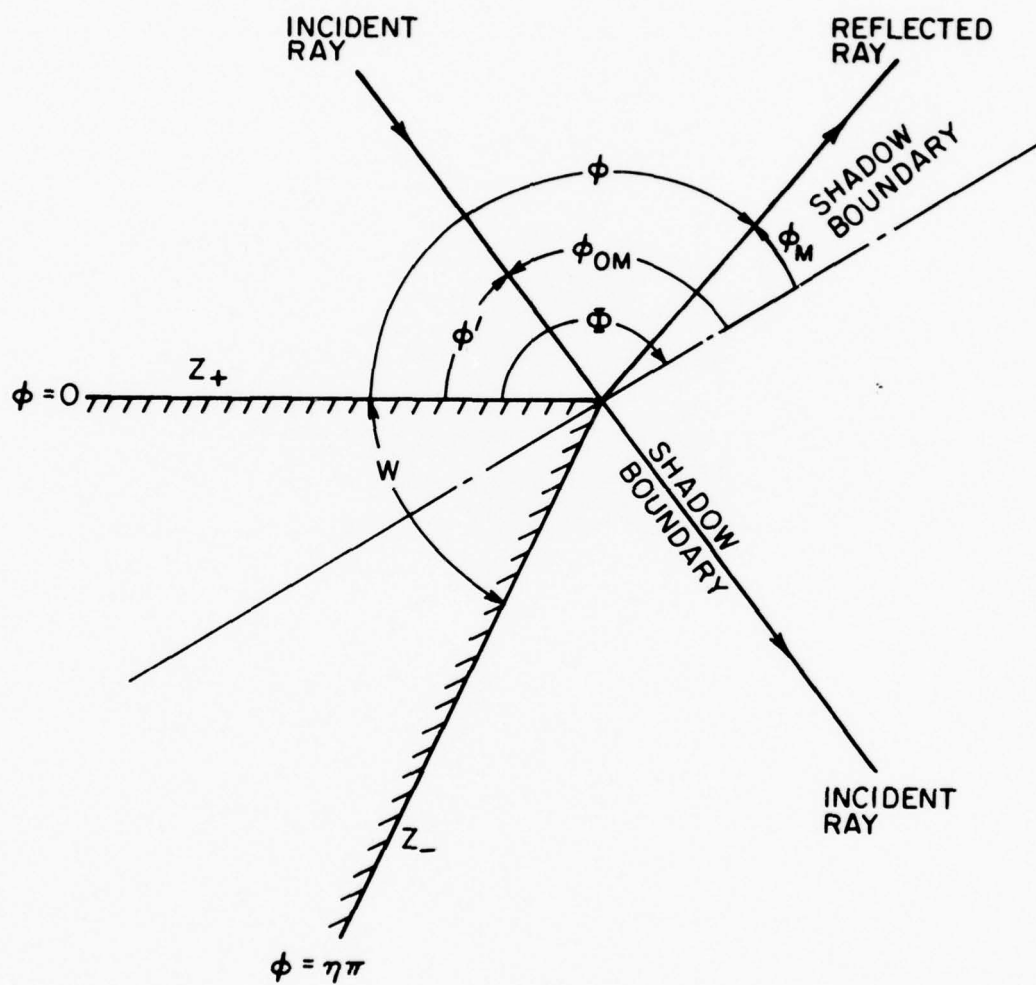


Figure 2.5 Geometry for Diffraction Problems.



terms were not sufficiently small in comparison to those retained.

Pauli<sup>32</sup> subsequently took a different approach based on a transformation of the integrand without changing the path of integration.

It should be noted that both the incident and reflected fields are discontinuous at their shadow boundaries. These discontinuities on the boundary are just compensated by the discontinuity of the diffracted field so that the total field is continuous. Pauli further confirmed that the field on the shadow boundary for  $kr$  large is equal to one-half of the incident field. He also concluded that the second term in the asymptotic series can be neglected for all practical cases.

Pauli's expression for the diffraction coefficient of a wedge, which is valid both within and outside the transition regions, was applied to the Geometric Theory of Diffraction by Kouyoumjian and Pathak.<sup>19</sup> This form of  $D(\phi, \phi')$  includes the Fresnel integral function and is modified by trigonometric substitution to obtain

$$\begin{aligned}
 D(\phi, \phi') = & \frac{-e^{-j\pi/4}}{2\eta \sqrt{2\pi k} \sin \beta} \left\{ \cot\left[\frac{\pi + (\phi - \phi')}{2\eta}\right] F[kLa^+(\phi - \phi')] \right. \\
 & + \cot\left[\frac{\pi - (\phi - \phi')}{2\eta}\right] F[kLa^-(\phi - \phi')] \\
 & \pm \cot\left[\frac{\pi + (\phi + \phi')}{2\eta}\right] F[kLa^+(\phi + \phi')] \\
 & \left. \pm \cot\left[\frac{\pi - (\phi + \phi')}{2\eta}\right] F[kLa^-(\phi + \phi')] \right\}, \quad (2.30)
 \end{aligned}$$

where  $F(x)$  denotes the transition function,

$$F(x) = 2j \sqrt{x} e^{jx} \int_{\sqrt{x}}^{\infty} e^{-j\tau^2} d\tau, \quad (2.31)$$

in which the principal (positive) branch of the square root  $\sqrt{x}$  is taken, and  $a^+(\phi \pm \phi')$  is simply a measure of the distance from the shadow boundary,

$$a^+(\phi \pm \phi') = 2 \cos^2 \left[ \frac{2\eta\pi N^+ - (\phi \pm \phi')}{2} \right], \quad (2.32)$$

$N^+$  being the integers which most nearly satisfy the equations

$$2\eta\pi N^+ - (\phi \pm \phi') = \pi$$

and

$$2\eta\pi N^- - (\phi \pm \phi') = -\pi. \quad (2.33)$$

It is seen that  $N^+$ ,  $N^-$  each have two values. For exterior edge-diffraction problems,  $N^+ = 0$  or  $1$  and  $N^- = -1, 0$  or  $1$ . The distance parameter,  $L$ , is obtained by requiring the diffracted fields to exactly compensate the geometrical acoustics discontinuity across the shadow boundaries. Expressions were found for several types of illumination, Reference 19,

$$L = \begin{cases} s \sin^2 \beta & \text{for plane-wave incidence} \\ \frac{\rho s}{\rho + s} & \text{for cylindrical-wave incidence,} \\ \frac{\rho s}{\rho + s} \sin^2 \beta & \text{for spherical-wave incidence} \end{cases} \quad (2.34)$$

where  $\rho$  is the radius of the normally incident wave and  $s$  is the perpendicular distance to the field point from the edge.

It can be seen from inspection of Equation (2.31) that the transition function  $F(x)$  includes an integral which can be written in

terms of the Fresnel integrals  $C(x)$  and  $S(x)$  (see Reference 1) as,

$$F(kLa^+) = 2j(kLa^+)^{1/2} e^{jkLa^+} \sqrt{\frac{\pi}{2}} \left\{ \left[ \frac{1}{2} - C(kLa^+) \right] - j \left[ \frac{1}{2} - S(kLa^+) \right] \right\}, \quad (2.35)$$

where

$$\begin{aligned} C(x) &= \int_0^x \cos\left(\frac{\pi}{2} t^2\right) dt \\ \text{and} \\ S(x) &= \int_0^x \sin\left(\frac{\pi}{2} t^2\right) dt. \end{aligned} \quad (2.36)$$

The Fresnel integrals are easily calculated numerically,<sup>43</sup> but care must be taken by noting that the argument is the square of the lower limit of the integration in Equation (2.31). The transition function,  $F(kLa^+)$ , is a smooth curve and does not oscillate. Its magnitude approaches zero and its phase approaches  $45^\circ$  for small arguments. For large arguments, (i.e.,  $x > 10$ ),  $F(kLa^+)$  approaches unity and its phase approaches  $0^\circ$ . If the arguments of the four transition functions in Equation (2.30) exceed 10, it follows that they can be replaced by unity, and Equation (2.30) reduces to Equation (2.28).

The first term in Equation (2.28) represents the diffracted field term for the incident ray and indicates that the shadow boundary is at  $\phi_i = \pi + \phi'$ . The diffracted field generated by the reflected ray is given by the second term where the shadow boundary is at an angle  $\phi_r = \pi - \phi'$ . The diffraction coefficients of Equations (2.28) and (2.30), therefore, can be thought of as a superposition of the individual incident and reflection diffraction terms. For both the hard and soft

cases, the magnitude of these rays are equal. They are in phase on the hard surface and out of phase on the soft surface as shown by the  $\pm$  sign in front of the reflected ray diffraction term.

A special case results when the incident field is at grazing incidence where  $\phi' = 0$ . At grazing incidence on a hard surface, the incident and reflected fields merge, so that one-half the total field propagating along the face of the wedge toward the edge is the incident field, and the other half is the reflected field. In this case, the incident field can be considered as the total field, therefore, only the incident ray diffraction term of Equation (2.28) can be kept. Alternatively, the incident and reflected rays can be treated separately keeping their respective diffraction terms. It is the latter concept which will be used. Equation (2.30) can be analyzed in the same manner, however, the values remain finite on the shadow boundaries, where the argument of the transition function is zero and the diffraction term's value is  $1/2$ .

At grazing incidence on a soft surface both Equations (2.28) and (2.30) will go to zero. This is not a physical phenomena, but instead is a result of neglecting any higher order derivatives of the incident field. Pauli<sup>32</sup> derived the first few terms of the asymptotic expansion and then ignored all but the first term since he was dealing with the field on a hard surface. Keller<sup>15</sup> recognized that for the grazing incidence case, diffraction associated with the first derivative of the incident field across the edge will become the leading term in the asymptotic expansion (see also References 10 and 25). Hence, the diffracted field for this case is proportional to  $\partial P_1 / \partial n$ , the normal derivative of the incident field at the edge. Thus, Equation (2.26)

must be replaced by

$$P_d = \frac{\partial P}{\partial n} D'(\phi) \sqrt{\frac{\rho}{s(\rho + s)}} e^{-jks} . \quad (2.37)$$

Here,  $D'(\phi)$  is a new diffraction coefficient found by solving a canonical problem (Karp and Keller, Reference 11) to obtain

$$\begin{aligned} D'(\phi) &= \frac{1}{jk} \frac{\partial}{\partial \phi'} D(\phi, 0) \\ &= \frac{2e^{j\pi/4} \sin \frac{\pi}{\eta} \sin \frac{\phi}{\eta}}{\eta^2 \sqrt{2\pi k} k \sin^2 \beta \left( \cos \frac{\pi}{\eta} - \cos \frac{\phi}{\eta} \right)^2} . \end{aligned} \quad (2.38)$$

Since this diffraction term is dependent on the slope of the incoming field, it has been referred to as the slope-diffraction term.

The generalized diffraction coefficients defined by Equations (2.28) and (2.30) were derived for the special case of a hard- or soft-wedge boundary using techniques employed by Sommerfeld and Keller. Even though these techniques are not trivial, it should be noted again that they only apply to the special boundary conditions  $P = 0$  and  $\frac{\partial P}{\partial n} = 0$ .

#### 2.6.2 Malyuzhinets Coefficient

Malyuzhinets<sup>28</sup> has formulated a general method of solution for scattering in wedge-shaped regions with arbitrary boundary conditions. The hard, soft, and impedance boundaries are readily solvable by this method with the aid of special  $\psi_\phi(\alpha)$  functions defined by Malyuzhinets. The geometry for the edge diffraction coefficient, see Figure 2.5, has been converted from the original coordinate system by the substitution



$$\phi_{\text{MALY}} = \Phi - \phi, \quad \phi_{\text{om}} = \Phi - \phi', \quad (2.39)$$

where

$$\Phi = \eta\pi/2. \quad (2.40)$$

The diffraction coefficient, which was derived for large  $kr$  and is the first term of an asymptotic expansion using the methods of steepest descents, is given as

$$D(\phi, \phi') = - \frac{\sin \frac{\phi'}{\eta} e^{-j\pi/4}}{\sqrt{2\pi k} \eta \Psi(\Phi - \phi')} \left\{ \frac{\Psi(\Phi - \phi - \pi)}{\cos \frac{\Phi + \pi}{\eta} - \cos \frac{\phi'}{\eta}} - \frac{\Psi(\Phi - \phi + \pi)}{\cos \frac{\Phi - \pi}{\eta} - \cos \frac{\phi'}{\eta}} \right\}, \quad (2.41)$$

with

$$\begin{aligned} \Psi(\alpha) &= \Psi_{\Phi}(\alpha + \Phi + \pi/2 - \theta_+) \Psi_{\Phi}(\alpha - \Phi - \pi/2 + \theta_-) \\ &\times \Psi_{\Phi}(\alpha + \Phi - \pi/2 + \theta_+) \Psi_{\Phi}(\alpha - \Phi + \pi/2 - \theta_-), \end{aligned} \quad (2.42)$$

where

$$\Psi_{\Phi}(\alpha) = \prod_{n=1}^{\infty} \prod_{m=1}^{\infty} \left[ 1 - \left( \frac{\alpha}{2\Phi(2n-1) + (\pi/2)(2m-1)} \right)^2 \right]^{(-1)^{m+1}} \quad (2.43)$$

and the grazing Brewster Angle is given by

$$\theta_{\pm} = \sin^{-1} \frac{\rho c}{Z_{\pm}}. \quad (2.44)$$

$Z_+$  is the normal surface impedance for  $\phi = 0$ , while  $Z_-$  is the normal surface impedance for  $\phi = \eta\pi$ . Equations (2.41), (2.42), (2.43), and (2.44) define the scattering for an incident pressure field with  $e^{j\omega t}$  time-dependence and, hence, give the complex conjugate of the formulation prepared by Malyuzhinets. Equation (2.41) can be converted to the general impedance diffraction coefficient by comparison with Equations (2.28) and (2.30),

$$\begin{aligned}
D(\phi, \phi') = & \frac{-e^{-j\pi/4}}{2\eta \sqrt{2\pi k} \sin \beta} \left[ \frac{\Psi(\phi - \phi' - \pi)}{\Psi(\phi - \phi')} \left\{ \cot \left[ \frac{\pi + (\phi - \phi')}{2\eta} \right] F[kLa^+(\phi - \phi')] \right. \right. \\
& - \cot \left[ \frac{\pi + (\phi + \phi')}{2\eta} \right] F[kLa^+(\phi + \phi')] \} \\
& + \frac{\Psi(\phi - \phi' + \pi)}{\Psi(\phi - \phi')} \left\{ \cot \left[ \frac{\pi - (\phi - \phi')}{2\eta} \right] F[kLa^-(\phi - \phi')] \right. \\
& \left. \left. - \cot \left[ \frac{\pi - (\phi + \phi')}{2\eta} \right] F[kLa^-(\phi + \phi')] \right\} \right] , \quad (2.45)
\end{aligned}$$

where the Fresnel integrals are given in Equations (2.31) and (2.35) and the  $\Psi_\phi(\alpha)$  functions are given in Equations (2.42) and (2.43).

Malyuzhinets also published the following form of the impedance function, rewriting Equation (2.43) for the rational ratio  $4\phi/\pi = n/m$  with odd and even  $n$ , respectively, as

$$\Psi_{\pi n/4m}(\alpha) = \prod_{k=1}^m \prod_{\ell=1}^n \left[ \frac{\cos \beta/2}{\cos(\alpha/2n + \beta/2)} \right]^{(-1)^\ell} , \quad (2.46)$$

and

$$\Psi_{\pi n/4m}(\alpha) = \prod_{k=1}^m \prod_{\ell=1}^n \exp \left[ \frac{(-1)^\ell}{\pi} \int_{\beta}^{\beta+\alpha/n} u \cot u \, du \right] , \quad (2.47)$$

where

$$\beta = \frac{\pi}{2} \left[ \frac{2\ell - 1}{n} - \frac{2k - 1}{m} \right] . \quad (2.48)$$

The values of  $n$  and  $m$  are, for example,  $n = 3$  and  $m = 1$  for a  $90^\circ$  wedge, and  $n = 19$ ,  $m = 6$  for a  $75^\circ$  wedge.

The techniques used to obtain the diffraction coefficient for an impedance wedge boundary makes the total field continuous across the reflection and shadow boundaries. Since the diffracted field is a function of the incident field (not the reflected field), the Malyuzhinets

diffraction coefficient must compensate for an impedance surface at the reflection boundary; i.e., the reflection coefficient is inherently built into the diffraction coefficient.

### 2.6.3 Comparison of Diffraction Coefficients

It is instructive to compare the directivity patterns of the Sommerfeld and Malyuzhinets diffraction coefficients, Equations (2.30) and (2.45), respectively. Each of the four terms present in Equation (2.30) can be found in Equation (2.45) multiplied by an impedance  $\Psi_\phi(\alpha)$  function. However, in the Malyuzhinets diffraction coefficient, the terms no longer can be separated into an expression for the incident and reflected rays. For example, the reflection terms in the Sommerfeld equation (the third and fourth terms) are found as the second and fourth terms of the Malyuzhinets equation. The signs of the terms correspond to a soft baffle, indicating the initial boundary condition from which Malyuzhinets began his derivation. The  $\Psi_\phi(\alpha)$  functions, however, reference one term to the impedance of the  $Z_+$  surface and the other to the  $Z_-$  surface. It will be seen later that the impedance of the surface which is in the direction of the field point plays the dominant role.

The directivity patterns of the Sommerfeld diffraction coefficient on a  $90^\circ$  wedge, with and without the transition function is shown in Figure 2.6(a), where the field variable is  $\theta = \phi' - \pi/2$ . The observer angle is fixed, while the source angle varies. The curve generated without using the transition function goes to infinity at the shadow boundary. The pressure levels at angles larger than  $\pm 30^\circ$  from the shadow boundary are not affected by the transition function. Equations

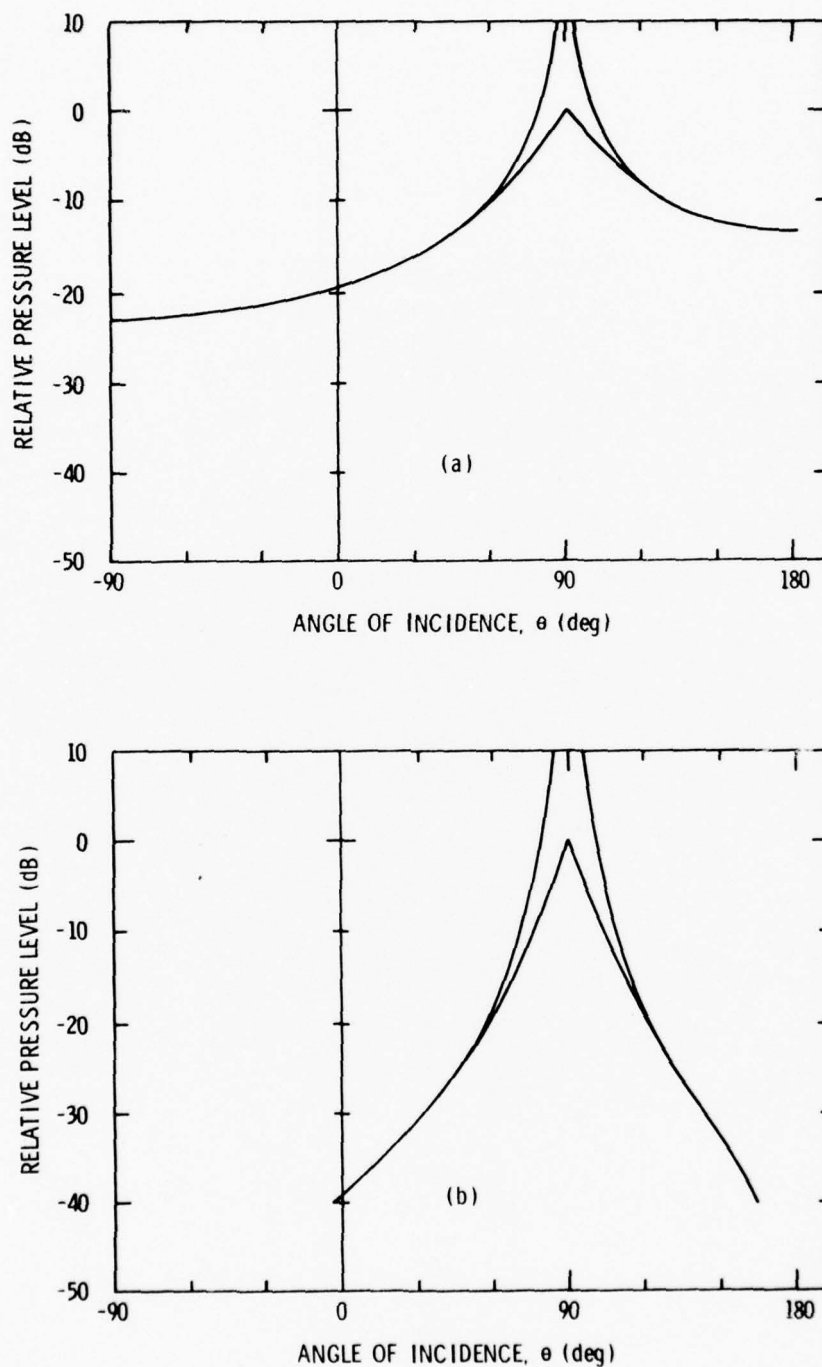


Figure 2.6 Calculated Directivity Patterns with  $\phi = 0^\circ$  for the Sommerfeld Diffraction Coefficient for the Hard Edge in (a), and Keller's Coefficient for the Soft Edge in (b). Comparison is With and Without Transition Function.

(2.28) and (2.30) were used to calculate the directivity patterns using a source at grazing incidence on a hard surface located three wavelengths from a  $90^\circ$  wedge. Notice that the diffracted pressure is finite at all angles exterior to the wedge. The angles  $90^\circ$  and  $180^\circ$  bound the shadow zone where only the diffracted field exists. The diffracted field between  $-90^\circ$  and  $+90^\circ$  coexists with the incident and reflected fields and creates a ripple interference effect. The high amplitude of the diffracted field on a hard surface can cause a significant ripple.

The edge of a soft surface, on the other hand, produces a diffraction coefficient which, because of its low level, will create very little ripple in the insonified region. The directivity pattern for a grazing ray on the edge of a soft surface is shown in Figure 2.6(b) and was calculated using Equation (2.38) and its modification for the transition region. Notice again that both curves merge at  $\pm 30^\circ$  from the shadow boundary indicating the beginning of the transition region. In comparison to the hard surface, the soft surface diffracted field rapidly diminishes in amplitude away from the shadow boundary.

When  $\phi'$  is non-zero, the grazing ray case where both the incident and reflection shadow boundaries coincide is removed. Shown in Figures 2.7(a) and 2.7(b) are the directivity patterns with a hard and soft baffle, respectively, for a  $30^\circ$  angle between the plane and the direction of the incident ray. These curves again show that the transition region begins at angles  $\pm 30^\circ$  from a shadow boundary. The resulting pattern in Figure 2.7(a) can be thought of as a composite of two patterns each of which are similar to that in Figure 2.6(a) but shifted by an angle  $\phi'$ .



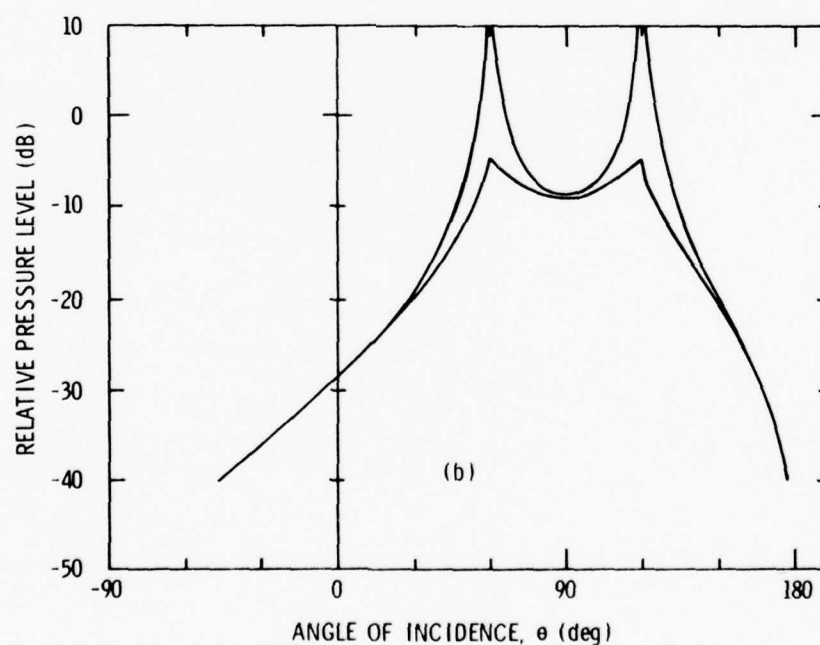
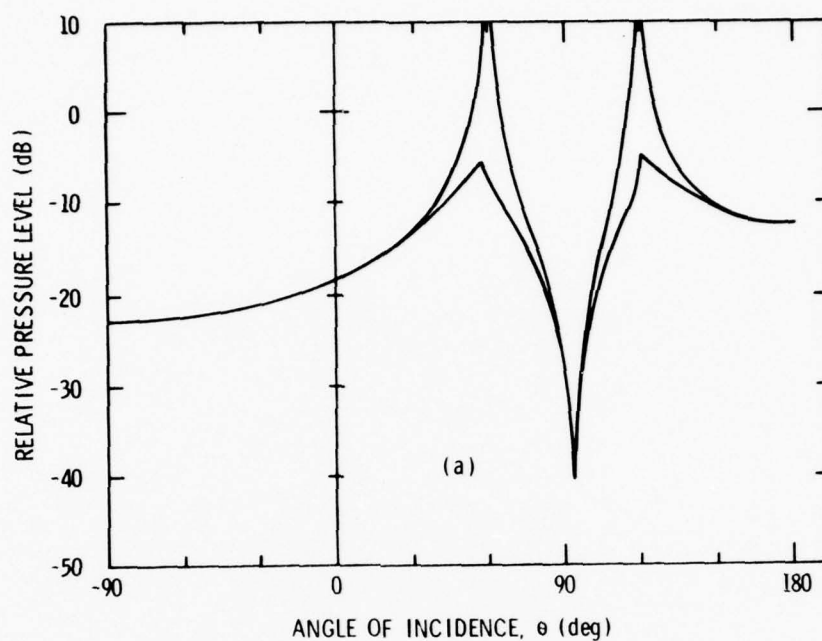


Figure 2.7 Calculated Directivity Patterns with  $\phi = 30^\circ$  for the Sommerfeld Hard Diffraction Coefficient in (a), and the Sommerfeld Soft Diffraction Coefficient in (b). Comparison is With and Without Transition Function.

The first pattern, peaking at  $\theta = 60^\circ$  is due to the reflected ray and the second at  $\theta = 120^\circ$  is due to the incident ray. The phase of each diffracted field shifts  $180^\circ$  as it passes through a shadow boundary. The phase reversal leads to the situation where, between the shadow boundaries ( $90^\circ < \theta < 120^\circ$ ), the two diffracted fields are opposite in phase. The cancellation effect seen in Figure 2.7(a) results. The two diffracted fields are in phase at all other angles (i.e.,  $\theta < 90^\circ$  and  $\theta > 120^\circ$ ).

Just the opposite phase relationships exist for the diffracted field on a soft baffle, as shown in Figure 2.7(b). The second term in Equation (2.28) is negative, thus making the incident and reflection diffracted fields in phase for angles between the shadow boundaries, and out of phase at all other angles. These phase relationships account for the shallow dip in the pattern between shadow boundaries and the rapid decrease in level outside the shadow boundaries.

Shown in Figures 2.8(a) and 2.8(b) are the directivity patterns of the Sommerfeld hard [Equation (2.30)] and the Keller soft [modified Equation (2.38)] diffraction coefficients, respectively, for a point source at several distances from the diffracting edge. As expected, the closer to the edge that a source is located, the higher the diffracted field. Figure 2.8 clearly indicates quantitatively the increase in the diffracted field as the edge is approached. The distance of one-third wavelength,  $k\rho = 2$ , appears to give a valid diffracted field. Its validity will later be checked by comparison with experimental data.

The previous discussion has dealt with only hard or soft surface impedance conditions. The Malyuzhinets diffraction coefficient defined by Equation (2.45) allows investigation of surfaces of intermediate impedances. In order to obtain an understanding of the effect of

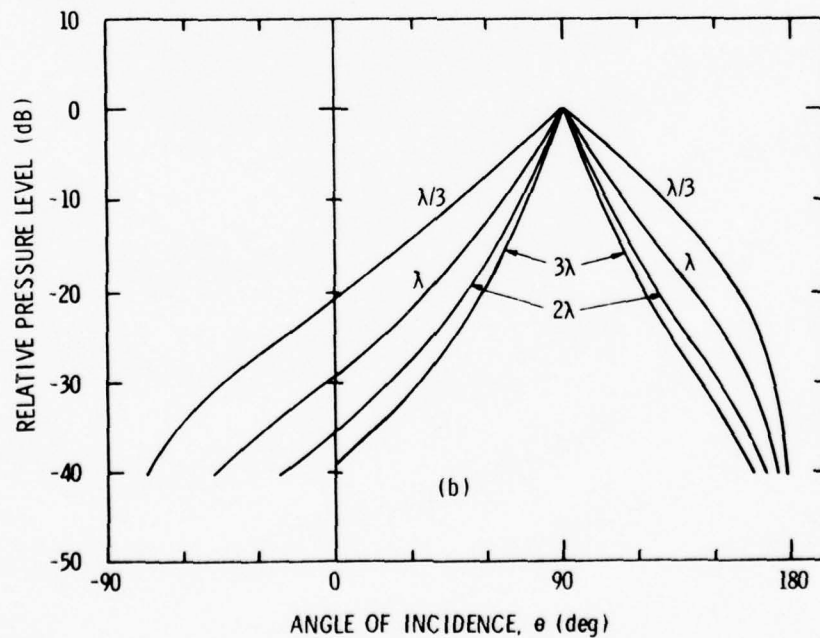
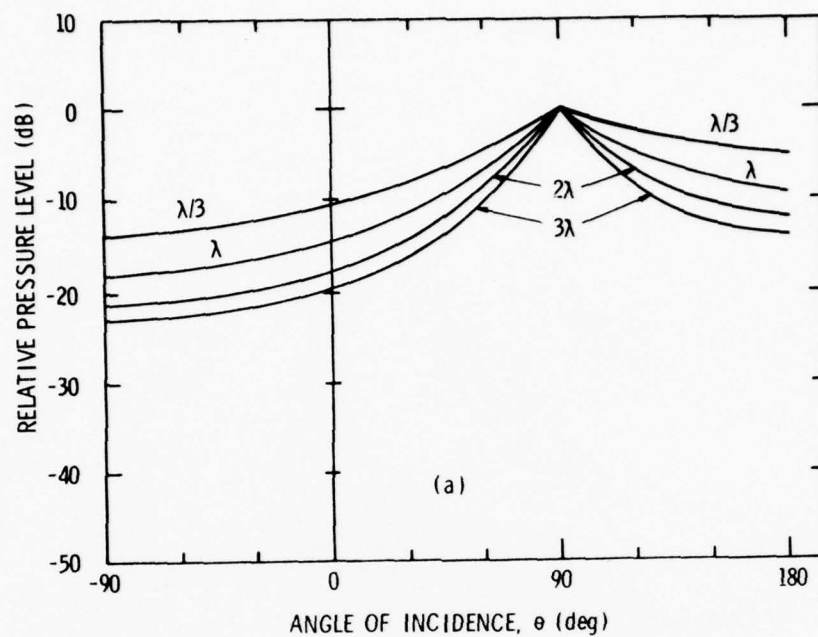


Figure 2.8 Calculated Directivity Patterns of the Sommerfeld Hard (a) and Keller Soft (b) Diffraction Coefficients for Several Distances from the Edge.

changing surface impedance, the directivity patterns for a  $\phi = 30^\circ$  were plotted in Figure 2.9 as a function of the surface impedance ratio  $Z/\rho c$ . Both surfaces of the wedge had the same impedance, i.e.,  $Z_+ = Z_-$ . Notice that the level of the incidence ray shadow boundary remains constant as the impedance is varied from soft to hard. Also, the level of the diffraction field present in the shadow region continuously increases as the impedance changes from soft to hard. The sharp-cornered pattern is that given by the hard Sommerfeld diffraction coefficient in Figure 2.7(a). The pattern for the lowest surface impedance which was plotted is equivalent to the pattern produced by the soft diffraction coefficient in Figure 2.7(b).

The amplitude at the reflected ray shadow boundary in Figure 2.9 goes through a minimum where the normal component of the surface impedance matches the impedance of the sound propagating medium. In water, which is the propagating medium under investigation, the impedance is  $\rho c = 1.5 \times 10^6$  MKS Rayls. It is interesting to observe that even though the diffracted field changes significantly with surface impedance in the illuminated region,  $\theta < 120^\circ$ , the diffracted field in the shadow region does not. Another indication that the diffracted field in the shadow region acts almost independently of the diffracted field in the illuminated region is that when the surface impedances  $Z_+$  and  $Z_-$  are different, the shadow region is controlled by  $Z_-$  and the illuminated region by  $Z_+$ . That is, the diffracted field in the shadow region for a given impedance,  $Z_-$ , only undergoes a minor change when the impedance of the other surface,  $Z_+$ , is changed. For all practical purposes, then, Figure 2.9 provides the pattern information for all cases of  $Z_+$  and  $Z_-$  impedances.

changing surface impedance, the directivity patterns for a  $\phi = 30^\circ$  were plotted in Figure 2.9 as a function of the surface impedance ratio  $Z/\rho c$ . Both surfaces of the wedge had the same impedance, i.e.,  $Z_+ = Z_-$ . Notice that the level of the incidence ray shadow boundary remains constant as the impedance is varied from soft to hard. Also, the level of the diffraction field present in the shadow region continuously increases as the impedance changes from soft to hard. The sharp-cornered pattern is that given by the hard Sommerfeld diffraction coefficient in Figure 2.7(a). The pattern for the lowest surface impedance which was plotted is equivalent to the pattern produced by the soft diffraction coefficient in Figure 2.7(b).

The amplitude at the reflected ray shadow boundary in Figure 2.9 goes through a minimum where the normal component of the surface impedance matches the impedance of the sound propagating medium. In water, which is the propagating medium under investigation, the impedance is  $\rho c = 1.5 \times 10^6$  MKS Rayls. It is interesting to observe that even though the diffracted field changes significantly with surface impedance in the illuminated region,  $\theta < 120^\circ$ , the diffracted field in the shadow region does not. Another indication that the diffracted field in the shadow region acts almost independently of the diffracted field in the illuminated region is that when the surface impedances  $Z_+$  and  $Z_-$  are different, the shadow region is controlled by  $Z_-$  and the illuminated region by  $Z_+$ . That is, the diffracted field in the shadow region for a given impedance,  $Z_-$ , only undergoes a minor change when the impedance of the other surface,  $Z_+$ , is changed. For all practical purposes, then, Figure 2.9 provides the pattern information for all cases of  $Z_+$  and  $Z_-$  impedances.



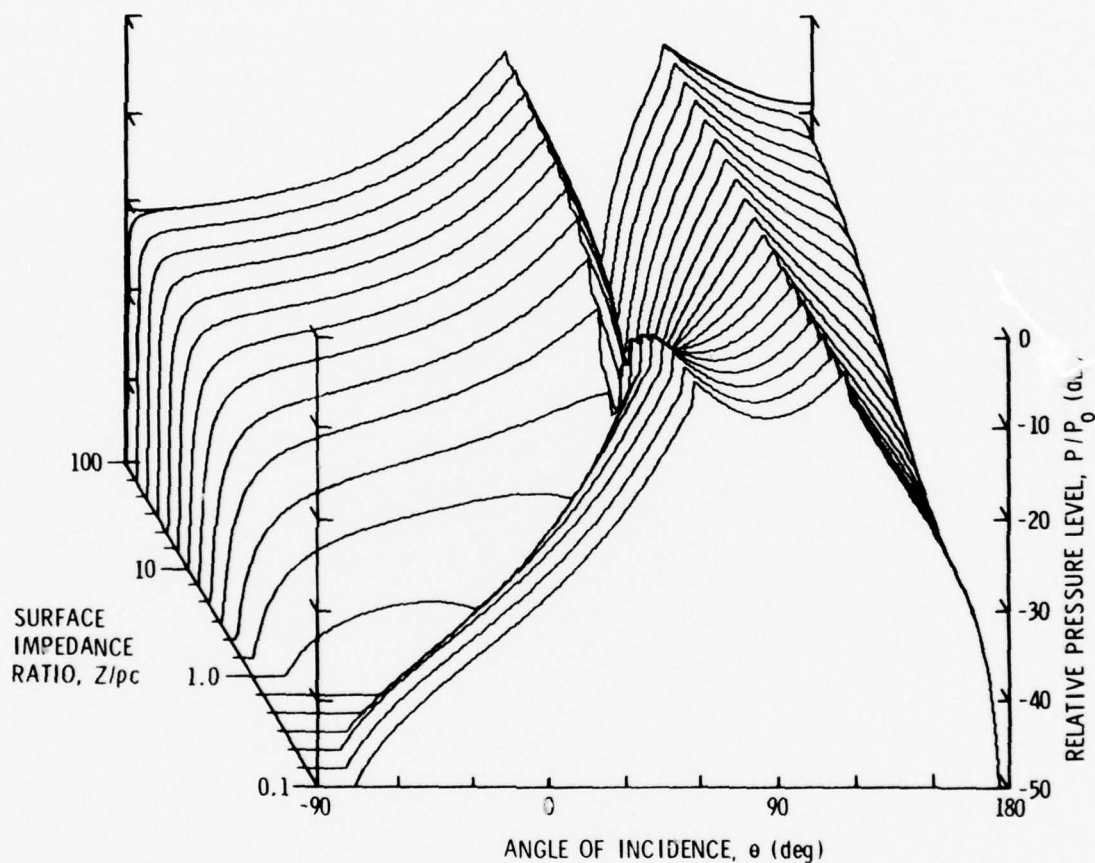


Figure 2.9 Calculated Directivity Patterns with  $\phi = 30^\circ$  as a Function of the Surface Impedance Using the Malyuzhinets Diffraction Coefficient.

In Figure 2.10, the change in the diffracted field as a function of the observation angle  $\phi$  is presented. The surface impedance ratio is  $Z/\rho c = 1.5$ . As  $\phi$  approaches an impedance surface, the diffracted field goes to zero. Continuity of the total field is maintained by the diffracted field amplitude between the shadow boundaries.

## 2.7 Reflection from an Impedance Wedge

When a progressive plane wave in a fluid medium impinges on the boundary of a second medium, a reflected wave is generated in the first medium. The ratio of the pressure amplitude of the reflected wave to that of the incident wave depends on the characteristic impedances of the two media and on the angle of the incident wave. The amplitude of the reflected wave can be represented by the complex reflection factor

$$R_{\xi} = \frac{(Z/\rho c) \cos \xi - 1}{(Z/\rho c) \cos \xi + 1}, \quad (2.49)$$

where  $\xi$  is the angle between the direction of propagation and the normal to the reflecting surface. Oblique incidence, therefore, reduces the acoustic impedance by a factor of  $\cos \xi$ . At grazing incidence, a finite impedance surface behaves as a soft surface. In addition, the surface impedance of the boundary usually depends on the angle of incidence. This dependency must also be taken into account when applying the reflection coefficient in an actual problem.

There are many references which deal with the reflection of sound from surfaces.<sup>31,39</sup> However, there seems to be no analysis in the literature concerning the attenuation of a wave front close to or on an impedance surface as a function of distance from the source. This is an area which needs further research.

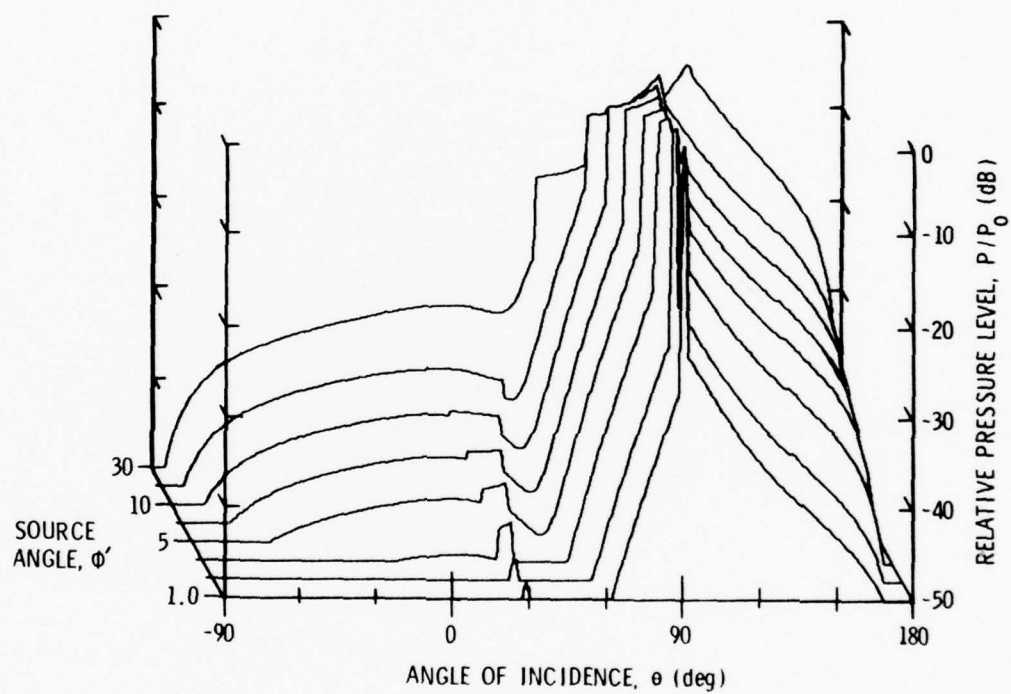


Figure 2.10 Calculated Directivity Patterns with Both Surface Impedance Ratios Equal to  $Z/\rho c = 1.5$  as a Function of Source Angle.

The analysis can be extended to the case of spherical waves, where a point source and receiver are located above an impedance surface as shown in Figure 2.11. An interference phenomena is produced between the sound reflected from the impedance surface and the sound coming directly from the source without reflection. Analysis of this effect can best be done using a source-image approach.

Let a point source be located a distance,  $\ell$ , above an impedance surface. The direct path length from the source to the receiver is  $b$ , and the path length of the reflected ray is equivalent to the distance from the image source to the receiver,  $a$ . By first referencing the coordinate system to the surface and then to the edge as in Figure 2.11, the distances can be written as follows:

$$r = [d^2 + s^2 - 2ds \cos(\theta + \pi/2)]^{1/2}, \quad (2.50)$$

$$\phi = \pi/2 - \cos^{-1} \left[ \frac{r^2 + d^2 - s^2}{2rd} \right], \quad (2.51)$$

$$a = [r^2 + \ell^2 - 2r\ell \cos(\pi - |\phi|)]^{1/2} \quad (2.52)$$

and

$$b = [r^2 + \ell^2 - 2r\ell \cos \phi]^{1/2}. \quad (2.53)$$

The reflection coefficient given in Equation (2.49) can be used where the angle of reflection is given by

$$\xi = \cos^{-1} \left[ \frac{\ell^2 + a^2 - r^2}{2\ell a} \right]. \quad (2.54)$$

The total pressure field at the receiver is simply the sum of the pressures resulting from the direct ray and the reflected ray, the latter being modified in amplitude and phase by a reflection coefficient,

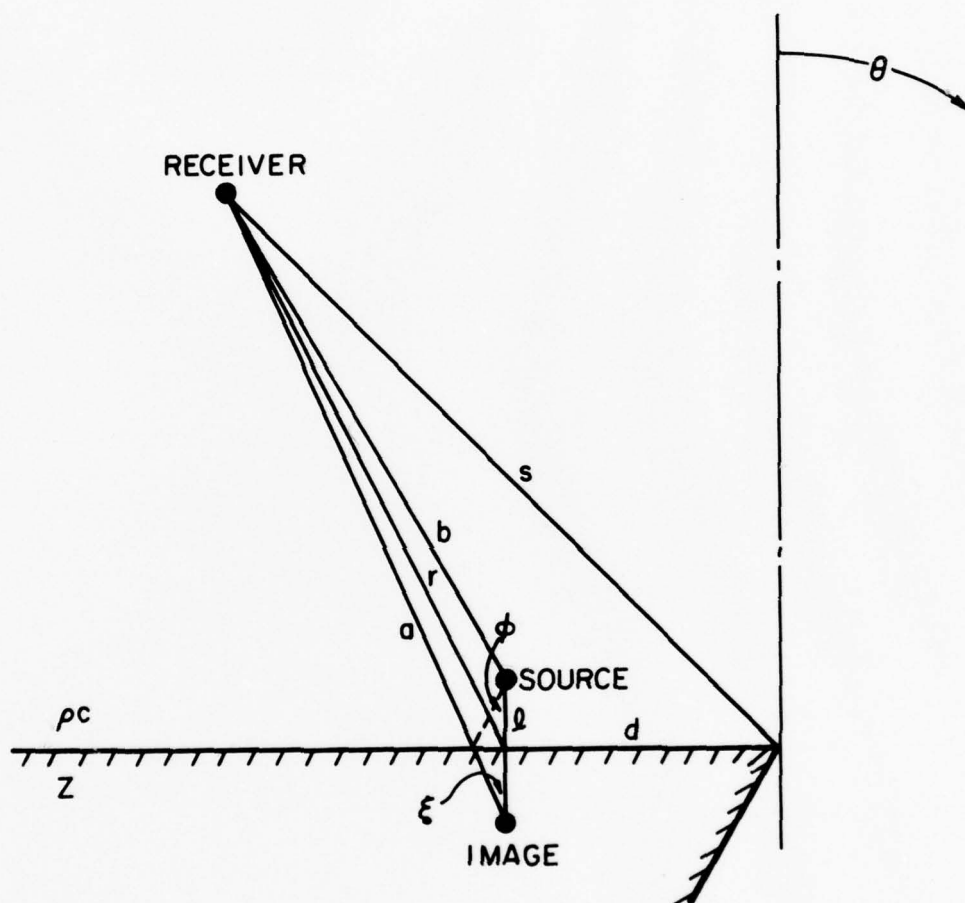


Figure 2.11 Reflection from an Impedance Wedge.

$$P(\text{total}) = \frac{e^{-jkb}}{b} + R_{\xi} \frac{e^{-jka}}{a} . \quad (2.55)$$

The source-image approach uses a ray analysis concept which should be compatible with the ray concept of the Geometric Theory of Diffraction.

## 2.8 Attenuation of Progressive Waves on an Impedance Surface

The same analysis as used in Section 2.7 can be used to determine the attenuation of a progressive wave as it propagates along an impedance surface. Assume that both the source and receiver are the same distance  $\ell$  from the surface, where  $\ell$  is a small portion of a wavelength, and are separated by a distance  $b$ . The distance from the image source to the receiver is  $a = \sqrt{4\ell^2 + b^2}$ , and the reflection angle is  $\sin \xi = b/a$ . Using Equation (2.55) for various values of  $b$  and  $Z/\rho c$ , curves can be generated which will define the signal attenuation on an impedance surface. In the limits, the far field attenuation is 6 dB and 12 dB per doubling of distance for the rigid and soft surfaces, respectively. An impedance surface should have an intermediate value.

## 2.9 Finite Size of Receiver

Ideally, an infinitely small receiver would measure twice the pressure of an incident wave at a rigid surface and would measure zero at a soft surface. However, an actual receiver, small though it may be, has a finite size.

Depending upon the problem, it is sometimes easier to utilize the reciprocity principle and exchange the role of the source and receiver. Let us now place the receiver near a reflecting surface. The effect of the finite size of the receiver can be ascertained for the case of a plane wave incident normal to the surface. The receiver is a cylindrical



piezoelectric ceramic transducer over which we wish to obtain the average pressure; hence, we must perform an integration over the probe surface of the form,

$$P_{ave} = \frac{\int_{\sigma} P_i d(\text{area})}{\int_{\sigma} d(\text{area})}, \quad (2.56)$$

where  $P_i$  is the incident pressure, and  $\sigma$  denotes the surface. The problem of a plane wave incident on a cylinder can be treated as a two-dimensional problem with sufficiently accurate results. Since the probe cross-sectional area is a circle of a radius  $a$ , see Figure 2.12, we thus have

$$P_{ave} = \frac{\int_0^{2\pi} P_i a d\theta}{\int_0^{2\pi} a d\theta} = \frac{1}{2\pi a} \int_0^{2\pi} P_i a d\theta. \quad (2.57)$$

For the case of a soft surface, the incident pressure can normally be written as

$$P_i = P_{max} \sin(kx), \quad (2.58)$$

where  $x = r + a \cos \theta$  for the surface of the receiver. Thus,

$$P_{ave}(\text{soft}) = \frac{1}{2\pi a} \int_0^{2\pi} P_{max} \sin(kx) a d\theta = \frac{P_{max}}{\pi} \int_0^{\pi} \sin[kr + ka \cos \theta] d\theta \quad (2.59)$$

and

$$P_{ave}(\text{soft}) = P_{max} \left\{ (\sin kr) \frac{1}{\pi} \int_0^{\pi} \cos(ka \cos \theta) d\theta + (\cos kr) \frac{1}{\pi} \int_0^{\pi} \sin(ka \cos \theta) d\theta \right\}. \quad (2.60)$$

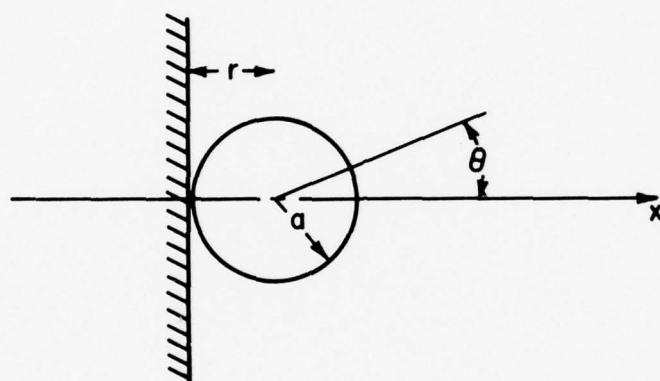


Figure 2.12 Circular Cross-Sectional Area of a Receiver Near the Baffle Surface.

Integrating this, we obtain<sup>29</sup>

$$P_{\text{ave}}(\text{soft}) = P_{\text{max}} \sin kr J_0(ka) . \quad (2.61)$$

For the case of a rigid surface,

$$P_i = P_{\text{max}} \cos(kx) \quad (2.62)$$

and

$$\begin{aligned} P_{\text{ave}}(\text{rigid}) &= \frac{P_{\text{max}}}{\pi} \int_0^\pi \cos[kr + ka \cos \theta] d\theta \\ &= \frac{P_{\text{max}}}{\pi} \int_0^\pi [\cos kr \cos(ka \cos \theta) \\ &\quad - \sin kr \sin(ka \cos \theta)] d\theta . \end{aligned} \quad (2.63)$$

Hence,

$$P_{\text{ave}}(\text{rigid}) = P_{\text{max}} \cos kr J_0(ka) . \quad (2.64)$$

Figure 2.13 presents a plot of Equations (2.61) and (2.64) for the case of the receiver touching the surface ( $r = a$ ). The level of  $P_{\text{max}}$  is twice the level of the incident pressure which, in the absence of the baffle, is the free-field pressure.

## 2.10 Transmission Properties of a Baffle

The objective of this research is to study the diffraction effects caused by finite baffles. If the transmission properties of the baffle are not controlled or well known, then analysis of the experimental results may become difficult.

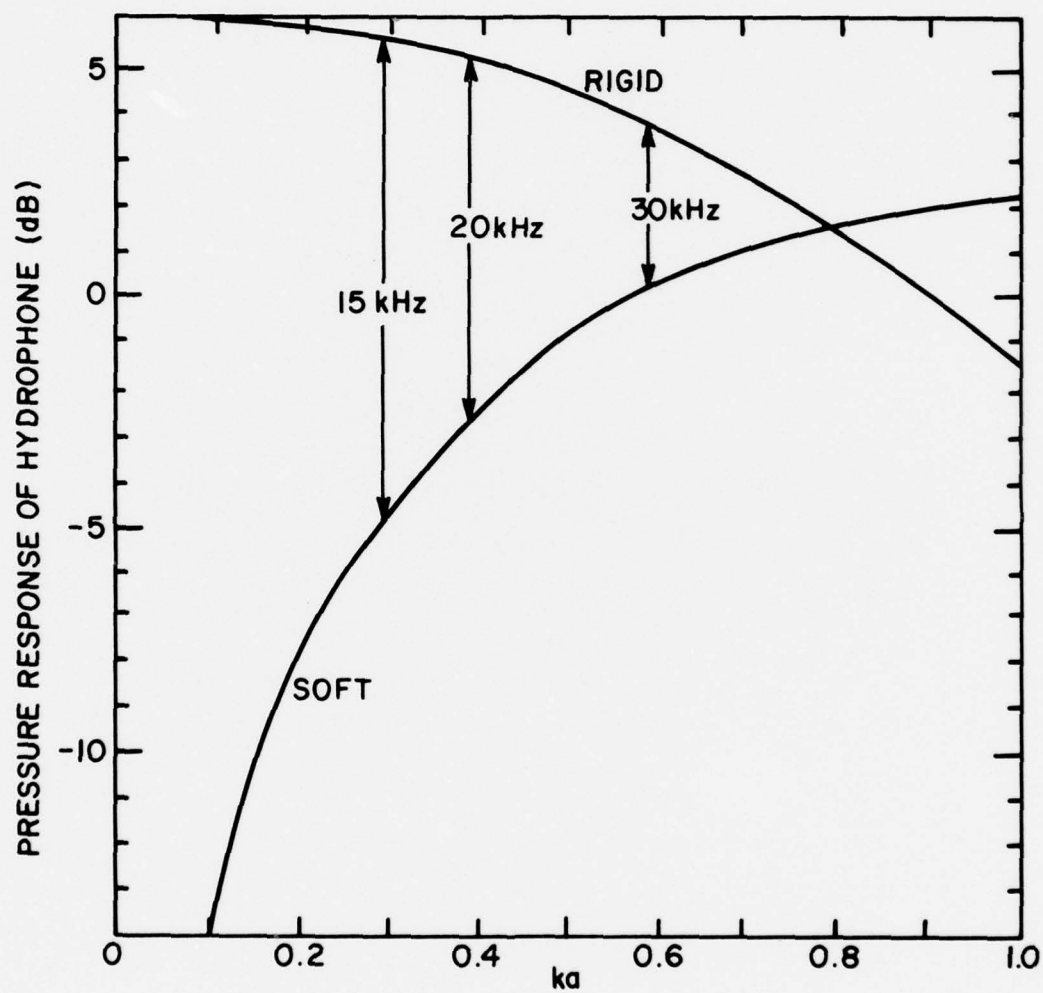


Figure 2.13 Pressure Response of a Receiver of Radius  $a$  Adjacent to a Soft and Rigid Surface.

The typical three-medium problem (Reference 31) for the transmission of sound is presented in Figure 2.14 for a soft surface where the second medium is air. The ratio of the transmitted signal amplitude  $A_3$  to the incident signal amplitude  $A_1$  is,

$$\frac{A_3}{A_1} = \frac{c_3}{c_1} \frac{2}{[(1 + m_1 m_2)^2 \cos^2(k_2 h) + (m_1 + m_2)^2 \sin^2(k_2 h)]^{1/2}}, \quad (2.65)$$

where  $m_1$  and  $m_2$  are the impedance ratios,

$$m_1 = \frac{\rho_2 c_2}{\rho_1 c_1}, \quad m_2 = \frac{\rho_3 c_3}{\rho_2 c_2}, \quad (2.66)$$

and  $k$  is the wave number,  $\rho$  is the density,  $c$  is the sound velocity and  $h$  is the thickness of Medium II.

If Medium I and Medium III are the same, such as water, a quantity called insertion loss is frequently used. Insertion loss is defined as the reduction of the signal, in decibels, caused by inserting the material between a sound source and a receiver in the absence of diffraction and refraction effects. It is given by

$$\text{Insertion Loss} = 20 \log \left( \frac{A_1}{A_3} \right). \quad (2.67)$$

Using Equations (2.67) and (2.65), it can readily be seen that for a plane wave normally incident on a plate immersed in water, the theoretical insertion loss becomes,

$$\text{Insertion Loss} = 10 \log \left[ \frac{(1 + m^2)^2}{4m^2} \sin^2 k_2 h + \cos^2 k_2 h \right], \quad (2.68)$$

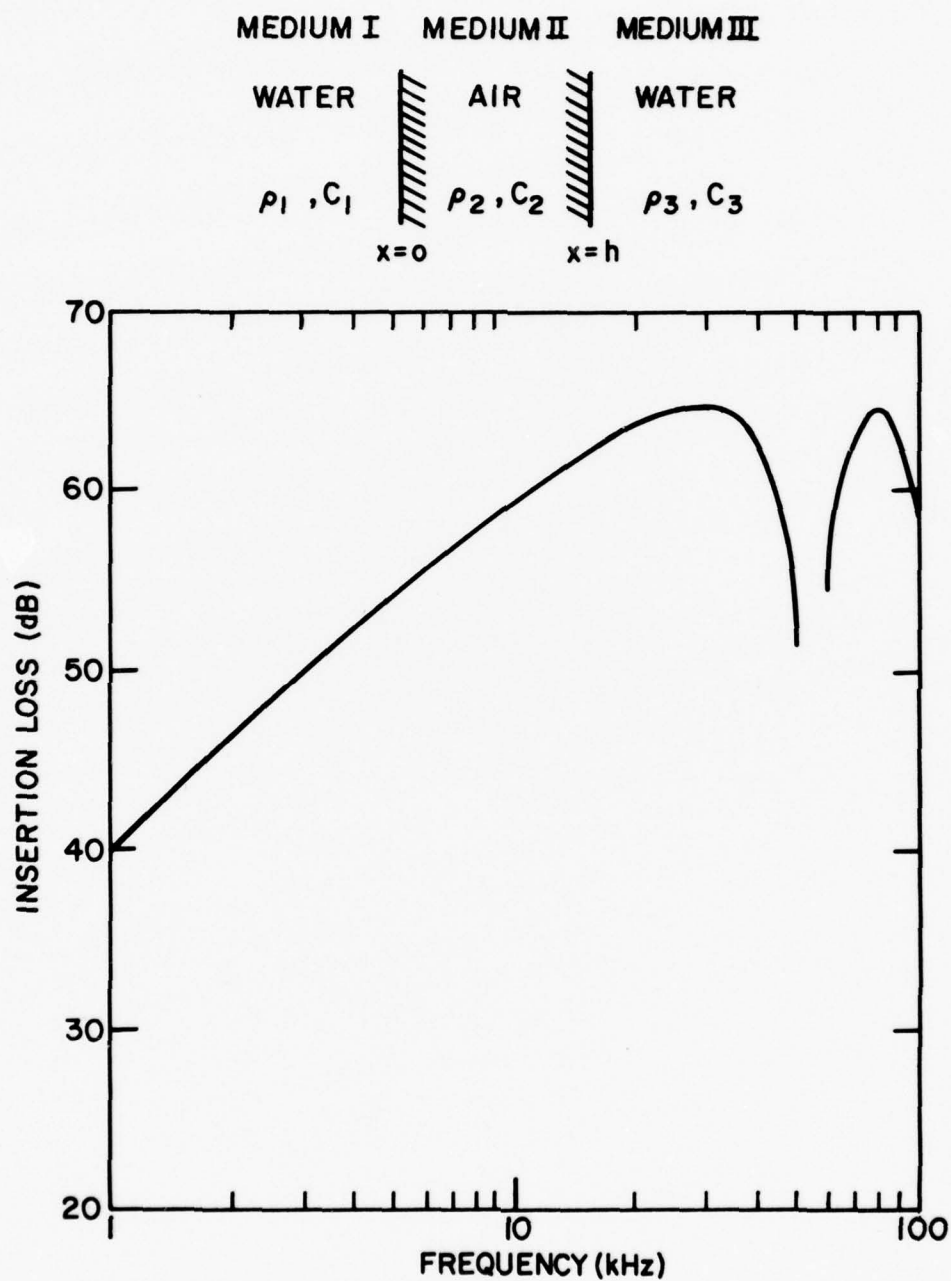


Figure 2.14 Insertion Loss Properties for a 1/8" Thick Layer of Air.



where  $m = \rho c / \rho_w c_w$ , which is the ratio of the characteristic impedance  $\rho c$  of the material to the characteristic impedance of water ( $\rho_w c_w \simeq 1.5 \times 10^6$  MKS Rayls). Equation (2.68) remains unchanged if  $1/m$  is substituted for  $m$ . Physically, this means a high impedance material can have the same insertion loss as a low impedance material where  $m$  for one material is the reciprocal of  $m$  for the other material,  $kh$  being the same for each case. The insertion loss becomes zero for a nonabsorbing material when the thickness is near a multiple of a half wavelength ( $kh = 0, \pi$ , etc.) or when a perfect impedance match exists ( $m = 1$ ). The maximum insertion loss occurs when the thickness is an odd multiple of a quarter wavelength ( $kh = \pi/2, 3\pi/2$ , etc.).

A soft material such as water or cell-tite neoprene has a characteristic impedance of  $\rho c = 415$  MKS Rayls. The maximum insertion loss for a water-air-water interface, where  $m = 2.8 \times 10^{-4}$ , is

$$\text{Insertion Loss(max)} = 65 \text{ dB(air)}, \quad (2.69)$$

and, for an 1/8" thick layer of air, occurs at a frequency of

$$f(\text{peak}) = \frac{c(\text{air})}{4h} = 32.7 \text{ kHz(1/8" air layer)}. \quad (2.70)$$

The insertion loss as a function of frequency for a 1/8" thick layer of air placed in water is plotted in Figure 2.14. The maximum insertion loss depends only on the impedance ratio and not on the material thickness. The frequency at which maximum and minimum insertion loss occurs depends only on the thickness.

A good rigid baffle should have an impedance ratio equal to the reciprocal of the soft baffle. It is not possible to achieve a large impedance ratio in water with a high  $\rho c$  material because of the relatively high  $\rho c$  of water. Steel has one of the highest values of  $\rho c = 39 \times 10^6$  MKS Rayls of all the common materials and can readily be used as a baffle. Tungsten has an impedance about twice that of steel but is expensive, more than twice as heavy, and only increases the insertion loss by 6 dB. The impedance mismatch between steel and air is  $10^4$  times higher than that for steel and water. It is for this reason that most of the experimental work on rigid baffles has been done in an air environment.

The maximum obtainable insertion loss for a water-steel-water interface where  $m = 26$  is

$$\text{Insertion Loss(max)} = 22 \text{ dB(steel)} . \quad (2.71)$$

Insertion loss as a function of frequency and for several thicknesses of steel in water is plotted in Figure 2.15. Although the insertion loss appears adequate for experimental purposes, the thickness required for low frequencies may make the baffle too heavy for practical considerations.

## 2.11 Baffle Vibration

Another effect which cannot be overlooked is that of plate vibration on the nearfield response of the hydrophone. It is possible that the hydrophone response could be affected by the flexural or bending waves set up in the baffle by acoustic interaction with the

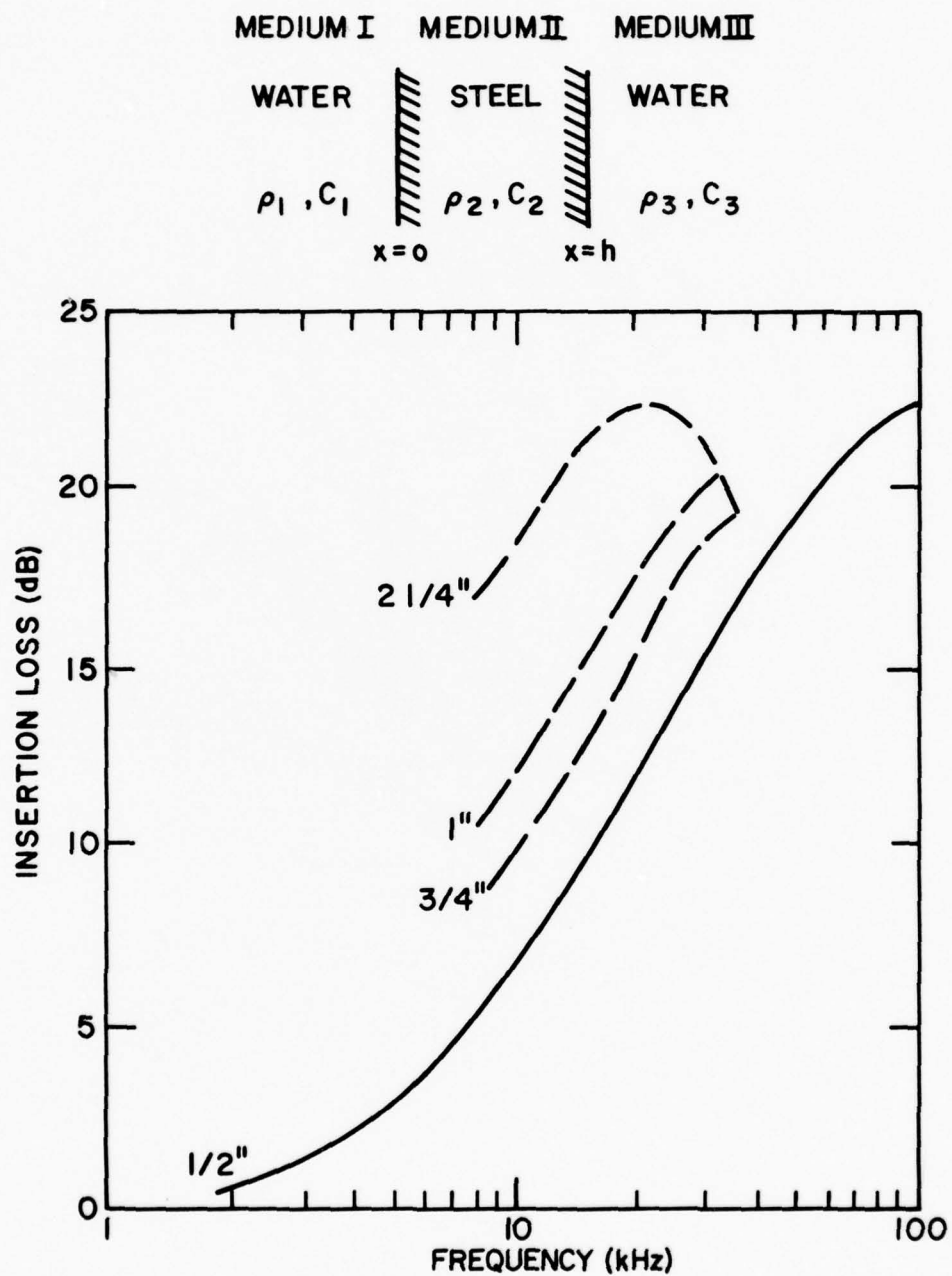


Figure 2.15 Insertion Loss Properties for Various Thickness of Steel.

incident sound wave. A rigid baffle is much more difficult to construct than a soft baffle since, in addition to maximizing the insertion loss, the vibrational modes of the structure must be eliminated or damped in the frequency range of interest in the experiments. If the baffle is allowed to vibrate at or near the test frequencies, then the hydrophone could be monitoring both the diffraction field and the near-field radiation of the structure and invalidate the tests.

If the plate is homogeneous and the vibration pattern a natural one (in contrast to a forced pattern that results if the plate is clamped along various lines), the distance between the nodal lines and also the bending wave number are functions of the frequency. The bending wave velocity is

$$c_B = \alpha \sqrt{\omega} \quad , \quad (2.72)$$

where

$$\alpha^4 = \frac{\lambda_E h^2}{12\rho(1 - \nu^2)} = \frac{c_p^2 h^2}{12} \quad (2.73)$$

and

$$c_p = \sqrt{\lambda_E / \rho(1 - \nu^2)} = c_{\text{bar}} \sqrt{\frac{1}{1 - \nu^2}} \quad . \quad (2.74)$$

The quantity  $c_p$  is the sound velocity for longitudinal waves in a thin plate,  $h$  is the thickness of the plate,  $\nu$  is the Poisson contraction,  $\rho$  is the density, and  $\lambda_E$  is Young's modulus.

For a steel plate, we have  $\nu = 0.28$  and  $c_{\text{bar}} = 5050$  m/sec which gives a plate velocity of  $c_p = 5260$  m/sec. For example, a 1/2-inch ( $1.27 \times 10^{-2}$  m) thick steel plate has

$$\alpha = (c_p^2 h^2 / 12)^{1/4} = 4.39 \quad , \quad (2.75)$$

and a bending wavelength of

$$\lambda_B = \frac{c_B}{f} = \frac{\alpha \sqrt{\omega}}{f} = \alpha \sqrt{\frac{2\pi}{f}} \quad (2.76)$$

where  $\lambda_B = 3.54''$ ,  $3.06''$ , and  $2.50''$  at the frequencies 15, 20, and 30 kHz, respectively. It is evident that to avoid bending resonance in the frequency range of the measurements, the baffle must be constructed as a mosaic of small steel squares, e.g., 2" on a side, with a compliant bond between each square.

A square which has edges of  $\ell = 2''$  long has a resonance frequency of

$$f_r = c_B/\ell = 2\pi\alpha^2/\ell^2 = 47 \text{ kHz} . \quad (2.77)$$

If one considers this square as a half-wave resonator, then  $f = f_r/4 = 11.7 \text{ kHz}$ . The experimental frequencies lie between these two resonance frequencies and, hence, a bending resonance will not affect the response characteristics of the hydrophone.

## 2.12 Diffraction from a Single-Edge Impedance Wedge

An example diffraction problem will now be illustrated which combines the theory presented in Sections 2.5, 2.6, and 2.7. Assume the diffraction wedge has a single  $90^\circ$  interior angle and semi-infinite surfaces which can have any impedance. Also, assume both surfaces have the same impedance. The geometry for ray path analysis will be the same as presented in Section 2.7 and Figure 2.11, with the receiver near the wedge surface and the source rotated about the edge.

In order to present a practical problem the normal distance from the point source to the surface will be taken to be  $\ell = 0.35''$  which is the approximate separation distance for the acoustic center of an LC-32 transducer in contact with the surface. With a wavelength of  $3''$  ( $f = 20$  kHz), the source-to-edge distance is 4 wavelengths ( $12''$ ) and the receiver-to-edge distance is 10 wavelengths ( $30''$ ). The receiver rotates from  $\theta = -90^\circ$  to the  $\theta = 180^\circ$  surface. The following equations are used; the direct and reflected pressure field is

$$P_o = \frac{e^{-jkb}}{b} + R_\xi \frac{e^{-jka}}{a} \quad 0^\circ \leq \phi < \phi_r \quad (2.78)$$

and

$$P_o = \frac{e^{-jkb}}{b} \quad \phi_r < \phi < \phi_i, \quad (2.79)$$

$$P_o = 0 \quad \phi_i < \phi < 2\phi_i, \quad (2.80)$$

and the diffracted field is:

$$P_d = P_i D(\phi, \phi') \sqrt{\frac{\rho}{s(\rho + s)}} e^{-jks} \quad 0^\circ \leq \phi \leq 270^\circ, \quad (2.81)$$

where  $\phi_i$  and  $\phi_r$  are the angles of the incident and reflected shadow boundaries and  $b, a$  are defined in Figure 2.11.

The total pressure field is given by,

$$P_t = P_o + P_d. \quad (2.82)$$



At the reflected ray shadow boundary  $\phi = \phi_r$ ,

$$P_t(\phi_r) = \frac{e^{-jkb}}{b} + R_\xi \frac{e^{-jka}}{2a}, \quad (2.83)$$

and at the incident ray shadow boundary  $\phi = \phi_i$ ,

$$P_t(\phi_i) = \frac{e^{-jkb}}{2b}. \quad (2.84)$$

The field incident at the diffraction point is,

$$P_i = \frac{e^{-jk\rho}}{\rho}, \quad (2.85)$$

where  $\rho = \sqrt{\ell^2 + d^2}$ . Equation (2.30) or (2.45) can be used for the diffraction coefficient.

By analyzing Figures 2.6 to 2.10 an understanding can be obtained of how the diffraction coefficient varies with impedance, angle of incidence, and distance (as a function of frequency) from the source to the diffracting point. A similar analysis of the single-edge diffraction problem will give insight to the more complex multi-edge problems and to the experimental data. The change in the directivity pattern at 20 kHz as a function of surface impedance is plotted in Figure 2.16, where  $P/P_o$  is the ratio of the received pressure to the free field pressure based on the separation distance when the source is directly above the receiver. When the impedance ratio is low ( $Z/\rho c = 0.1$ ), the surface is soft and a smooth directivity pattern results. Because of the soft surface, the far-field pressure is proportional to  $\cos \theta$  and has a

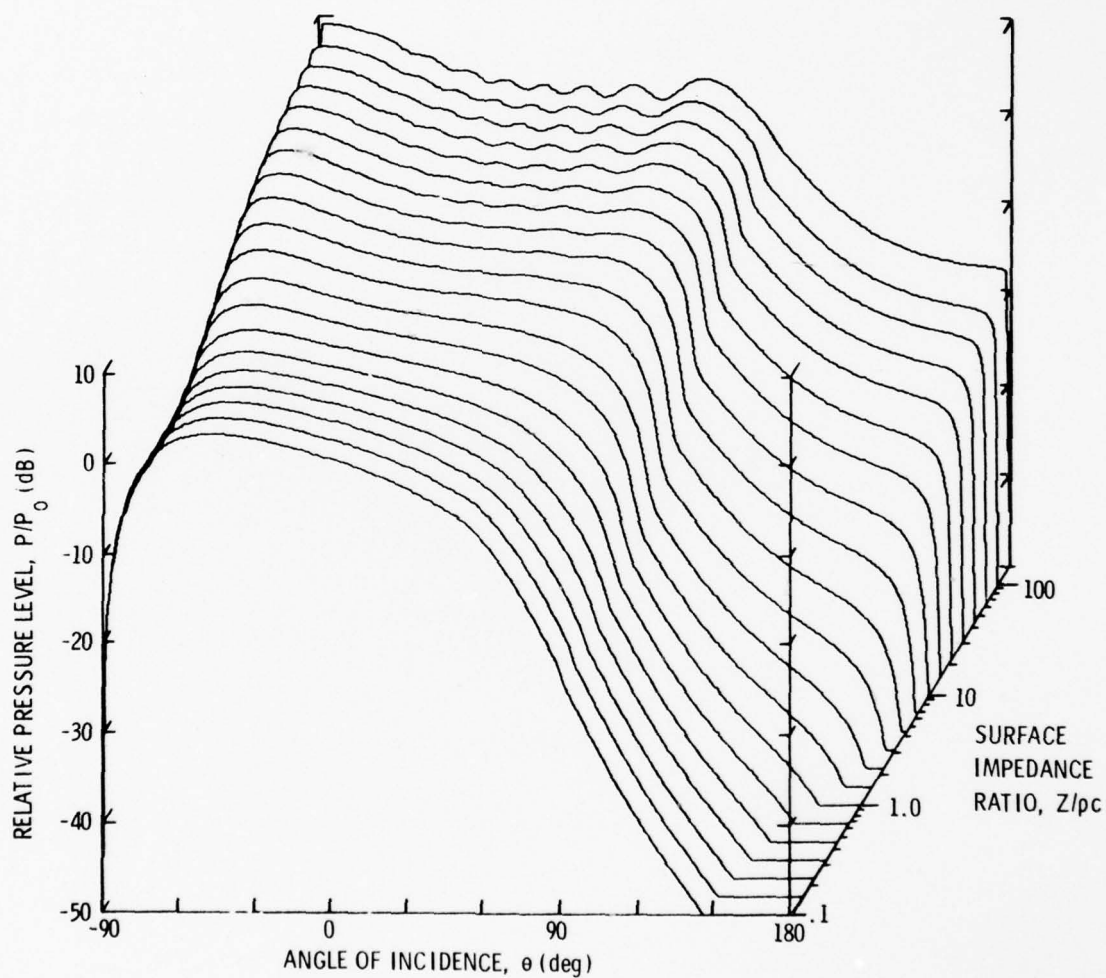


Figure 2.16 Calculated Directivity Patterns as a Function of Surface Impedance for a Single Diffraction Edge. Point Source is Near Surface and Four Wavelengths from Edge (20 kHz).

highly attenuated diffracted field. Hence, no ripples are present in the insonified regions. The angle of incidence from the source to the diffraction point, for this example, is about  $3^\circ$ . From Figure 2.10, it can be seen that the diffracted field for a small angle of incidence and a low impedance surface has a high, flat peak between the shadow boundary angles. This peak exactly compensates for the high incident field level [Equation (2.79)], as expected, and the continuous curves shown in Figure 2.16 result.

As the surface impedance increases, the level of the diffracted field in the shadow region increases and an interference effect causing ripples becomes evident in the insonified region. Figure 2.17 shows the same impedance dependence for a directivity pattern at 60 kHz. The drastic change from the relatively smooth soft impedance pattern to the rigid impedance pattern is caused by the source being positioned at a point whose distance from the surface is a significant fraction of a wavelength ( $0.35\lambda$ ). In addition to the large interference lobes present at a high impedance, ripples are generated by the diffracted field. Note that these ripples are more closely spaced than at 20 kHz. The source-to-edge distance is a larger number of wavelengths at the higher frequency, hence, the larger number of ripples.

In Figure 2.8(a), it was shown that the diffracted field for a rigid surface increases as the distance to the edge decreases. Figure 2.18 shows the same dependence for a source close to the surface of a rigid wedge. As the source moves closer to the edge, the number of ripples decrease and the level of the field in the shadow region increases. The diffracted field on a soft surface wedge increases in a similar

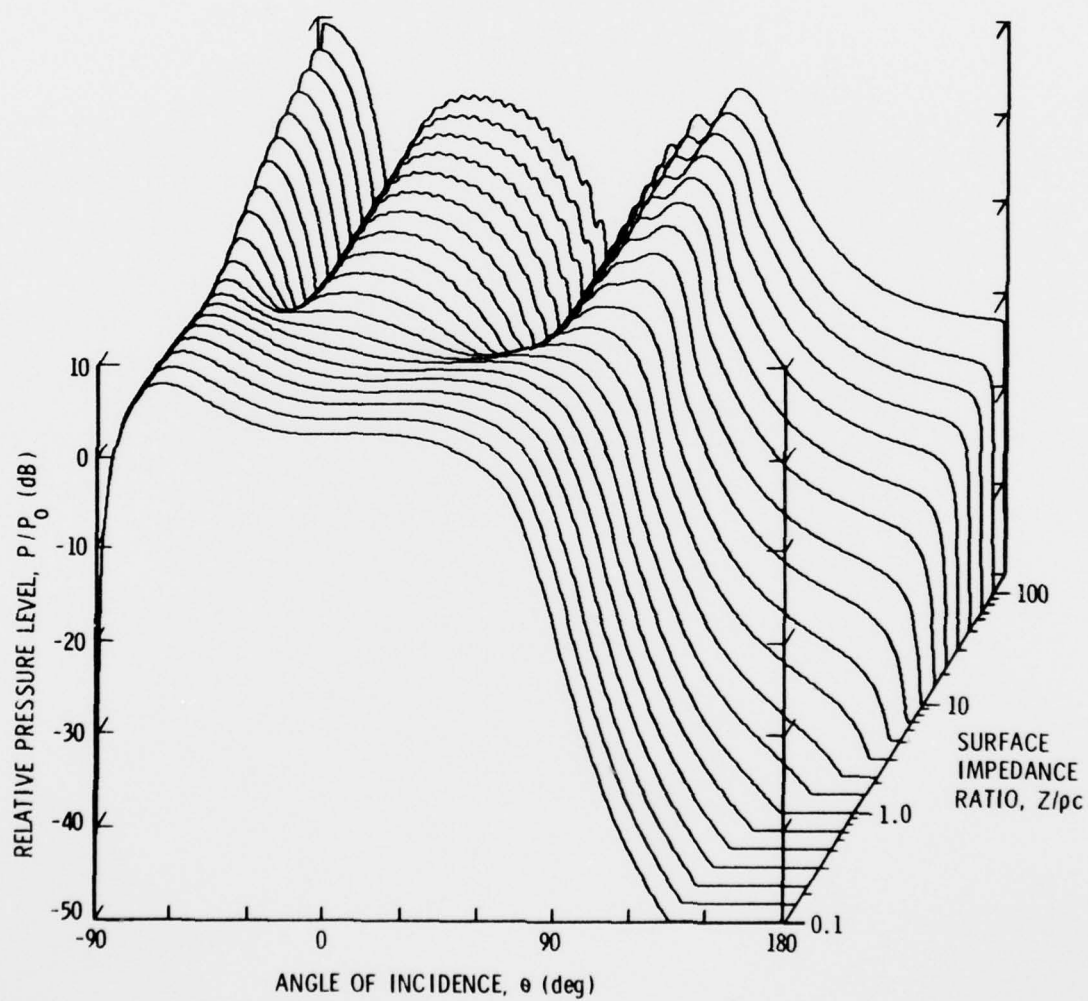


Figure 2.17 Calculated Directivity Patterns as a Function of Surface Impedance. Point Source is Near Surface and 12 Wavelengths from Edge (60 kHz).

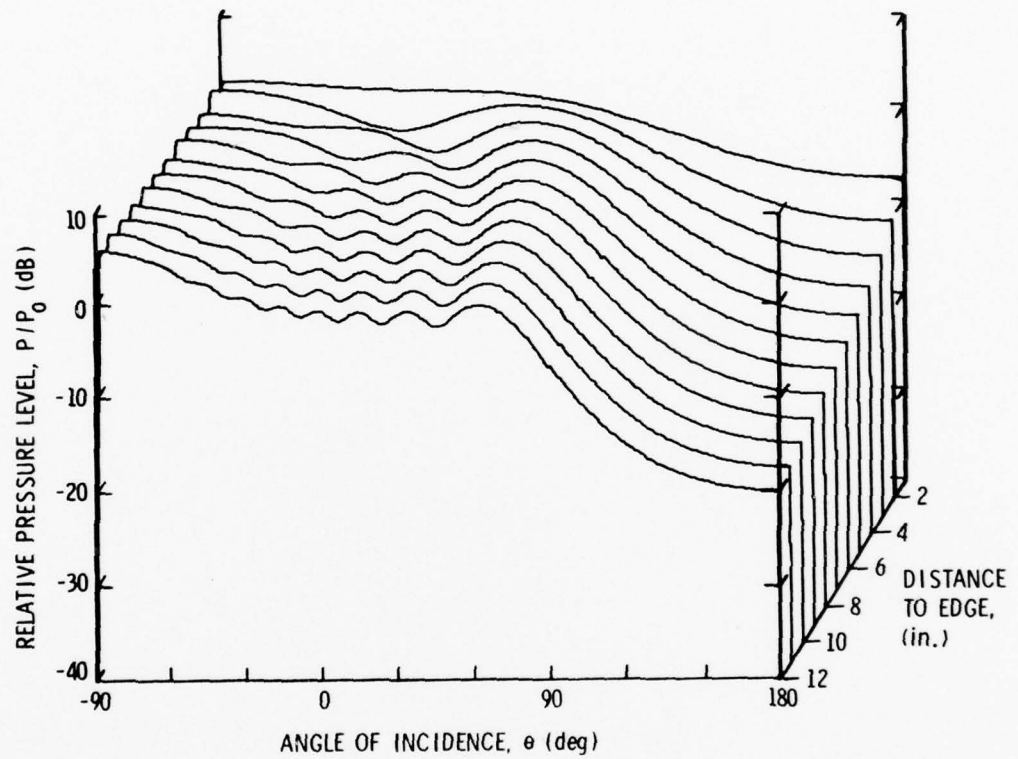


Figure 2.18 Calculated Directivity Patterns as a Function of Distance from the Edge on a Rigid Wedge. The Wavelength is 3".



manner as shown in Figure 2.19. Compare Figures 2.8(b) and 2.19 to see the contribution of the diffracted field.

Both Figures 2.18 and 2.19 were calculated using the Sommerfeld diffraction coefficient for a finite angle of incidence ( $\phi' \neq 0^\circ$ ). Figures 2.16 and 2.17 were calculated using the Malyuzhinets diffraction coefficient. Whenever any case of mixed boundary conditions is present, i.e., one surface impedance differs from the other, then the Malyuzhinets diffraction coefficient must be used. This is evident in Figure 2.20(a) where  $Z_+$  is soft and  $Z_-$  is hard. Even though the Sommerfeld coefficient is valid for either soft or hard wedges, it obviously gives a bad result for a mixed soft/hard wedge. The Malyuzhinets coefficient gives the expected diffraction pattern. Figure 2.20(b) shows the directivity pattern of  $Z_+$  hard and  $Z_-$  soft, opposite of the case used in Figure 2.20(a). Again, only the Malyuzhinets coefficient produces a realistic directivity pattern. Notice that in the mixed surface impedance problem, the pattern in the insonified region has a smooth dipole-like (i.e.,  $\cos \theta$ ) response when  $Z_+$  is soft, and a ripple effect when  $Z_+$  is hard, as expected when both surfaces of the wedge have the same impedance, e.g., Figure 2.16. The pattern response in the insonified region, therefore, has only a weak dependence on the impedance,  $Z_-$ , of the other wedge surface. Another fact to note is that the diffracted field is lower in Figure 2.20(a) than in (b), even though the soft surface diffraction coefficient is used, implying that the surface on which the source is located has the predominant influence on the directivity pattern.



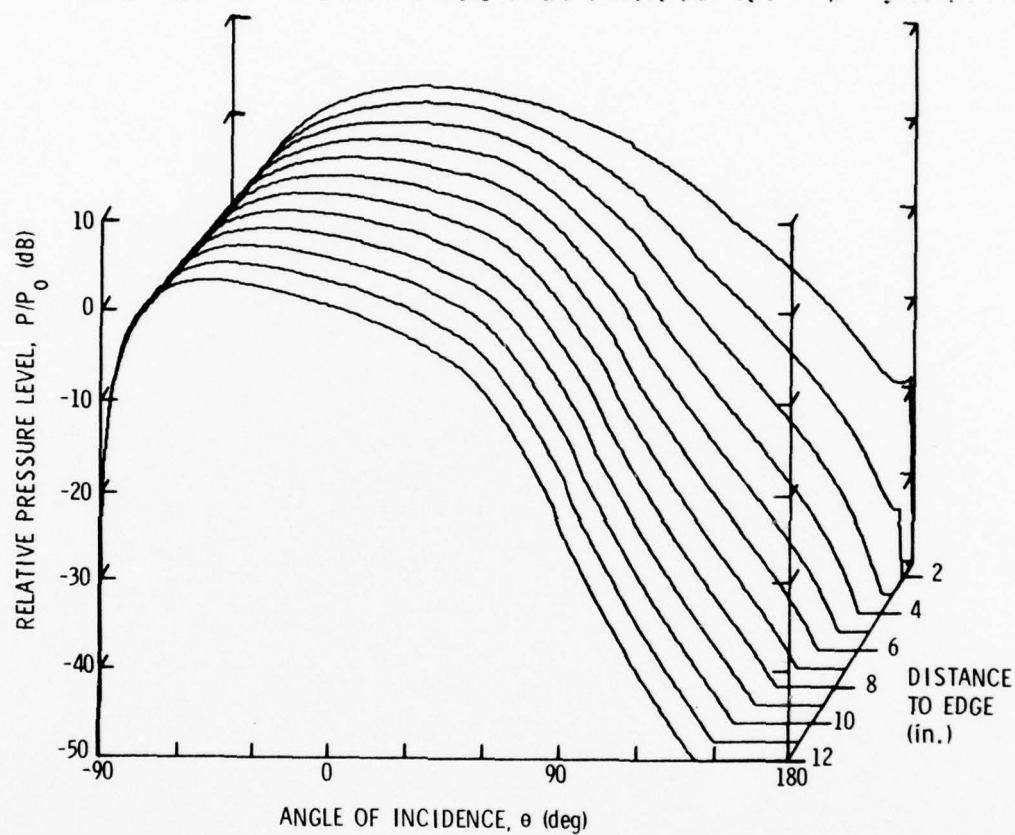


Figure 2.19 Calculated Directivity Patterns as a Function of Distance from the Edge on a Soft Wedge. The Wavelength is 3".

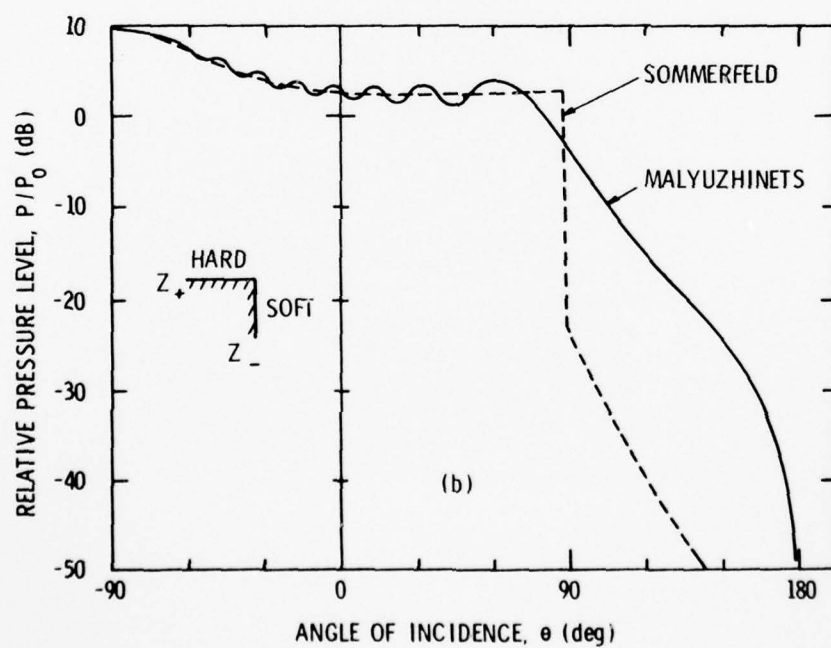
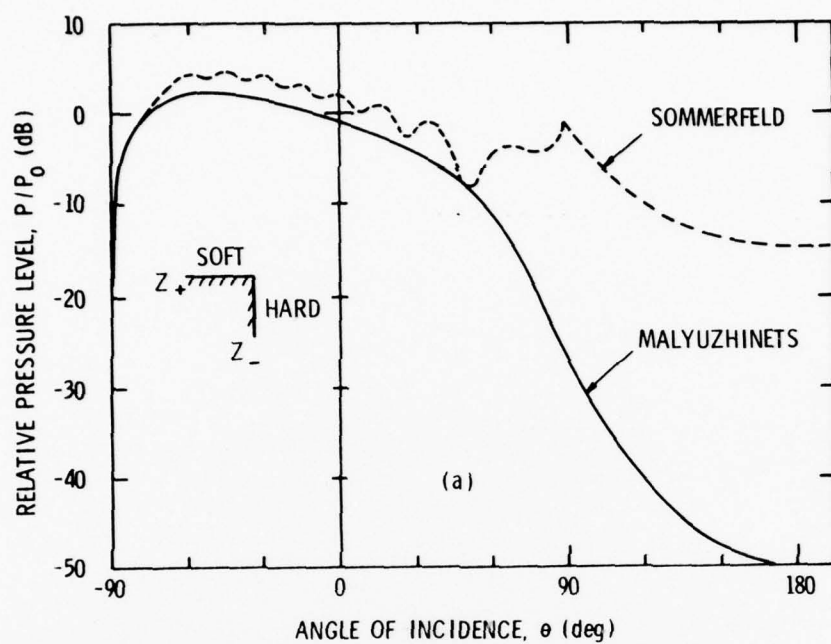


Figure 2.20 Calculated Directivity Patterns for Mixed Impedance Surfaces.

### 2.13 Multi-Edge Diffraction

Consider now a second diffraction problem which concerns the far-field directivity patterns of a point source on a two-dimensional baffle. A two-dimensional baffle can be used as a first approximation for any baffle in which the radius of curvature at the diffraction point is large compared to the wavelength. For illustrative purposes, assume a rectangular rigid baffle with the coordinate system referenced to the center of the upper surface. The distance across the baffle is  $\ell$  and the height of the baffle is  $H$ . With a source on the surface of a rigid baffle and the receiver at a large distance from the surface, the direct field will be,

$$P_o(\theta) = 2e^{-jkr \sin \theta} \quad -90^\circ < \theta < 90^\circ$$

and

$$\begin{aligned} P_o(\theta) &= e^{-jkr \sin \theta} & \theta &= -90^\circ, \\ & & \theta &= 90^\circ, \end{aligned} \quad (2.86)$$

where  $r$  is the distance from the center to the source.

The diffracted field from the right edge is

$$\begin{aligned} P_R(\phi) &= P_i^{(R)} D_s(\phi, \rho) \sqrt{\rho} e^{-j(k\ell/2) \sin \theta} & -90^\circ \leq \theta \leq 180^\circ, \\ & & \phi &= \theta + 90^\circ, \end{aligned} \quad (2.87)$$

where the incident field is  $P_i^{(R)} = \frac{e^{jk\rho}}{\rho}$ ,  $D_s(\phi, \rho)$  is the Sommerfeld diffraction coefficient, and  $\rho$  is the distance from the source to the right edge. At the left edge, the diffracted field is

$$P_L(\phi) = P_i^{(L)} D_S(\phi, \rho') \sqrt{\rho'} e^{j(k\ell/2) \sin \theta} \quad -180^\circ \leq \theta \leq 90^\circ ,$$

$$\phi = 90^\circ - \theta , \quad (2.88)$$

where the incident field is  $P_i^{(L)} = \frac{e^{jk\rho'}}{\rho'}$ , and  $\rho'$  is the distance from the source to the left edge. The right-back edge generates a far-field diffraction function

$$P_{RB}(\phi) = P_i^{(RB)} D_S(\phi, \rho + H) \sqrt{\rho + H} e^{-jk(\ell/2 \sin \theta + H \cos \theta)} ,$$

$$\theta \geq 0^\circ ,$$

$$\theta \leq -90^\circ$$

and

$$\phi = \theta , \quad (2.89)$$

the incident field at the diffraction edge being,

$$P_i^{(RB)} = P_i^{(R)} D_S(270^\circ, \rho) \frac{\sqrt{\rho}}{\sqrt{(\rho + H) H}} e^{-jkH} . \quad (2.90)$$

At the left-back edge, the diffracted field is

$$P_{LB}(\phi) = P_i^{(LB)} D_S(\phi, \rho' + H) \sqrt{\rho' + H} e^{jk(\ell/2 \sin \theta - H \cos \theta)} , \quad (2.91)$$

$$\theta \leq 0^\circ ,$$

$$\theta \geq 90^\circ$$

and

$$\phi = -\theta ,$$

the incident field at the diffraction edge being,

$$P_i^{(LB)} = P_i^{(L)} D_s(270, \rho') \frac{\sqrt{\rho'}}{\sqrt{(\rho' + H) H}} e^{-jkH} \quad (2.92)$$

Using the above equations, directivity patterns were computed for different source positions on a rigid baffle. These patterns are presented in Figure 2.21 for a baffle 18" wide and 14" in height. The frequency (20 kHz) has a wavelength of 3" and the patterns are plotted for the source placed at every one-inch position across the baffle. The presence of diffraction lobes in the shadow region is in contrast to the smooth curves as seen in the single edge diffraction patterns of Figure 2.18. Another significant observation is the degree of asymmetry present in the pattern when the source is located -8" from the center, i.e., one-third wavelength from the left edge of the baffle. The presence of an asymmetric pattern, such as this, for a source on a finite baffle was one of the motivating factors for this study. Similarities present in Figures 2.21 and 2.18 are the increasing level of the diffracted field as the source approaches one edge, and the ripple effect present in the insonified region. Superposition of the diffracted fields from both the right and left edges with the direct field results in the appearance of a complex ripple effect.

A limitation of the example just presented is that the Sommerfeld diffraction coefficient must be used. When an impedance surface or a mixed hard and soft wedge is considered, the Malyuzhinets diffraction coefficient must be used. But the Malyuzhinets coefficient for a finite impedance is equal to zero on the back surface, thus eliminating any contribution from the back diffraction edges. To ascertain whether a loss of information occurs by neglecting the back diffraction edge, i.e.,

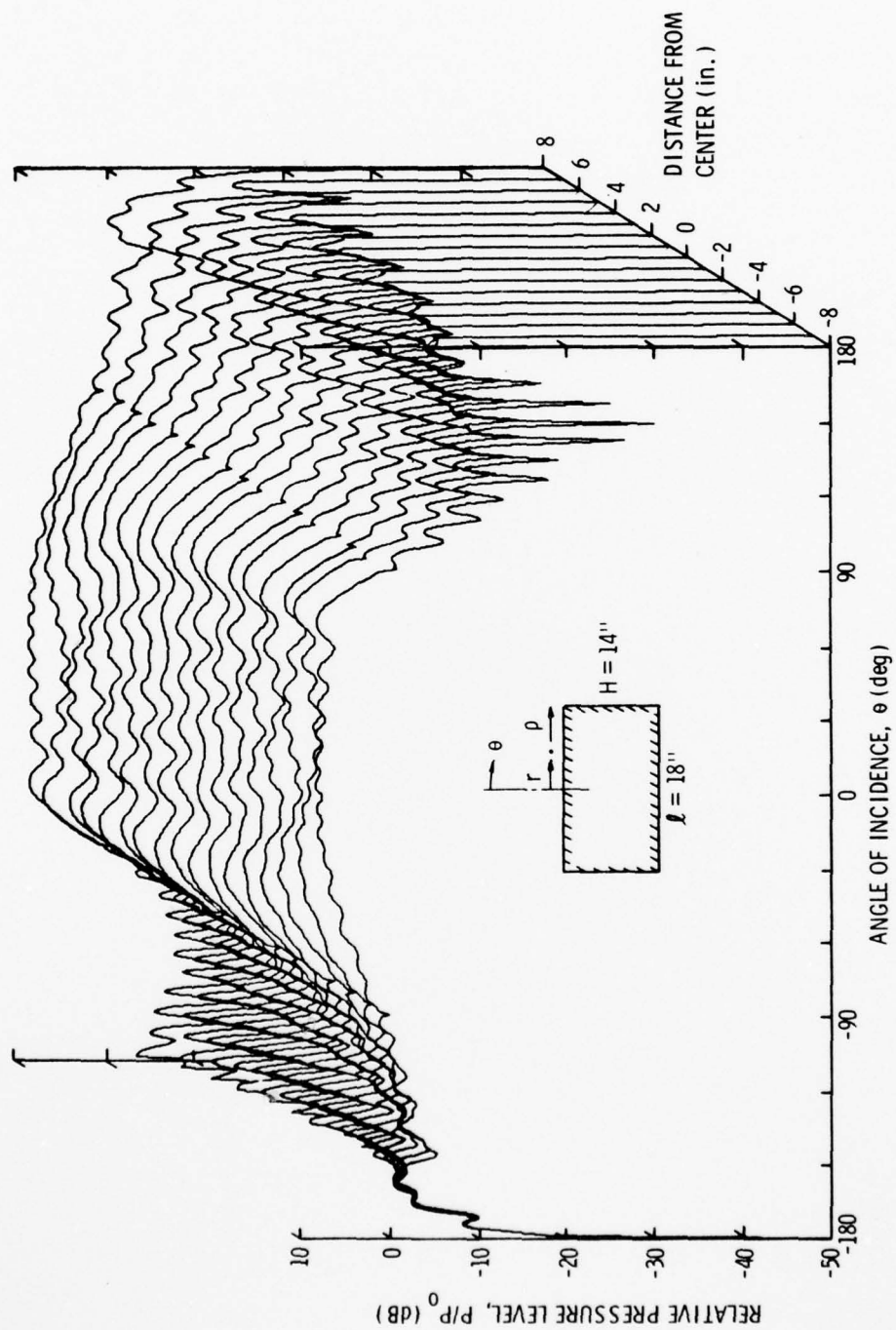


Figure 2.21 Calculated Far-Field Directivity Patterns for Various Source Positions on a Two-Dimensional Rigid Baffle. The Wavelength is 3".



where  $H$  goes to infinity, the far-field directivity patterns were plotted in Figure 2.22(a) and (b) for the source positioned in the center of the baffle and one inch from the right edge, respectively.

Neglecting the secondary diffraction at the edges in the shadow region does not appear to result in a loss of information. As expected, the directivity patterns obtained when  $H$  goes to infinity, now called the two-edge problem, closely match the four-edge problem in the insonified region and give an average level in the shadow region. The mismatch in levels at  $-180^\circ$  and  $+180^\circ$  in Figure 2.22(b), when averaged, provide a good match to the four-edge problem. Two advantages result from using a two diffraction edge analysis for comparison with experimentally obtained patterns. The smooth curve in the diffraction lobe region can be readily observed, making the theory-to-experiment comparisons easier. Secondly, finite impedance surfaces can be introduced by substituting the Malyuzhinets diffraction coefficient in place of the Sommerfeld coefficient. All comparisons of theoretical and experimental directivity patterns will be performed with the two diffraction edge model using the Malyuzhinets diffraction coefficient.

## CHAPTER III

### EXPERIMENTAL SETUP

#### 3.1 Hydrophone and Projector

The hydrophones used in the experiments were commercially available Atlantic Research LC-10 and an LC-32 transducer. They have small cylindrical lead zirconate titanate ceramics with diameters of 0.38" and 0.75" and sensitivities of -208 dB and -204 dB re 1 volt/ $\mu$  Pascal, respectively. Smaller hydrophones are available but require a preamplifier-cable driver which is mounted in a large housing. The large housing would possibly interfere with the diffraction field to a greater extent than the slightly larger LC-10 and LC-32. The LC-10 was used for all measurements on the finite "rigid" and soft baffles, while the LC-32 was used on the impedance wedge baffle where size was less important and a higher sensitivity was more important.

A directional high efficiency F-33 projector was utilized as the far field source for all tests involving the finite rigid and soft baffles. Another LC-32, a reciprocal transducer, was used as a projector for tests with the impedance wedge since an omnidirectional source was required.

#### 3.2 Impedance Wedge Baffle

The impedance wedge baffle was used for diffraction measurements in order to obtain a set of data for comparison with the field predicted by diffraction theory. The dimensions of the wedge baffle were such that

a single edge could be isolated, i.e., the direct and diffracted acoustic signal relating to one edge could be isolated from all other reflection and diffraction paths. The only care taken with the baffle was to prevent transmission through the material. An arbitrary impedance surface with dimensions such that one edge at a time could be analyzed was all that was required.

### 3.2.1 Material

The baffle was constructed out of 3/16" steel lined with a 1/8" layer of cell-tite neoprene. Cell-tite neoprene is a closed cell neoprene rubber which contains nitrogen. Nitrogen has about the same impedance properties as air. From Section 2.10, it can be seen that an adequate insertion loss was present to prevent transmitted signals from interfering with the tests.

### 3.2.2 Description

Two configurations of the baffle are shown in Figure 3.1. As can be seen by inspection, it was a closed triangular shaped baffle with two 75° sharp wedges and the third a 30° cylindrical wedge of 6" radius. The centers of rotation were located at the edge of the 75° wedge, as shown in Figure 3.1(a), and at the center of curvature of the cylindrical wedge. The source was positioned on a boom at a distance of 30" from the center of rotation. The receiver was located 12" from the center of rotation at an angle such that it just touched the baffle surface. The receiver remained fixed while the source was rotated about the axis.

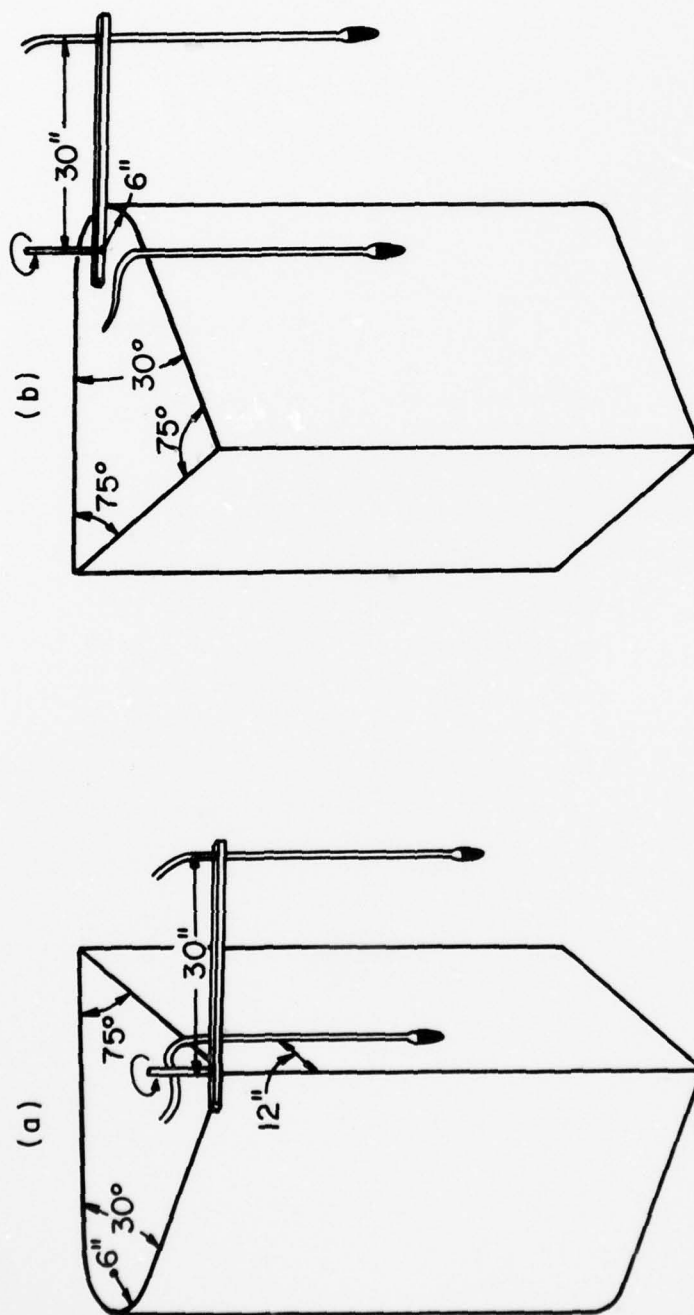


Figure 3.1 Wedge Baffle Configured to Study the Sharp Edge (a), and the Cylindrical Edge (b).

AD-A056 292

PENNSYLVANIA STATE UNIV UNIVERSITY PARK APPLIED RESE--ETC F/6 20/1  
DIFFRACTION EFFECTS OF BAFFLES ON ACOUSTIC DIRECTIVITY PATTERNS--ETC(U)  
NOV 77 W J HUGHES

N00017-73-C-1418

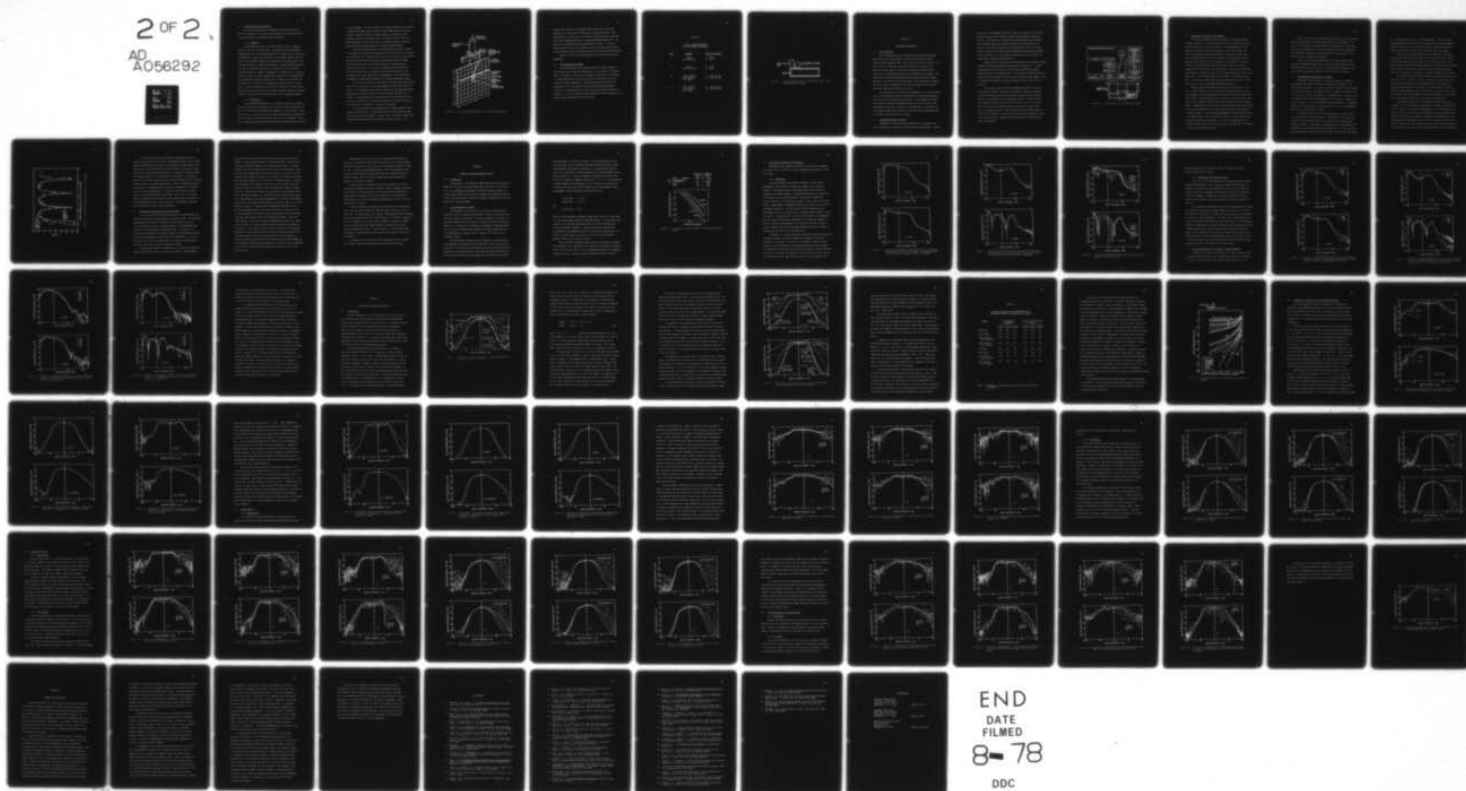
UNCLASSIFIED

TM-77-304

NL

2 OF 2

AD  
A056292



END  
DATE  
FILMED

8-78

DDC





### 3.3 Finite Rigid and Soft Baffles

The first considerations in designing finite baffles were to select the materials to be used for the rigid and soft surfaces and to avoid resonances in the frequency range of interest.

#### 3.3.1 Material

The analysis in Section 2.10 indicates that steel or tungsten should be used for the rigid baffle. Considering the weight handling capabilities of the training mechanisms used to rotate the baffles it was determined that tungsten was too heavy. The maximum insertion loss for steel (22 dB) appeared adequate for experimental purposes; however, the required thickness at 20 kHz (mid-frequency) to obtain maximum insertion loss was 2-1/4 inches, which was far too massive for the transducer training equipment to handle. Consequently, a thickness of 1/2 inch was selected so that the baffle remained thin compared to a wavelength while still providing sufficient insertion loss. Indeed, the insertion loss was shown to be sufficient by considering the pattern data of a rigid disk. It will be shown that in the case of the latter, the diffraction lobe level rises as the frequency increases, whereas insertion loss theory predicts a lowering of the diffraction lobes with increasing frequency.

#### 3.3.2 Description

To avoid bending resonance in the frequency range of the measurements, the baffle was constructed as a nine row by nine column mosaic of 2" x 2" x 1/2" steel blocks which were machined on all four edges. From Section 2.11, it can be seen that the nominal experimental frequencies of 15 kHz, 20 kHz, and 30 kHz lie between the first two resonances. Therefore, bending mode resonances did not affect the response characteristics

of the hydrophone. The steel squares were bonded together with pliobond, a rubber-based cement, which produced a good damping quality and also provided a degree of isolation between squares. This bond is quite compliant, however, which means that if the baffle mass had been too great (implying a thick plate), plate stretching could have occurred, opening gaps and causing the baffle to buckle during handling.

The probe was positioned on the square baffle as shown in Figure 3.2 by means of a small brass mounting unit which was held by a set screw to a long brass rod. The brass rod was, in turn, held by set screws into two stand-off posts which are loosely screwed into the steel blocks. This allowed the probe to be shifted easily to any other position relative to the baffle. These loose and numerous joints effectively isolated the probe from any possible structure-borne vibration with frequencies near those used during the experiments. This positioning arrangement was maintained throughout the entire experimental program.

The first soft baffle was rectangular, 48 inches long and 15 inches wide, with a thick cover of cell-tite neoprene into which the probe was 'buried'. All subsequent soft baffles consisted of the comparable rigid baffle with an 1/8-inch layer of cell-tite neoprene attached to its surfaces. This procedure was justified when it was determined that the directivity patterns of the probe were essentially identical whether it was placed into the neoprene or rested on its surface.

A disk was constructed by inscribing the largest possible circle within the square baffle. This produces both the rigid disk and, when covered with cell-tite neoprene, the soft disk. The finite cylinder was formed by attaching the disk to a massive cylindrical shell. The

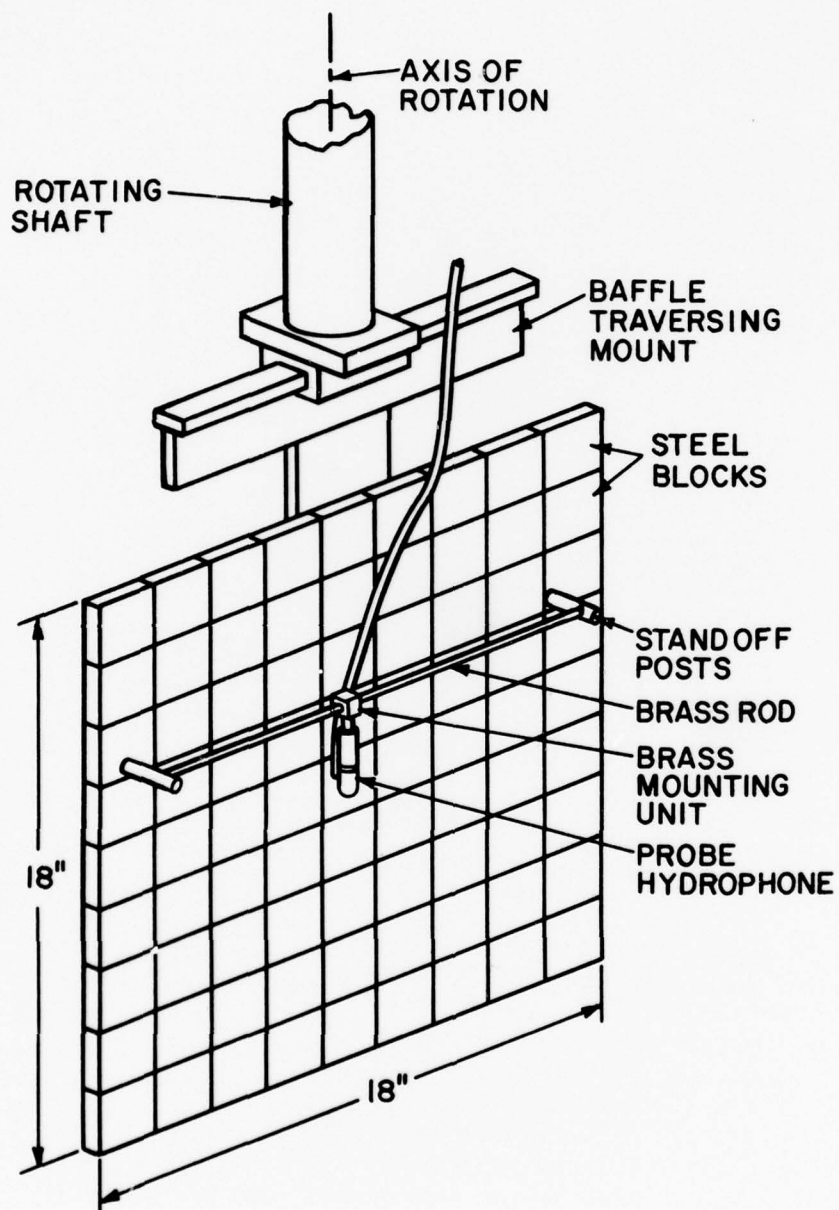


Figure 3.2 Probe Mounting Assembly with the Rigid Square Baffle.

cylinder was actually an internally braced frustrum of a cone with diameters of 18 inches and 21 inches and a massive back plate. The mounted disk, now an end cap, was isolated from the shell by a 1/4 inch soft rubber diaphragm backed by an internally mounted wooden disc. The addition of a massive back plate sealed the air cavity. It was not expected that the shell, via coupling from the incident acoustic waves, would contribute to the sound energy received by the measuring hydrophone.

Table 3.1 lists the baffle geometries tested and their surface impedances.

#### 3.4 Scattering Bars and Rings

The scattering bars and rings were made of a high  $\rho c$  material (steel) and a low  $\rho c$  material (polystyrene). Polystyrene, a closed cell foam, was ideal for a soft barrier exposed to water, since it retained its formed dimensions, was easy to work with and did not flex as the baffle was rotated underwater. Both materials used as barriers had dimensions of 1/2 inch high and 1/4 inch wide and were positioned around the circumference of the rigid circular and square baffles as in Figure 3.3. The soft baffle was not tested with a barrier because of its already high attenuation at the baffle edge.

TABLE 3.1

LIST OF BAFFLE GEOMETRIES  
AND THEIR SURFACE IMPEDANCES

<u>CASE</u>	<u>GEOMETRY</u>	<u>SURFACE IMPEDANCE</u>
I	disk (18" diameter)	A. rigid B. soft
II	square (18" on a side)	A. rigid B. soft
III	rigid cylinder (18" diameter) (15" long)	A. rigid end cap B. soft end cap
IV	soft cylinder (18" diameter) (15" long)	A. rigid end cap B. soft end cap



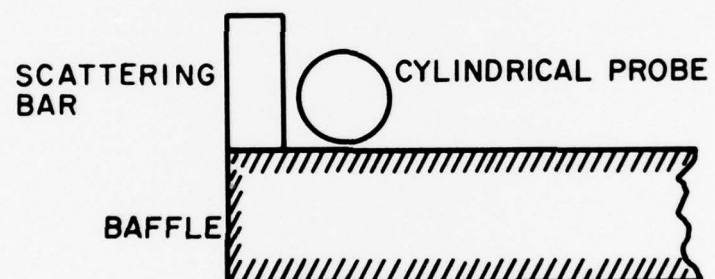


Figure 3.3 Cross-Sectional View of a Rigid Baffle with a Bar or Ring Mounted at its Edge.



## CHAPTER IV

### EXPERIMENTAL PROCEDURE

#### 4.1 Test Facilities

The experimental work was conducted using the Applied Research Laboratory's water-filled anechoic tank facility which has been in operation since September 1968. This concrete tank (26 ft. long, 17.5 ft. wide, and 18 ft. deep) has an anechoic wall liner of "Saper T" (a Goodrich acoustic liner) to reduce the reflection and reverberation levels, thus avoiding interference in each repeated pulsed signal. The tank itself is vibration-isolated from surrounding structures, being mounted on 3-inch-thick Korfund "Vibrocork." The average water temperature of the tank is approximately 22°C and the depth of the projector and baffle probe were normally set at 9 ft.

For beam pattern or directivity measurements of the finite baffles the test hydrophone and baffle were mounted on a telescoping positioner and rotated in the incident acoustic field. The hydrophone and baffle were oriented to achieve coincidence between the acoustic axis of the hydrophone and the axis of rotation of the positioner. Experiments on the impedance wedge baffle required a different rotating mechanism which would rotate the source about the baffle.

#### 4.2 Transmission Measuring System

Experiments in the restricted boundaries of an underwater test tank are made in the presence of reflections and reverberations. Energy

arriving at the hydrophone and baffle under test consists of the desired direct path energy plus undesired signals from extraneous reflecting objects. The system used to gather data discriminated between desired and extraneous signals by using pulse modulation and selective time gating. The receiver signal gate was positioned in time so that only a selected portion of the direct path propagation was passed and recorded without distortion. In the absence of the gating pulse, the input and output were isolated by more than 80 dB.

Signal control and recording was performed by the Scientific-Atlanta Automatic Transmission Measuring System shown in Figure 4.1. A pulse timing generator at the heart of the system controlled pulse widths, repetition rates, and sampling times. The oscillator output was directed into the Transmit Signal Gate which formed a pulsed transmit signal. The E-I Normalizer maintained a constant voltage or current level on the projector.

The received signal was first preamplified and then filtered to remove unwanted noise. By means of the Receiver Signal Gate and Peak Detector network any portion of the receive signal could be isolated, measured, and recorded on the Rectangular recorder. A polar recorder was available but was not used for two reasons. First, the recorded directivity patterns would have had to be adjusted in level to give  $P/P_0$ , the pressure ratio of field obtained with the baffle present to the free-field pressure. Polar plots cannot be easily adjusted in level after being recorded. Moreover, better resolution of the diffraction lobes are obtained.

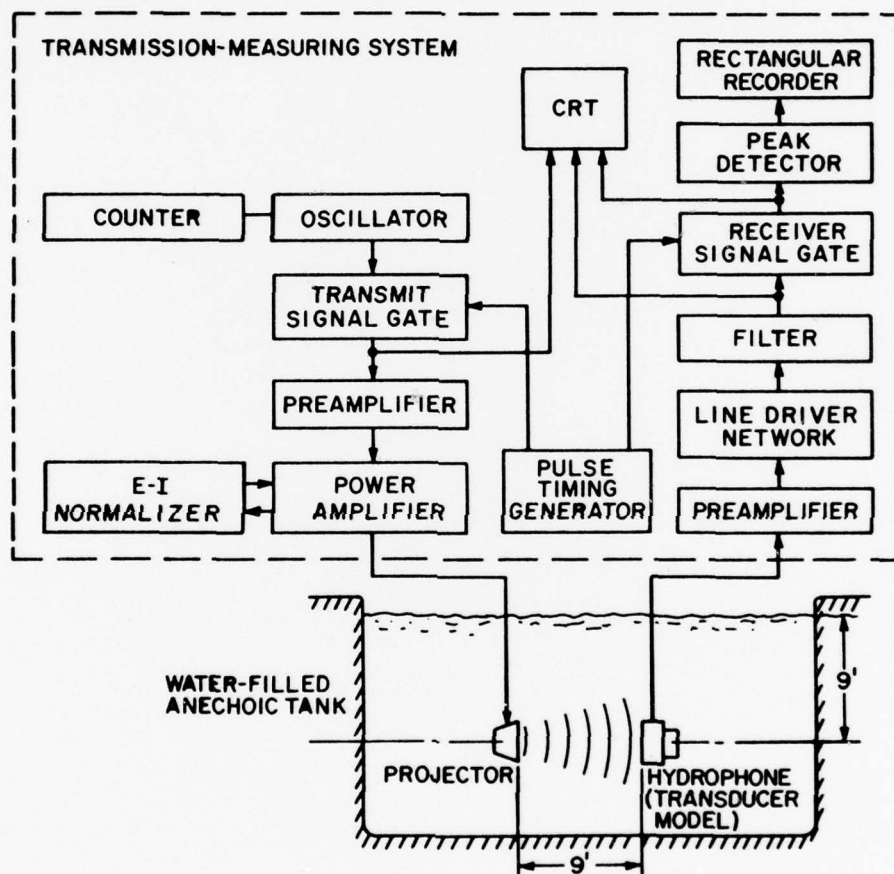


Figure 4.1 Block Diagram of the Experimental Setup.

#### 4.3 Experimental Technique and Procedure

The square and disk baffles were mounted on a movable carriage, as shown in Figure 3.2, which allowed the baffle to be moved in a transverse direction from the axis of rotation. The hydrophone was first mounted on the baffle a specific distance from the baffle edge. The entire baffle-probe unit was then shifted to align the acoustic center of the hydrophone with the axis of rotation. The cylindrical baffle, however, was too massive for the procedure to be followed. The axis of rotation was therefore positioned close to the baffle face giving a maximum radius of 10 inches to the hydrophone. Since the projector was positioned at a distance of nine feet, for these experiments, the error in angle was  $\sim 6^\circ$  for incident angles of  $0^\circ$  and  $180^\circ$ . No error occurred at  $90^\circ$ . It was felt that analytical difficulties should not occur if this angle error is kept in mind when comparisons are made.

When the probe was removed from the axis of rotation, as in all of the finite cylinder tests, the projector-hydrophone distance varied as the angle of incidence changed; hence, the receive pulse arrival time also varied. The gate which was set to measure a certain portion of the receive pulse remained fixed in time since it was set on the instrument panel. Consequently, the total effect observed was that the gate position on the pulse envelope shifted along the pulse envelope as the angle of incidence changed. Since the analyzing equipment recorded the peak value of the gated signal, care was exercised so that at no time did the gate include the pulse cutoff transient. In order to compensate for the different arrival times of the received pulse, the gate had to be adjusted in time as the baffle was rotated.

Prior to filtering, the waveshape was distorted by a high frequency harmonic (approximately 100 kHz) whose source was the projector. The source of this harmonic was established by observing that, if the probe was raised or lowered by one foot, the harmonic distortion disappeared. This indicated a highly directional pattern which was expected if the projector were introducing the harmonic.

Some of the problems mentioned above were also present during tests on the impedance wedge baffle. The experimental techniques and procedures for the wedge baffle were relatively simple compared to the finite baffles because the projector was rotated about the wedge.

#### 4.4 Hydrophone Position Relative to Surface

Experiments were conducted to resolve the potential problem of mounting the LC-10 probe on the finite rigid and soft baffles. Two options were available: 1) to mount the probe a distance of one diameter into the test surface, a flush-mount; and 2) to mount the probe so that it rested on the surface of the baffle, a surface-mount. In Section 2.9, the response level of a finite hydrophone for the case of a normal incidence is derived. It is very possible that the response of a hydrophone mounted on the surface will not be equivalent to that of the hydrophone whose face is flush with the surface.

A groove was cut into the cell-tite neoprene in order to mount the probe flush to the baffle surface. Positioning of the probe in the recess of the soft surface was critical because of the existing high pressure gradients. Difficulty in repeating accurate positioning of the hydrophone led to pressure response variations of 4 to 5 dB. To reduce these variations, the probe was mounted inside and flush with the surface



of a one-inch-wide section of the baffle material. Since the probe always remained in this section, the variations due to slight geometry changes were reduced. The probe and container could then be shifted across the baffle in discrete steps in order to scan the surface.

The first step in determining the level response of the finite probe was to check the standing wave pattern set up by the soft surface. A soft surface best shows the effect of the finite probe size. Both pulsed and CW (continuous waveform) signals were used to set up a standing wave in front of the baffle. Figure 4.2 shows the relative pressure level as a function of  $ka$  taken in a direction normal to the surface.

The initial position for the hydrophone was flush with the surface. The solid line is a plot of  $2 \sin kr$  for fresh water at 22°C and has been shifted to match the first experimental null. The difference between experimental data and the curve can be attributed to the fact that the surface impedance is not truly zero as it would be for an ideal soft surface. The high response at very small distances is most likely due to scattering from the slot cut into the baffle surface.

When using a rigid baffle, the problems encountered were quite different. In this instance, no high-pressure gradients occurred at the surface. However, by recessing a hydrophone into a slotted section of the 1/2" baffle, leaving only 1/8" thickness of steel, a problem of low insertion loss arose. In addition, a problem of repeatability occurred when moving the hydrophone and steel block to different positions on the baffle. Problems were also evident with bond quality and the presence of air bubbles, not to mention the time consuming aspect of the procedure.



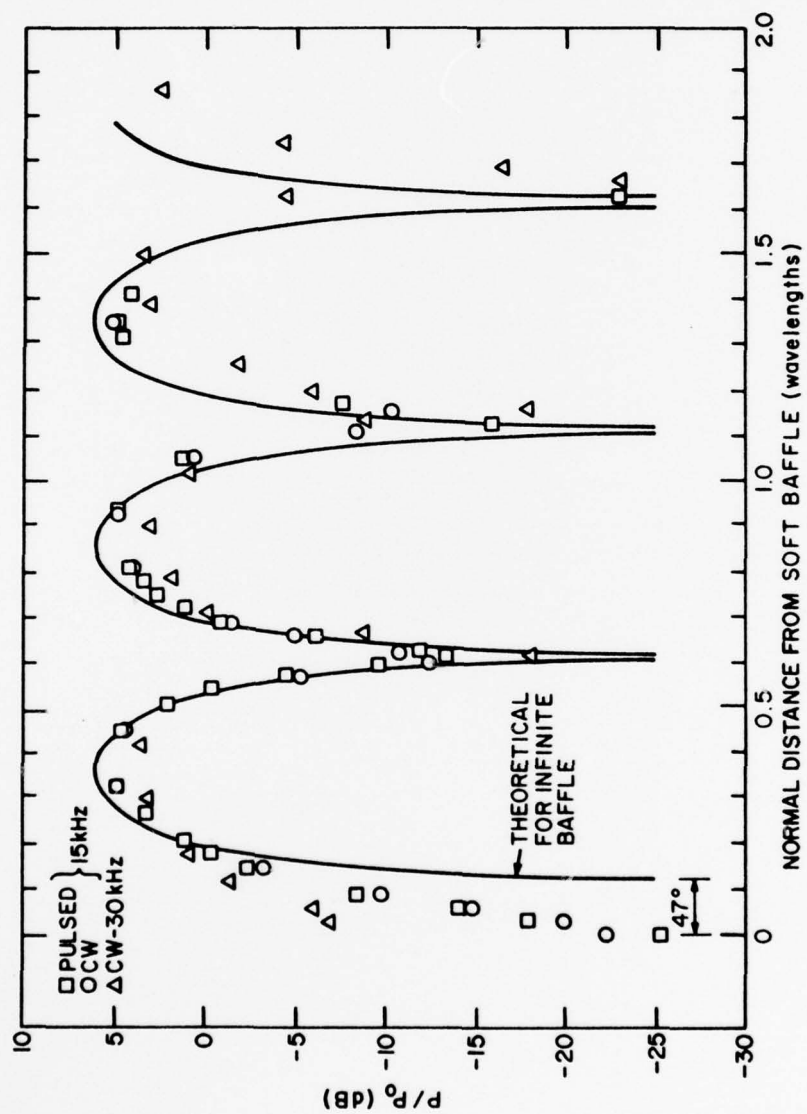


Figure 4.2 Standing Wave Formed in Front of a Soft Baffle.

The second option involved mounting the hydrophone so that it rested on the surface of the baffle. Repeatability checks on the surface-mounted hydrophone were very good, thus avoiding the major problem of the buried probe. Directivity patterns were recorded for each type of probe mounting to determine whether differences in response at different angles of incidence existed. The patterns will be discussed in a following chapter, but the data shows that there is little difference in the patterns between surface- or flush-mounted probes. Indeed, the data when plotted as a function of wavelength appear relatively independent of frequency, as well as probe mounting style. A check was also made with a rigid baffle and the same conclusions were drawn. In the case of the rigid baffle, repeatability of data with the buried probe was very inferior to the surface-mounted probe. All of the data to be analyzed, therefore, were obtained by a surface mounted hydrophone.

#### 4.5 Experimental Problems and Sources of Errors

It is a well known fact that the presence of air bubbles may constitute an appreciable loss mechanism for acoustic energy. The attenuation resulting from the presence of bubbles seriously distorts both the directivity patterns and the frequency response of the hydrophone and can lead to the accumulation of misleading data. Fortunately, this problem can be minimized by carefully "wetting" the hydrophone and baffle with a special detergent solution before each submergence. It is not necessary to wet the soft surface since the formation of bubbles will have very little effect on the low impedance surface.

A smooth metal surface is reasonably easy to maintain bubble-free, however, the baffles used in this study are a mosaic of small squares

and the Pliobond joints between these squares can easily trap some air bubbles. Using sufficient caution in wetting the surface prevented the occurrence of bubble problems on the rigid disk and square. A serious problem arose for the rigid end cap on the finite cylinder where a large air cavity was present behind the end cap surface. It was felt that the Pliobond joints between the mosaic steel blocks of the baffle would hold under the water pressure of 4.5 lb/sq. in. (9' depth of water). However, when the pressure was integrated over the area of the baffle face, the force was found to be 1100 lbs. which could seriously weaken the mosaic structure. During initial tests, the contained air found pinhole cracks in the bonding and leaked out to the baffle surface causing bubble problems. These pinhole leaks allowed enough water to seep into the housing, reducing the total inward force present on the baffle's face. All of the holes were sealed to eliminate these troublesome air bubbles and the baffle was submerged again. The bonds on a portion of the baffle were not strong enough to withstand the total water pressure and were sheared, caving the steel squares inward and flooding the housing. After this tragic episode, a 1/4" natural rubber diaphragm was bonded to the inside of the circular end cap and a support system was installed to withstand the pressure. This rubber provided a seal to prevent air from escaping through the end cap joints and also provided a vibration isolation from the wooden support disk which was braced between the end cap and an internal housing flange to maintain structural integrity during immersion. This mechanical configuration performed well as long as care was maintained to assure that no air bubbles were present on either the probe or the baffle surfaces.

Experimental errors, in general, are expected to increase with frequency, to increase at points near the edge due to the large pressure gradients existing there, and to decrease with increasing absolute values of  $P/P_0$ . This was noted experimentally in that the measurements conducted at 15 kHz generally appear more stable and repeatable than did those at 30 kHz. Also, air bubble problems were more prevalent and dramatic at the higher frequency.

Another source of potential error which was difficult and time-consuming to eliminate involved the effects of small frequency variations on the pattern. The oscillator in the system permitted resolving the frequencies of 15 kHz and 20 kHz to within  $\pm 20$  Hz, and 30 kHz  $\pm 50$  Hz. Patterns were run at small incremental frequencies near each of the test frequencies of interest.

A 100 Hz increase in frequency from 30 kHz caused the diffraction lobes to shift inward slightly in angle and varied in level by no more than 2 dB. The patterns were very similar, indicating that small frequency errors should have little effect on the patterns. At 20 kHz, a change of 40 Hz in frequency had a slight effect at angles of incidence of  $\pm 144^\circ$  where the diffraction lobe changed shape but remained near the same angular positions and levels. A 40 Hz change at 15 kHz produced almost no changes of the pattern, and indeed was the most stable of the three frequencies.

In general, for all frequencies, the repeatability was excellent in the major lobe area and was good in the diffraction lobe area.

## CHAPTER V

### IMPEDANCE WEDGE EXPERIMENTAL RESULTS

#### 5.1 Introduction

A description of the impedance wedge baffle has been presented in Chapter III and the theoretical background in Sections 2.5 to 2.8 and 2.12. The experimental measurement procedure is shown in Figure 3.1. Acoustic path lengths and receive gate sampling were checked in order to verify that only one edge of the baffle played a significant role in the directivity patterns obtained.

#### 5.2 Surface Impedance of Baffle

The impedance of the surface of the baffle is one of the most important material parameters needed before accurate calculations of the directivity pattern can be made. The surface impedance of a baffle is generally dependent upon the angle of incidence or angle of reflection. Moreover, it is important to determine the impedance at grazing angles since the field at these angles determine the shadow region level and the response beyond an angle of  $\pm 70^\circ$ . Figure 2.11 is used for the coordinate system.

The near-grazing incidence surface impedance can be determined experimentally by placing two LC-32 transducers (one a source and one a receiver) on the surface and recording their response levels as they are separated. It was determined that the baffle was sufficiently large so that the diffracted field from the edges was low enough to not affect



the measurements. The acoustic centers of both transducers were 0.35" from the surface and the received pulse was recorded at several separation distances, then plotted in Figure 5.1. Using equations given in Section 2.8, theoretical curves were generated for the experimental case shown in Figure 5.1. Since the impedance is unknown an iteration over all real and imaginary impedance values from  $\rho c$  to  $34 \rho c$  was performed. A complex impedance was determined for each frequency by selecting the resulting field which most closely agreed with the experimental values. The impedance ratios obtained from this selection are:

$$Z/\rho c(10 \text{ kHz}) = 3 + j6 ,$$

$$Z/\rho c(20 \text{ kHz}) = 10 + j3$$

and

$$Z/\rho c(30 \text{ kHz}) = j19 .$$

These are only approximate impedance values since there is a broad range of values which closely match the experimental data. At large separation distances, the received level falls off at the rate of approximately 10 dB per doubling of distance. The data obtained for 60 kHz were inconclusive so the impedance value at 30 kHz will be used instead. The field on a rigid surface falls off at a rate of 6 dB per doubling of distance and on a soft surface at 12 dB.

Many references deal with sound reflection from surfaces, however, there appears to be no analysis in the literature concerning the attenuation of a wave front close to or on an impedance surface as it propagates along the surface. This is an area which requires further research.



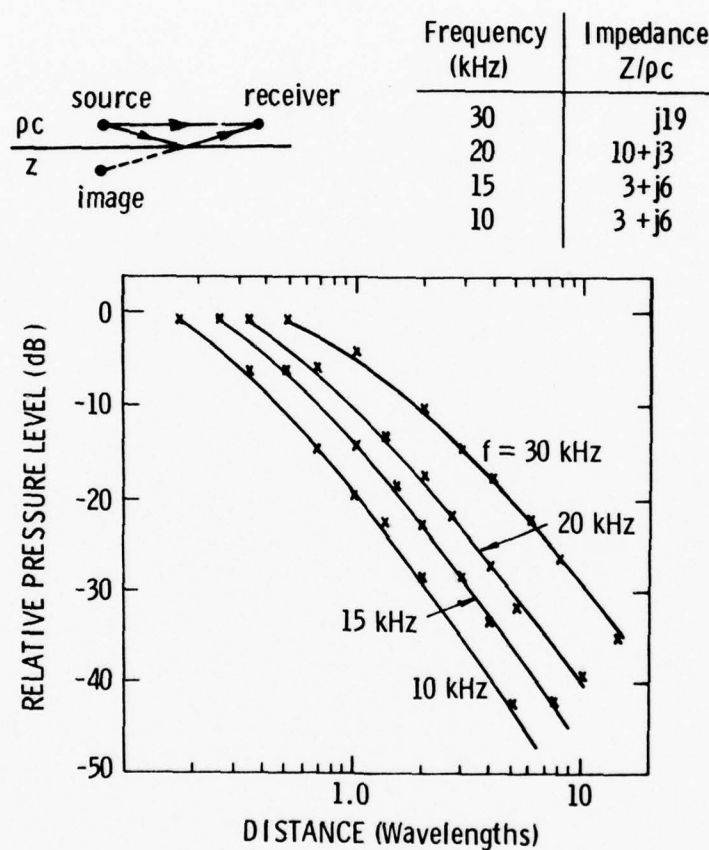


Figure 5.1 Attenuation Along the Surface of the Impedance Wedge Baffle

### 5.3 Directivity Patterns for a Sharp Edge

Experimental and theoretical directivity patterns are presented for a point source located 0.35" from an impedance surface and 12" from a 75° wedge.

#### 5.3.1 Sharp Edge

Directivity patterns are shown in Figures 5.2 and 5.3 where experimental (solid line) and theoretical (dashed line) curves are compared. The general shape of the patterns match well in both the illuminated and shadow regions. An especially good match is present for the ripples in the illuminated region. Notice that the number of ripples increases as the frequency increases. This is due to the source being a larger number of wavelengths away from the edge of the baffle at the higher frequencies. The only region in which theoretical and experimental levels do not match well is between incident angles of about 60° and 90°. A possible source of error could be due to the assumption that the surface impedance is independent of the angle of incidence. A method of obtaining the impedance as a function of incidence angle is needed. However, the grazing incidence impedance used here is useful in determining the level of the diffracted field.

In Figure 5.4, several theoretical patterns are depicted which show the manner in which the pattern changes with changes in the source distance to the surface. At 20 kHz, as the source is moved to larger distances from the surface, the illuminated region shows more evidence of interference effects and the shadow region exhibits a higher diffracted field level. At 60 kHz, positioning is very critical as can be seen in the calculated curves. The closer the source is to the surface, the

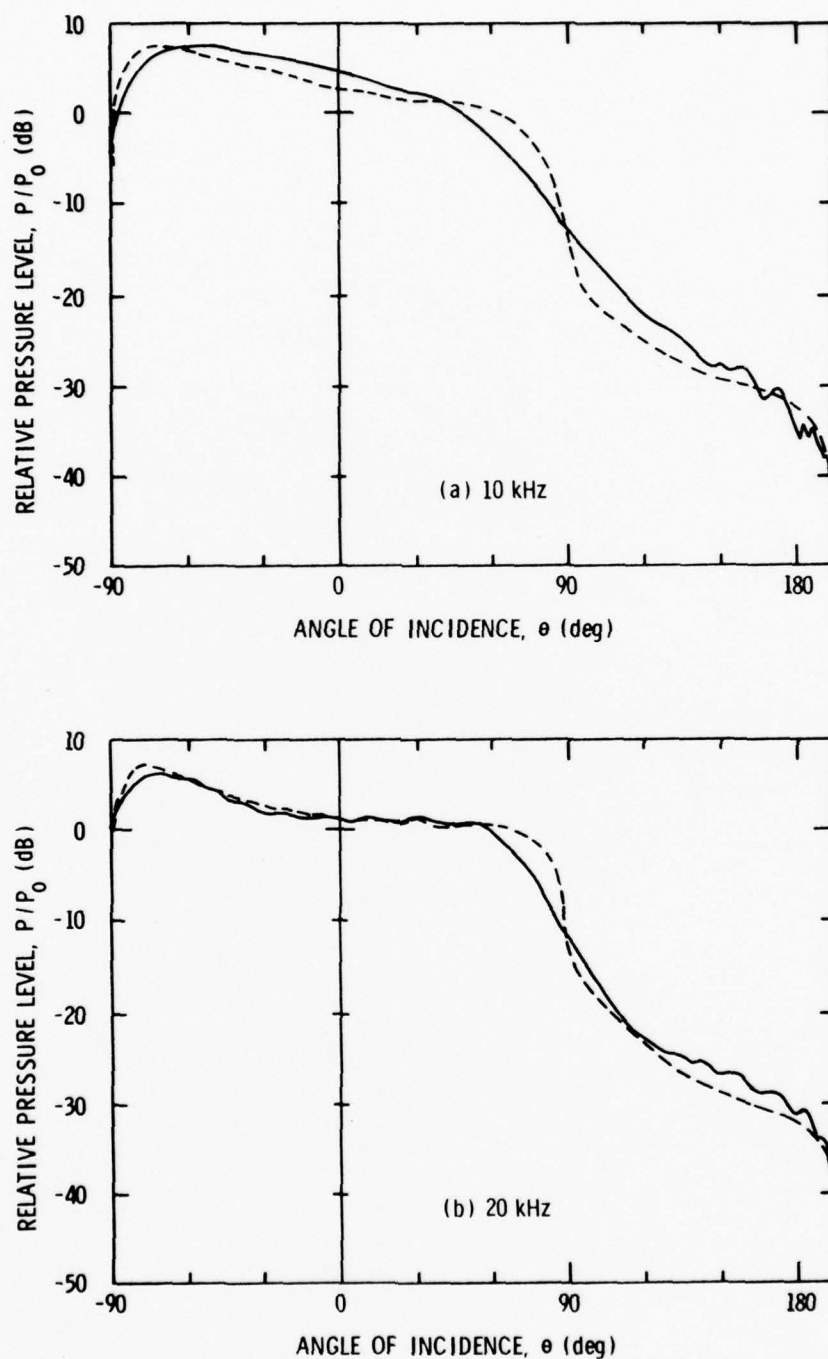


Figure 5.2 Directivity Patterns at 10 kHz and 20 kHz of a Transducer on the Surface of a Sharp 75° Wedge. Experimental (solid line) and Theoretical (dashed line) are compared.

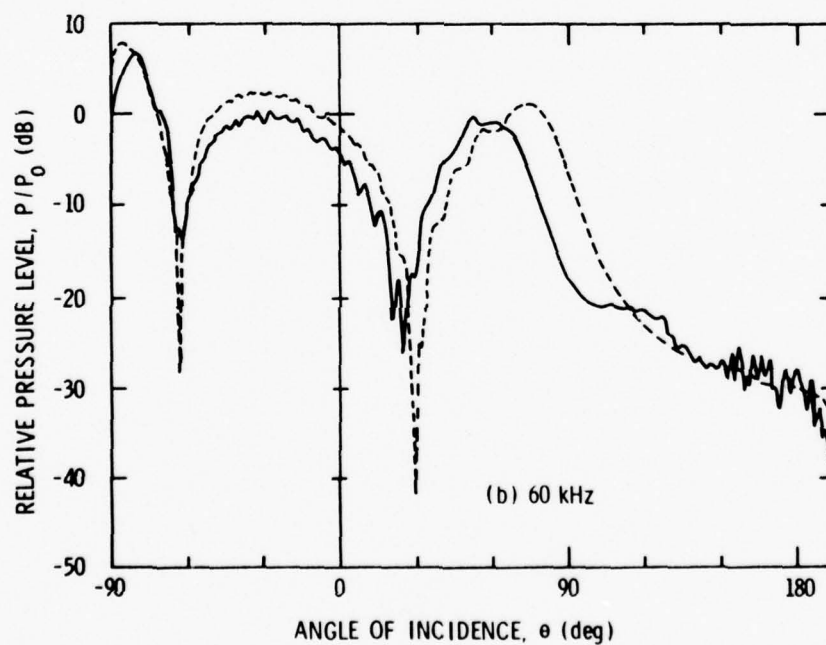
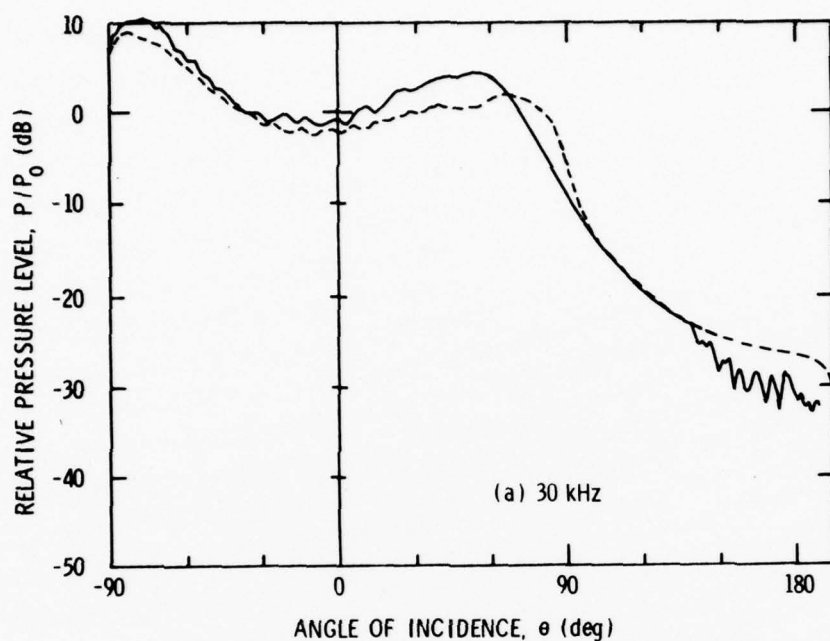


Figure 5.3 Directivity Patterns at 30 kHz and 60 kHz of a Transducer on the Surface of a Sharp  $75^\circ$  Wedge. Experimental (solid line) and Theoretical (dashed line) are Compared.

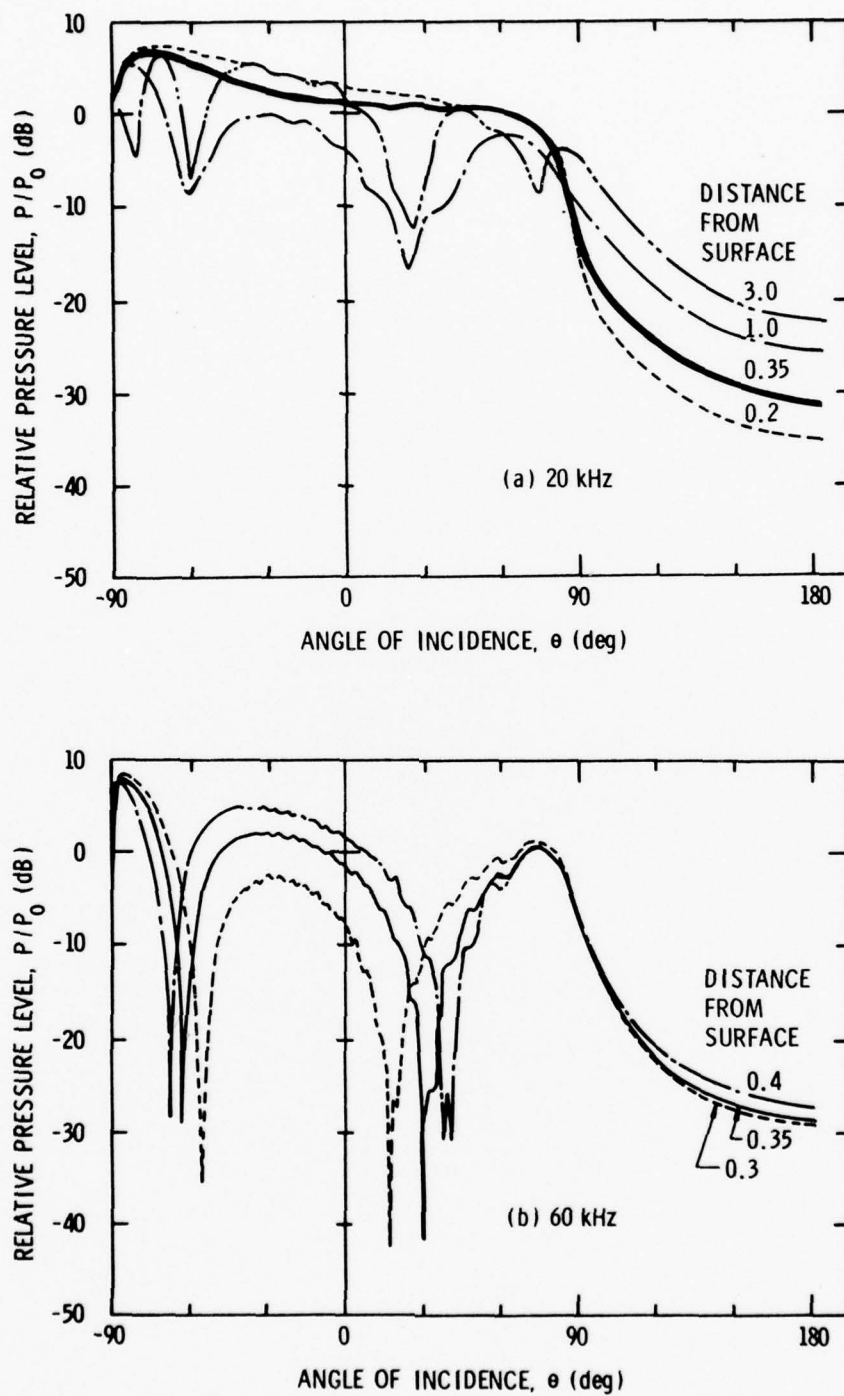


Figure 5.4 Calculated Directivity Pattern Variation for Different Source to Surface Distances.

closer together are the large dips, also, the center lobe and the shadow area are lower in level.

#### 5.3.2 Sharp Edge with Scattering Strip

A soft  $1/4'' \times 1/2''$  scattering strip was placed on the top surface immediately adjacent to the  $75^\circ$  wedge as is illustrated in Figure 3.3. Directivity patterns were then measured in order to verify whether the presence of the soft impedance strip changed the diffraction characteristics of the wedge. A comparison of directivity patterns of the  $75^\circ$  wedge with and without the soft scattering bar is shown in Figures 5.5 and 5.6.

It is readily apparent that when the soft scattering bar was added to the edge, the level in the shadow region was reduced by 5 to 10 dB. The effect has thus been to increase the effective angle of the wedge and to introduce a softer impedance at the edge, both of which would tend to lower the diffracted field level in the shadow region. In the insonified region, the ripple effect is more evident with the scattering bar present. A larger ripple effect would indicate either the diffracted field is higher or that some form of scattering or reflection is adding to the diffracted field. The latter explanation is most likely the cause since it would be expected that the diffracted field in the insonified region would decrease when it decreases in the shadow region.

#### 5.4 Directivity Patterns for a Wedge of Finite Curvature

A wedge with a radius of curvature of 6", shown in Figure 3.1(b), was used to obtain the directivity patterns which are given in Figures 5.7 and 5.8. The patterns for the smooth curved surface, i.e., no



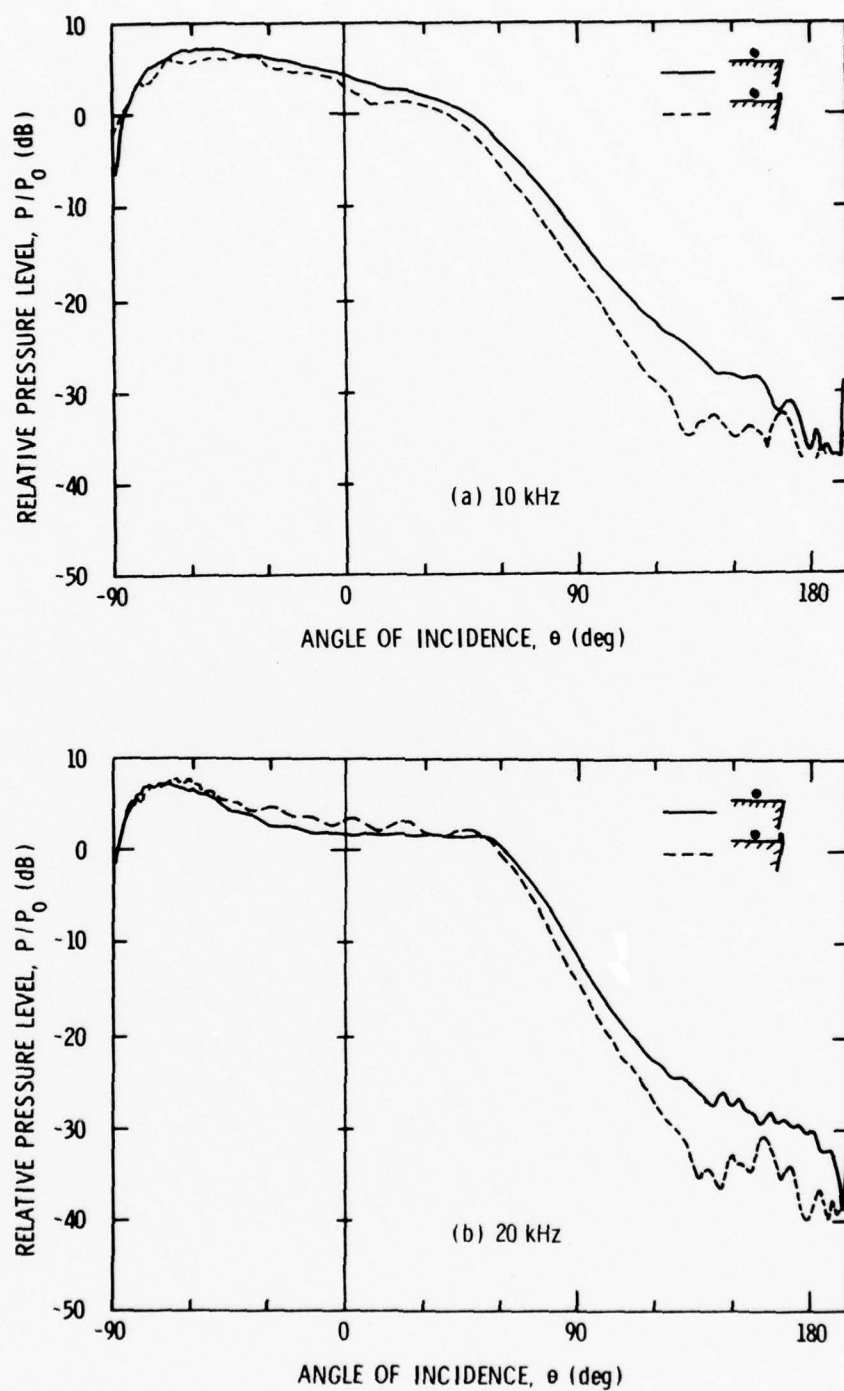


Figure 5.5 Comparison of Measured Directivity Patterns at 10 kHz and 20 kHz for a Sharp  $75^\circ$  Wedge With a Scattering Bar (dashed line) and Without a Scattering Bar (solid line).

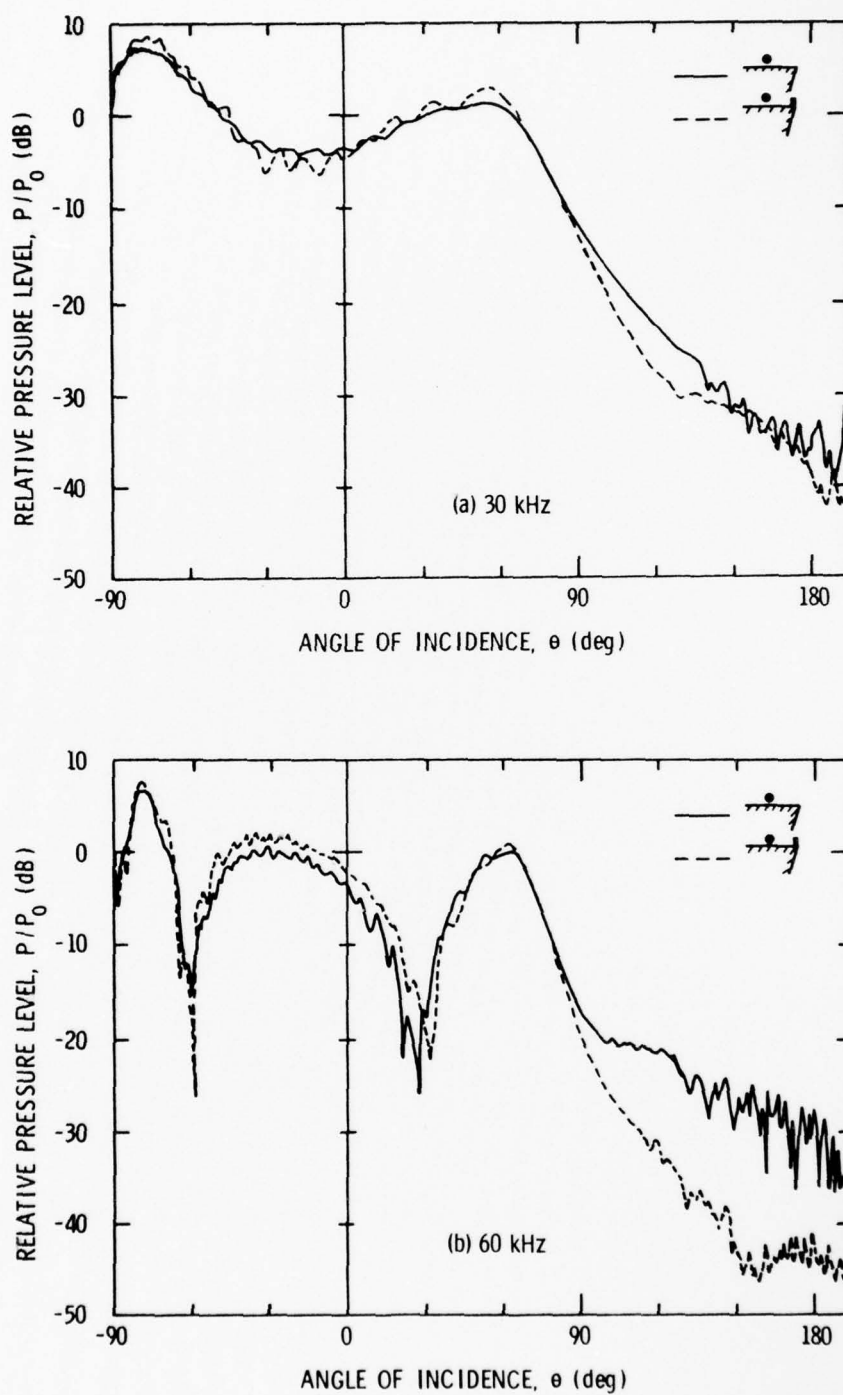


Figure 5.6 Comparison of Measured Directivity Patterns at 30 kHz and 60 kHz for a Sharp  $75^\circ$  Wedge With a Scattering Bar (dashed line) and Without a Scattering Bar (solid line).

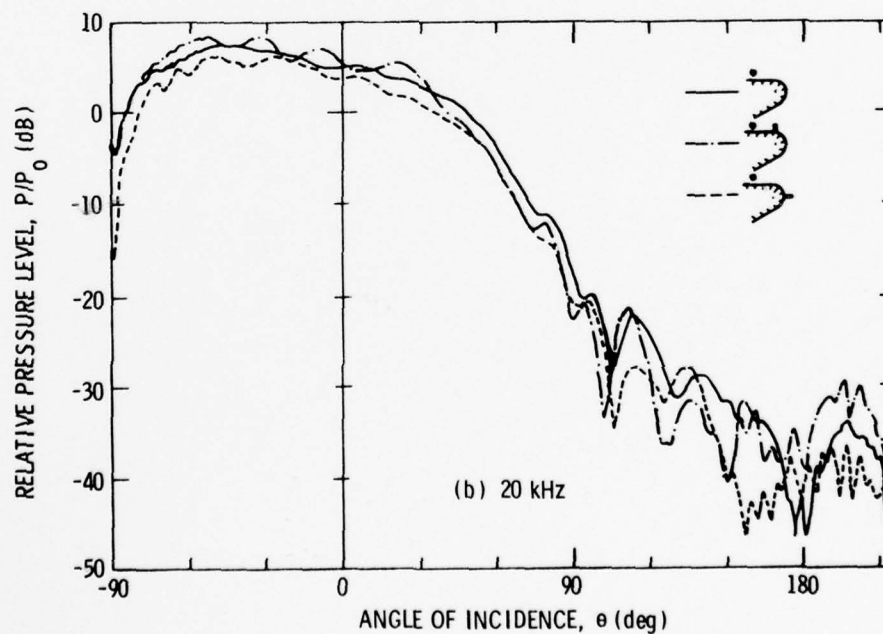
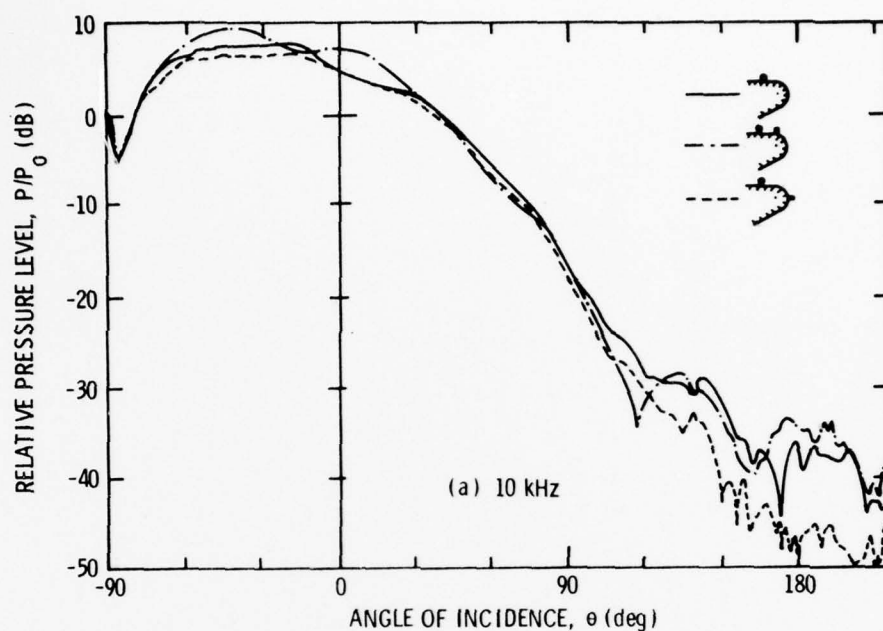


Figure 5.7 Comparison of Measured Directivity Patterns at 10 kHz and 20 kHz for a 30° Cylindrical Wedge of 6" Radius With and Without Scattering Bars.

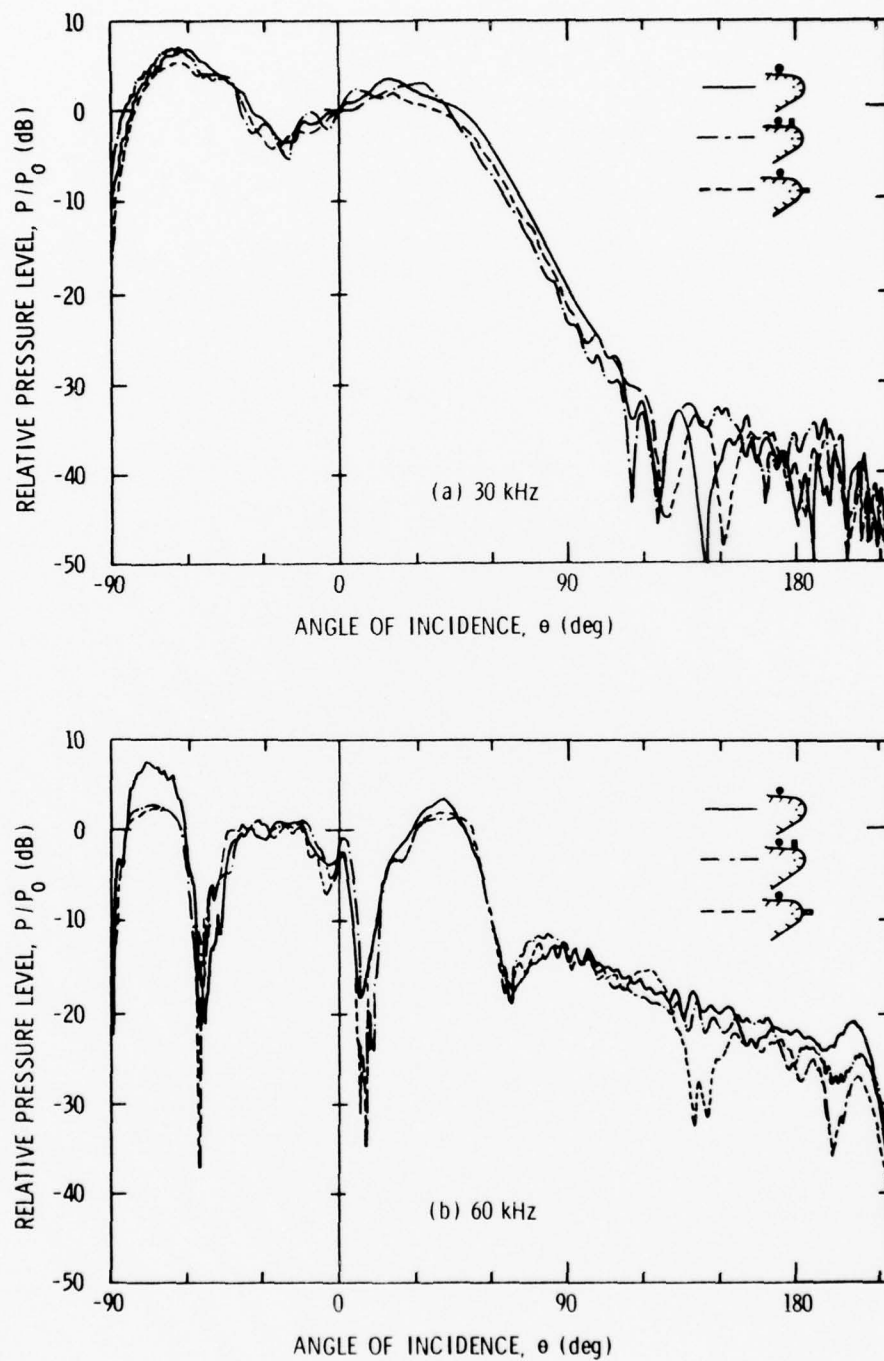


Figure 5.8 Comparison of Measured Directivity Patterns at 30 kHz and 60 kHz for a  $30^\circ$  Cylindrical Wedge of 6" Radius With and Without Scattering Bars.

scattering bar, are represented by solid lines. The broken lines represent the directivity patterns when a soft bar (Section 3.4) is placed at the point where the plane is tangent to the curved edge or at a point  $90^\circ$  along the curved surface from the tangent point.

It is apparent that positioning a soft scattering bar at the tangent point of the plane and the curved surface has little or no effect on the directivity patterns at any of the four frequencies recorded. Placing the scattering bar  $90^\circ$  along the curved surface produces an interesting effect. At the higher frequencies (30 kHz and 60 kHz), virtually no significant difference in the directivity patterns can be observed. A lower diffracted field level, however, is evident in the shadow region at 20 kHz and even more evident at 10 kHz. An assumption normally applied to curved surfaces is that, on the basis of Keller's theory, an edge can be treated as a curved surface whenever its radius of curvature is comparable with or greater than the wavelength. Here, the wavelength at 10 kHz is equal to the radius of curvature of the edge. The level in the shadow region of the directivity pattern obtained at 10 kHz is reduced to 5 to 10 dB when the soft bar is positioned  $90^\circ$  along the curved surface and is of the same order of decrease as occurred with the sharp edge. As the wavelength decreases, i.e., frequency increases, the effect of the soft bar on the directivity patterns disappears, leading to the conclusion that the radius of curvature should be greater than a wavelength before a curved surface analysis can be applied and high edge attenuation can be expected.

## CHAPTER VI

### FINITE BAFFLE EXPERIMENTAL RESULTS

#### 6.1 Introduction

A brief examination of a few directivity patterns will serve as an introduction to the experimental results and should provide some insight into the general pattern characteristics of a transducer mounted on finite baffles of various geometries and different impedances. Figure 6.1 is a composite curve of the directivity patterns of a transducer mounted in the center of each of the eight baffle configurations described in Table 3.1. The patterns were measured at the mid-test frequency, 20 kHz, and have been smoothed in the diffraction lobe region by plotting a locus of the diffraction lobe peaks.

The most striking pattern characteristics are the distinct differences between the patterns of a transducer on a rigid surface compared to those on a soft surface. Patterns measured with each of the rigid test surfaces, Cases IA, IIA, IIIA, and IVA in Table 3.1, show an oscillatory response or ripple for angles of incidence within  $\pm 60^\circ$  of the normal. Effects such as these have been predicted in Figures 2.16 and 2.18 which were calculated via the single-edge diffraction model and, from Figure 2.22, via the multi-edge mode. Interference phenomenon causing a ripple effect is characteristic of the central pattern lobe for each of the three baffles involving rigid test surfaces (see Section 3.3.2). Six maxima and five minima are present at approximately  $\pm 10^\circ$ ,



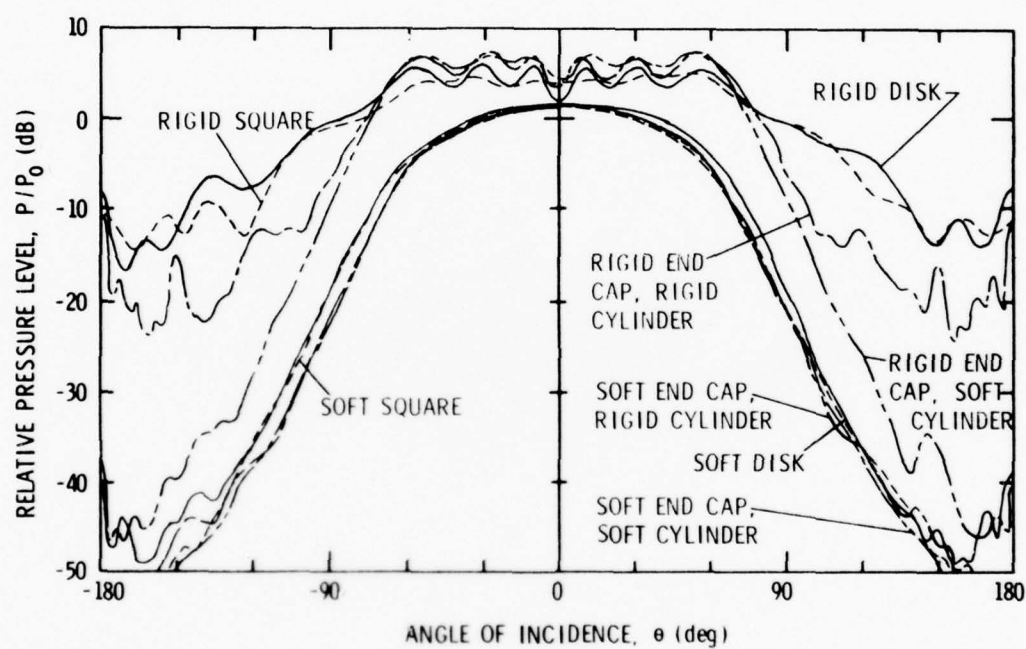


Figure 6.1 Measured Directivity Patterns for a Center Mounted Probe on Different Baffles at 20 kHz.

$\pm 30^\circ$ ,  $\pm 56^\circ$ , and  $0^\circ$ ,  $\pm 20^\circ$ ,  $\pm 42^\circ$ , respectively, showing good agreement with Figure 2.22 and verifying that the diffraction theory agrees with the experimental results. A simple means is available for predicting the angles at which pressure maxima and minima occur via the basic assumption of diffraction theory that an edge can be treated as a point where the incident field is reradiated with a phase shift of  $180^\circ$ . The maxima and minima can therefore be obtained from the equation,

$$\begin{aligned} \text{maxima} \quad d \sin \theta &= (2n + 1) \lambda / 2 , \\ \text{minima} \quad d \sin \theta &= n \lambda , \end{aligned} \quad (6.1)$$

where  $n = 0, 1, 2 \dots$ . Using this simplified approach the predicted maxima occur at  $\pm 9.6^\circ$ ,  $\pm 30.0^\circ$ ,  $\pm 56.4^\circ$  and the minima at  $0^\circ$ ,  $\pm 19.5^\circ$ ,  $\pm 41.8^\circ$ . Excellent agreement between these calculated angles and the corresponding experimentally measured angles are evident. The "bright spot" expected at  $180^\circ$  is present in each of the rigid baffle patterns.

The rigid square surface does not show a strong oscillatory response due to the lack of axial symmetry. Both the rigid disk and square baffles, however, produce a -3 dB beamwidth which is approximately  $140^\circ$ . Beyond these -3 dB angles, the patterns appear similar, having a response level which decreases by about 15 dB at an incident angle of about  $\pm 130^\circ$ . The close matching of the patterns is not unexpected since the diameter of the disk has the same dimension as the side of the square. The addition of a finite, rigid cylinder behind the rigid disk results in a pattern which has the same characteristic ripple pattern in the insonified region but has diffraction lobes which are 8 dB lower in the shadow region.

In contrast, experimental data from soft test surfaces show a smooth bell-shaped pattern with -3 dB points at approximately  $\pm 45^\circ$ . The diffraction lobes in the shadow region are between 45 and 50 dB below the peak, the major lobe being very similar in shape for each of the soft baffles. Again, the "bright spot" is observed, except for the soft square and the soft end-cap, soft cylinder baffles. The diffraction lobe level of -46 dB for the pattern from the soft disk was slightly higher than that for the soft square and soft end-capped cylinders.

A transducer on the rigid end-cap, soft cylinder has a pattern response which mixes the pattern characteristics obtained on rigid and soft baffles. At incident angles of less than  $\pm 60^\circ$ , the familiar ripple interference phenomenon of patterns from a rigid disk is observed, however, at larger angles, the response acts similar to that of a soft baffle and has a diffraction lobe level 48 dB below its average peak level. It is of interest to note that the relative peak to diffraction lobe level of this rigid end-cap, soft cylinder baffle is essentially the same as that of the soft baffles.

The impedance of the baffle edge, or cylindrical side, therefore, plays a significant role in the level of the diffraction lobes, whereas the impedance of the baffle-face plays the most significant role in the pattern beamwidth. It is very important to incorporate impedance, hence, element directivity pattern information, into underwater transducer array or baffle design since it helps to specify which area of the baffle needs design attention in order to achieve the desired directivity pattern.

The experimental data obtained at 15 kHz are presented in Figure 6.2(a). These patterns are well behaved and give essentially the same

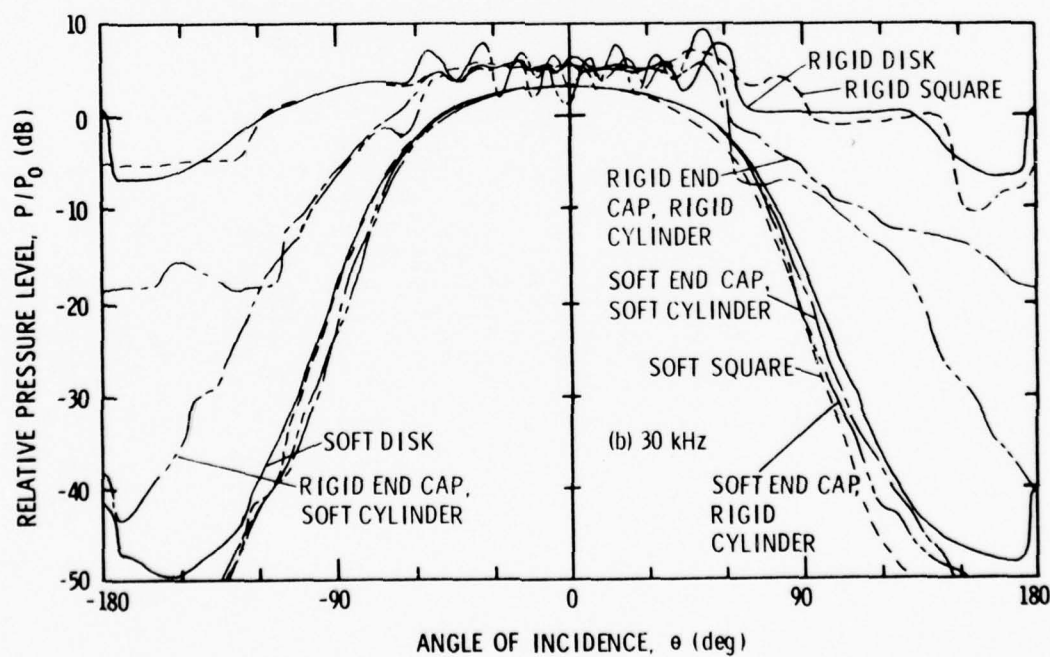
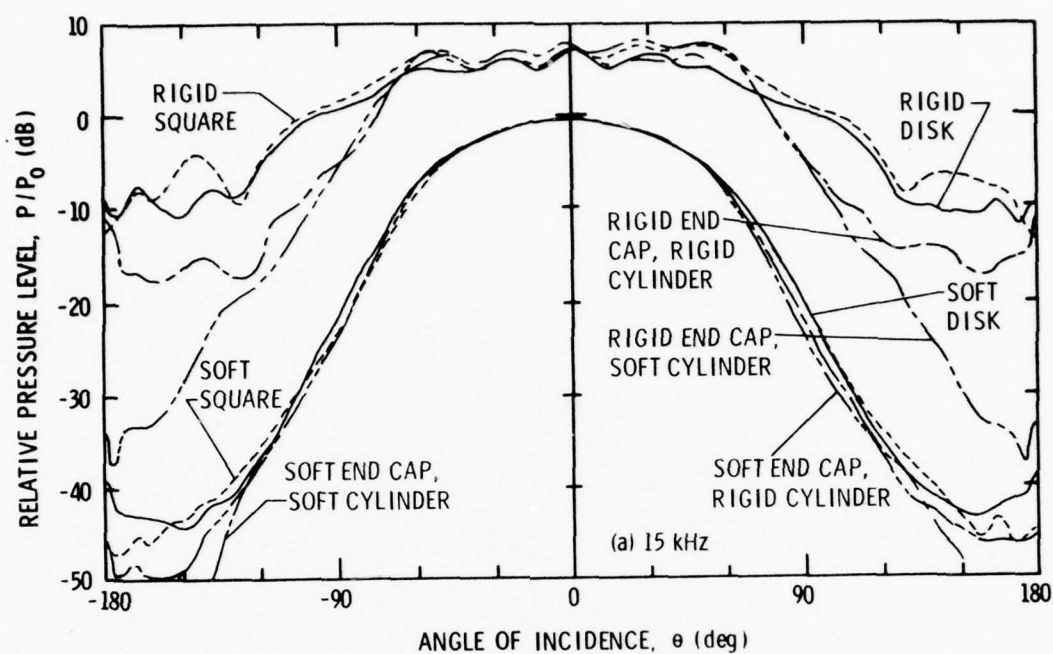


Figure 6.2 Measured Directivity Patterns for a Center Mounted Probe on Different Baffles at 15 kHz and 30 kHz.

relative information as did the patterns taken at 20 kHz. The interference phenomena seen on the rigid baffles at angles of incidence smaller than  $\pm 70^\circ$  produce five maxima compared to the six maxima of 20 kHz. The experimental maxima and minima occur at angles of  $0^\circ$ ,  $\pm 27^\circ$ ,  $\pm 54^\circ$ , and  $\pm 14^\circ$ ,  $\pm 40^\circ$ , respectively.

At 30 kHz, Figure 6.2(b), there is evidence of more variation in data than was present at either of the other two frequencies. Using data from the rigid disk, the maxima and minima of the ripple occur near  $0^\circ$ ,  $\pm 12^\circ$ ,  $\pm 27^\circ$ ,  $\pm 54^\circ$  and  $\pm 6^\circ$ ,  $\pm 20^\circ$ ,  $\pm 43^\circ$ ,  $\pm 65^\circ$ , respectively. These patterns are also very similar to those obtained at 20 kHz except the rigid baffles have a smaller beamwidth and the soft baffles have lower diffraction lobe levels.

A summary of the diffraction lobe levels and beamwidths of the centrally positioned transducer for all eight baffles can be found in Table 6.1. It can be seen that the -3 dB beamwidths obtained on a rigid baffle are between  $107^\circ$  and  $145^\circ$ , whereas the soft surfaces produce more consistent and narrower pattern beamwidths of  $85^\circ$  to  $96^\circ$ . These facts imply that if a wide beam pattern is desired, a rigid baffle should be used. Alternatively, if a narrow beam with low response to the sides is desired, a soft baffle should be used instead.

Diffraction lobe levels of patterns obtained with soft surfaces are more than 20 dB lower than those with rigid surfaces. When a rigid end-cap is placed on a soft cylinder, a broad pattern characteristic of a rigid surface, and a low diffraction lobe level characteristic of a soft surface, is produced. This baffle is of interest since it indicates that low diffraction lobes can be obtained when the diffracting edge is a soft material even if the hydrophone is mounted on a rigid surface.



TABLE 6.1

DIFFRACTION LOBE LEVEL AND BEAMWIDTH FOR A  
HYDROPHONE CENTRALLY POSITIONED ON THE BAFFLE

<u>Baffle</u>	<u>-3 dB Beamwidth (degrees)</u>			<u>Diffraction Lobe Level (dB)</u>		
	<u>15 kHz</u>	<u>20 kHz</u>	<u>30 kHz</u>	<u>15 kHz</u>	<u>20 kHz</u>	<u>30 kHz</u>
rigid disk	128	139	124	-15	-16	-12
rigid square	143	142	122	-16	-16	-12
rigid end-cap rigid cylinder	138	145	116	-22	-23	-20
rigid end-cap soft cylinder	136	134	107	-40	-48	-35
soft disk	96	96	96	-43	-45	-48
soft square	92	92	92	-43	-48	**
soft end-cap rigid cylinder	92	90	85	-44	-48	-54
soft end-cap soft cylinder	92	86	85	**	**	**

NOTE: \*\* indicates a diffraction lobe level below -50 dB and not measurable.



Figures 6.1 and 6.2 depict the directivity patterns for a transducer positioned at the center of a baffle. The pattern variation as the transducer is moved closer to the edge of a soft baffle is shown theoretically in Figure 2.19. Another method of presenting this information for experimental data is shown in Figure 6.3. The relative response level is plotted as a function of distance from the edge for several angles of incidence. Data from each of the four soft baffles and for each of the three frequencies are plotted. The data points varied by no more than 1 to 2 dB from the curves drawn, giving a good indication of the consistency of the measurements. This also indicates that the pattern response on a soft baffle is independent of frequency when the distance is plotted in wavelengths. Moreover, since all the data for the soft baffles when plotted on the same curve show minor variations in attenuation, it follows that the geometric shape of a soft baffle is not important as long as the dimensions are comparable. Diffraction effects for a transducer mounted on a soft baffle are significant at angles of incidence beyond  $90^\circ$  and for edge distances of less than one wavelength. The pattern response level for the soft disk is higher at all angles of incidence than for the other baffles. Data from the patterns of the four rigid surfaces are not analyzed in Figure 6.3 since the pronounced ripples and the high diffraction lobes would mask the information presented in these curves.

The previous general analysis explains much of the experimental data obtained. In the following sections some comparisons will be made of theoretical and experimental patterns and more detailed curves for each baffle will be presented.

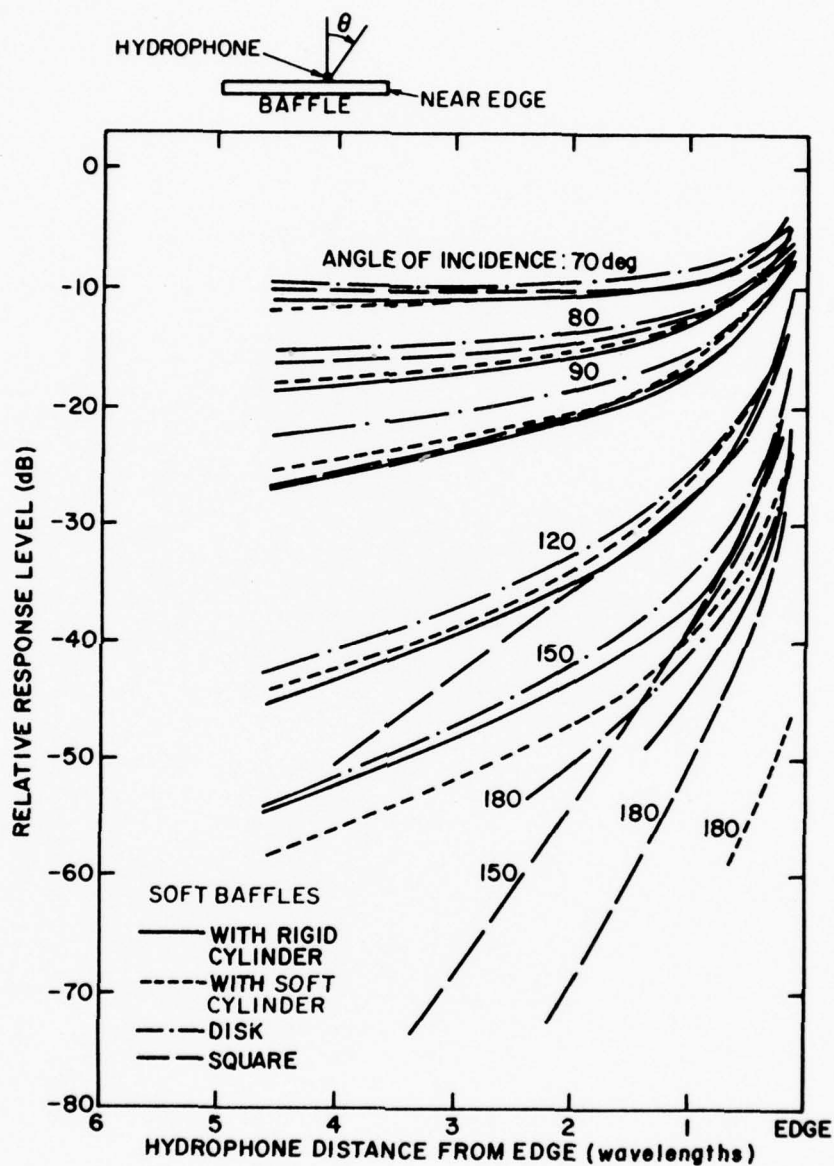


Figure 6.3 Hydrophone Responses for Soft Baffles as a Function of Position.

## 6.2 Comparison of Theoretical and Experimental Results

The following discussion will be limited to a comparison of theoretical and experimental patterns for the center frequency, 20 kHz, and to two transducer positions, viz., the baffle center and one inch from the edge. In addition, since pattern comparisons for the disk are representative of the square baffle, the latter will not be specifically considered.

Directivity patterns for the rigid disk are shown in Figure 6.4. Theoretical patterns were calculated for each of two surface impedances,  $Z_1 = Z_2 = 1000 \rho c$ , and  $26 \rho c$ , where the former impedance is equivalent to a rigid surface and the latter is the characteristic impedance of steel. Of the two, it is evident that the theoretical pattern for a rigid surface,  $Z = 1000 \rho c$ , matches the experimental pattern better. A reasonably good match between theory and experiment is observed. Soft disk directivity patterns are presented in Figure 6.5. The theoretical patterns using a surface impedance of  $Z_1 = Z_2 = 0.1 \rho c$  are an excellent match with the experimental patterns. The two-edge theoretical model cannot predict the back edge diffraction, which accounts for the mismatched diffraction field near an angle of  $-180^\circ$  in Figure 6.5(b).

Rigid end-cap, rigid cylinder directivity patterns are given in Figure 6.6. The end-cap impedance for steel is  $Z_1 = 26 \rho c$  and the aluminum cylinder impedance is  $Z_2 = 9 \rho c$ . The pattern obtained with the centrally positioned transducer is slightly asymmetric, giving a better match with theory on one side than on the other. In Figure 6.6(b), even though a good match between theory and experiment is present for angles toward the near edge,  $\theta > 0^\circ$ , it is evident that the match between

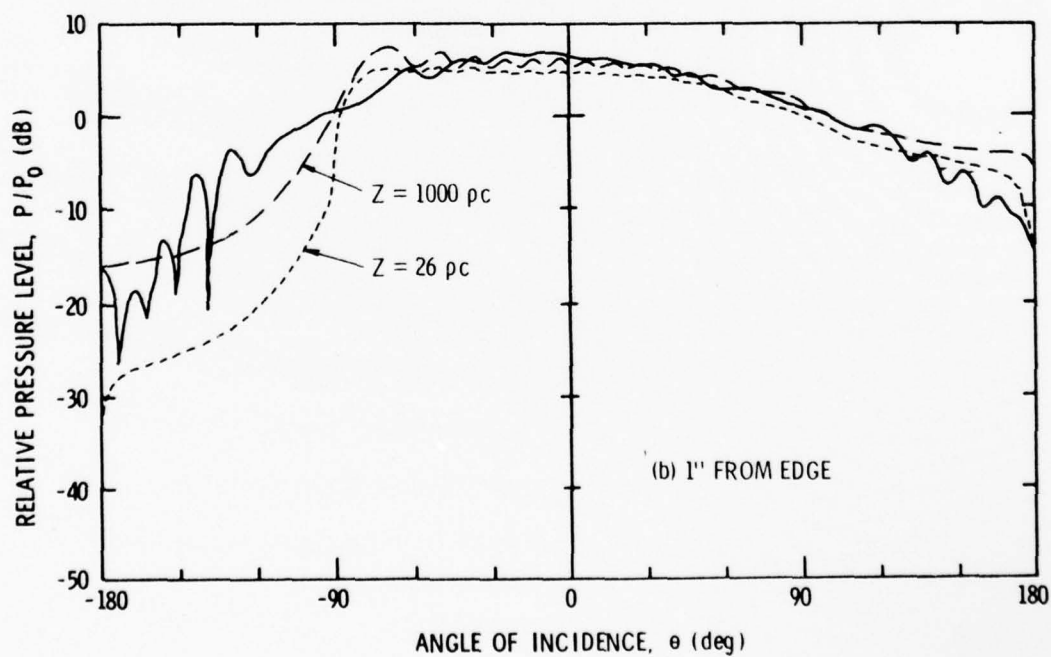
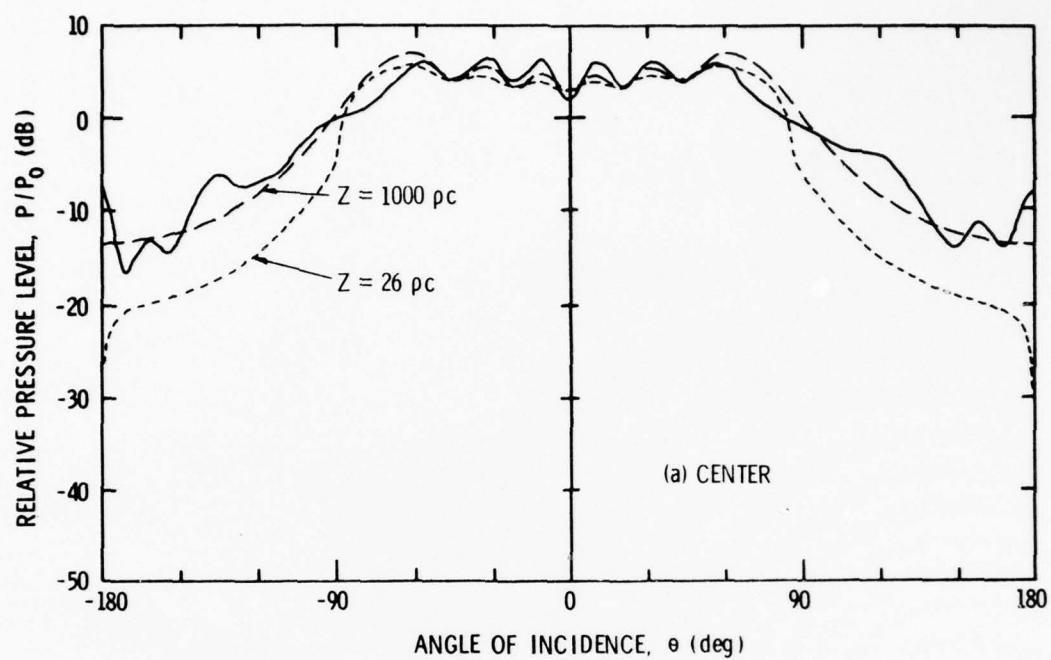


Figure 6.4 Experimental (solid line) and Theoretical (dashed line) Patterns for a Hydrophone on a Rigid Disk at 20 kHz.

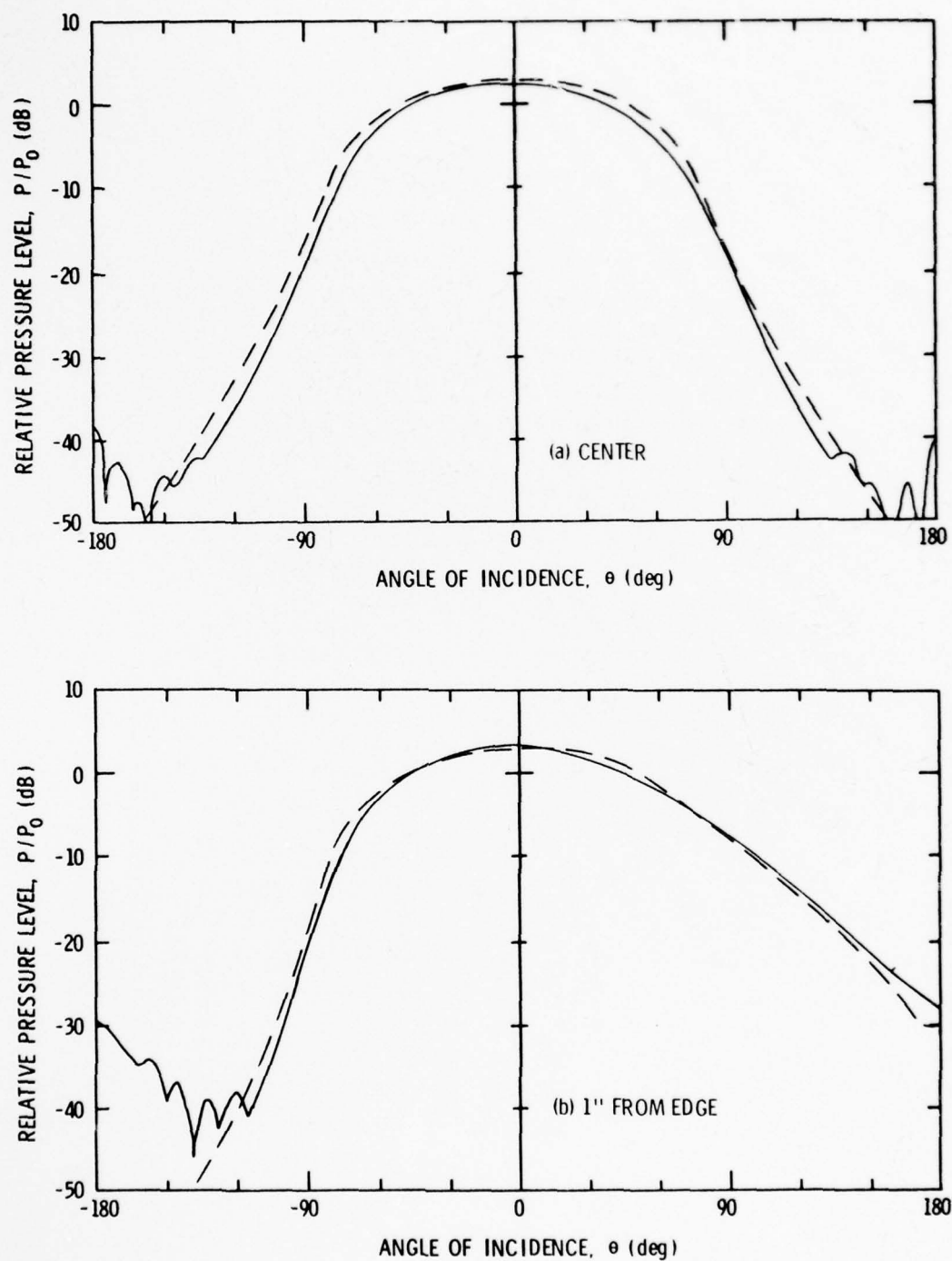


Figure 6.5 Experimental (solid line) and Theoretical (dashed line) Patterns for a Hydrophone on a Soft Disk at 20 kHz.

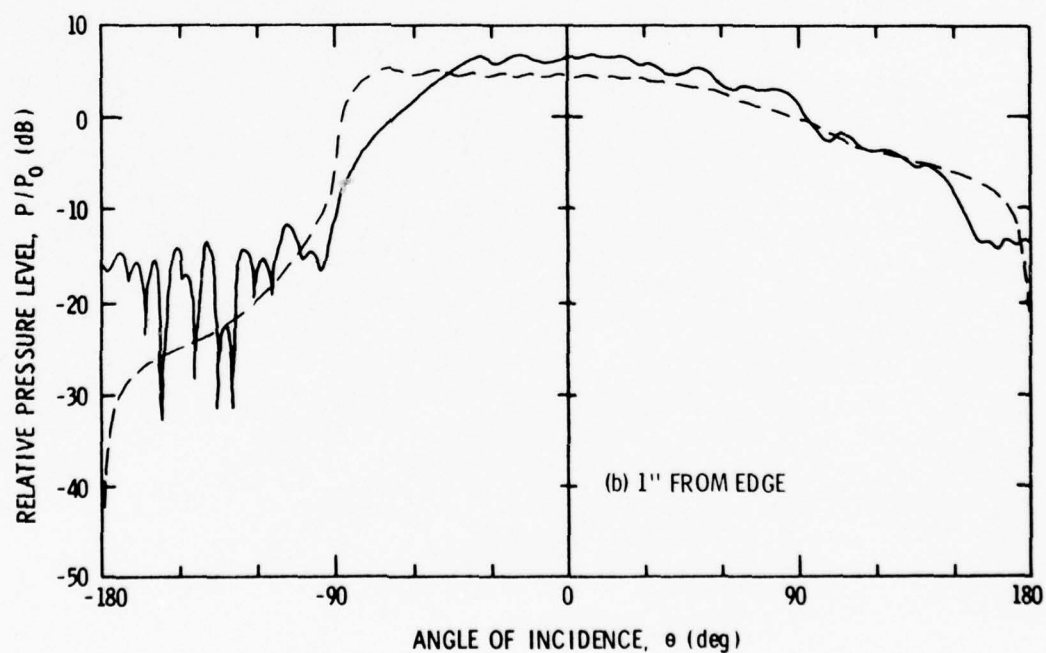
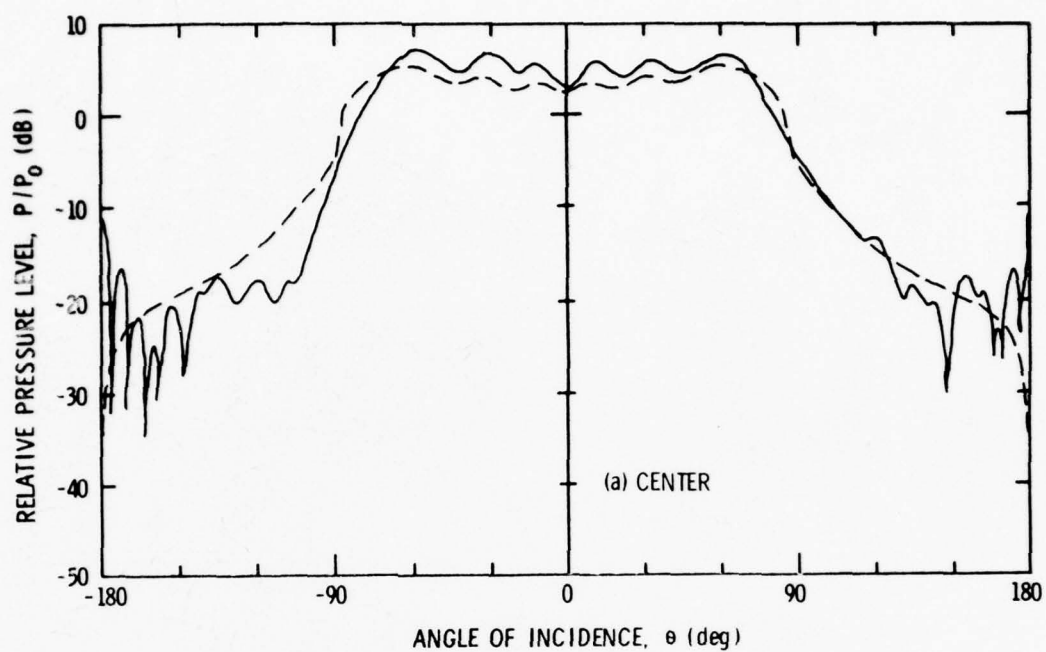


Figure 6.6 Experimental (solid line) and Theoretical (dashed line) Patterns for a Hydrophone on a Rigid End-Cap, Rigid Cylinder at 20 kHz.



theory and experiment is not good near  $\theta = -90^\circ$ . Upon reexamining Figures 6.6(a) and 6.4, the same type of mismatch is present. It appears, then, that whenever the transducer is more than a few wavelengths away from the edge, the theoretical model cannot predict diffraction levels accurately. Yet, the directivity patterns for a soft disk matched very well. The only conclusion which can be reached is that the impedance used for the surface of the rigid end-cap is inadequate. Indeed, the impedance should vary with angle of incidence, being softer for near grazing incidence. More validity for this explanation is given by overlaying the soft disk patterns onto Figure 6.6 and observing that the 'rounded edges' present in the soft disk patterns are also present in the rigid end-cap, rigid cylinder patterns.

The poor match between theory and experiment in Figure 6.7 for the rigid end-cap, soft cylinder patterns ( $Z_1 = 26 \rho c$ ,  $Z_2 = 0.1 \rho c$ ) can also be explained by the need for a more accurate description of the surface impedance. The theoretical and experimental patterns for a soft end-cap, soft cylinder, Figure 6.8, match quite well. In Figure 6.9, the results for a soft end-cap, rigid cylinder baffle again show a slight mismatch between the theoretical and experimental patterns. The theoretical model predicts directivity patterns which match the experimental patterns very well for all baffles except the rigid end-cap, soft cylinder where a better model for surface impedance as a function of incidence angle is needed.

### 6.3 Planar Baffles

#### 6.3.1 Rigid Baffles

It is difficult to obtain quantitative information from the directivity patterns of the disk and square rigid planar baffles shown

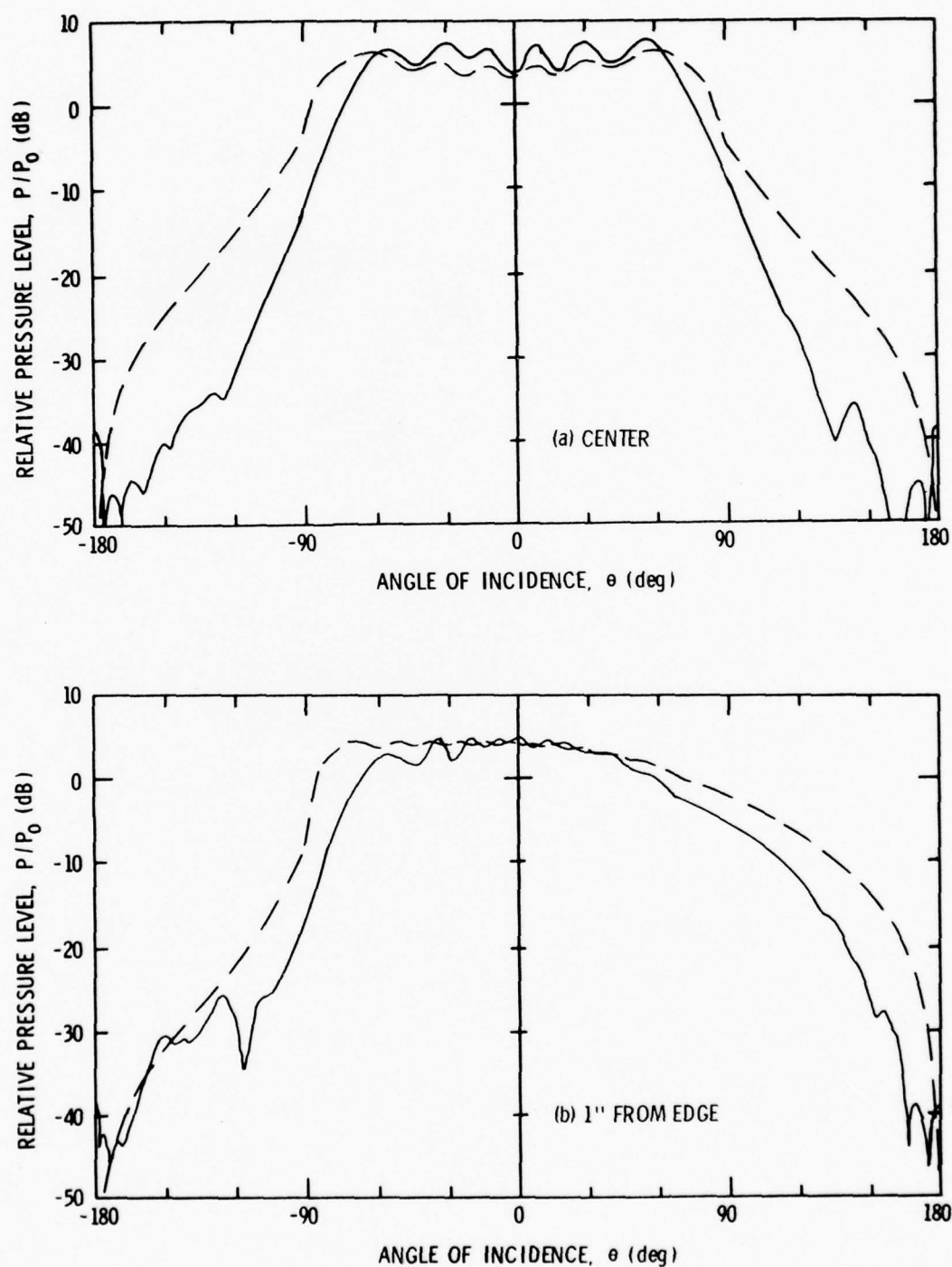


Figure 6.7 Experimental (solid line) and Theoretical (dashed line) Patterns for a Hydrophone on a Rigid End-Cap, Soft Cylinder at 20 kHz.

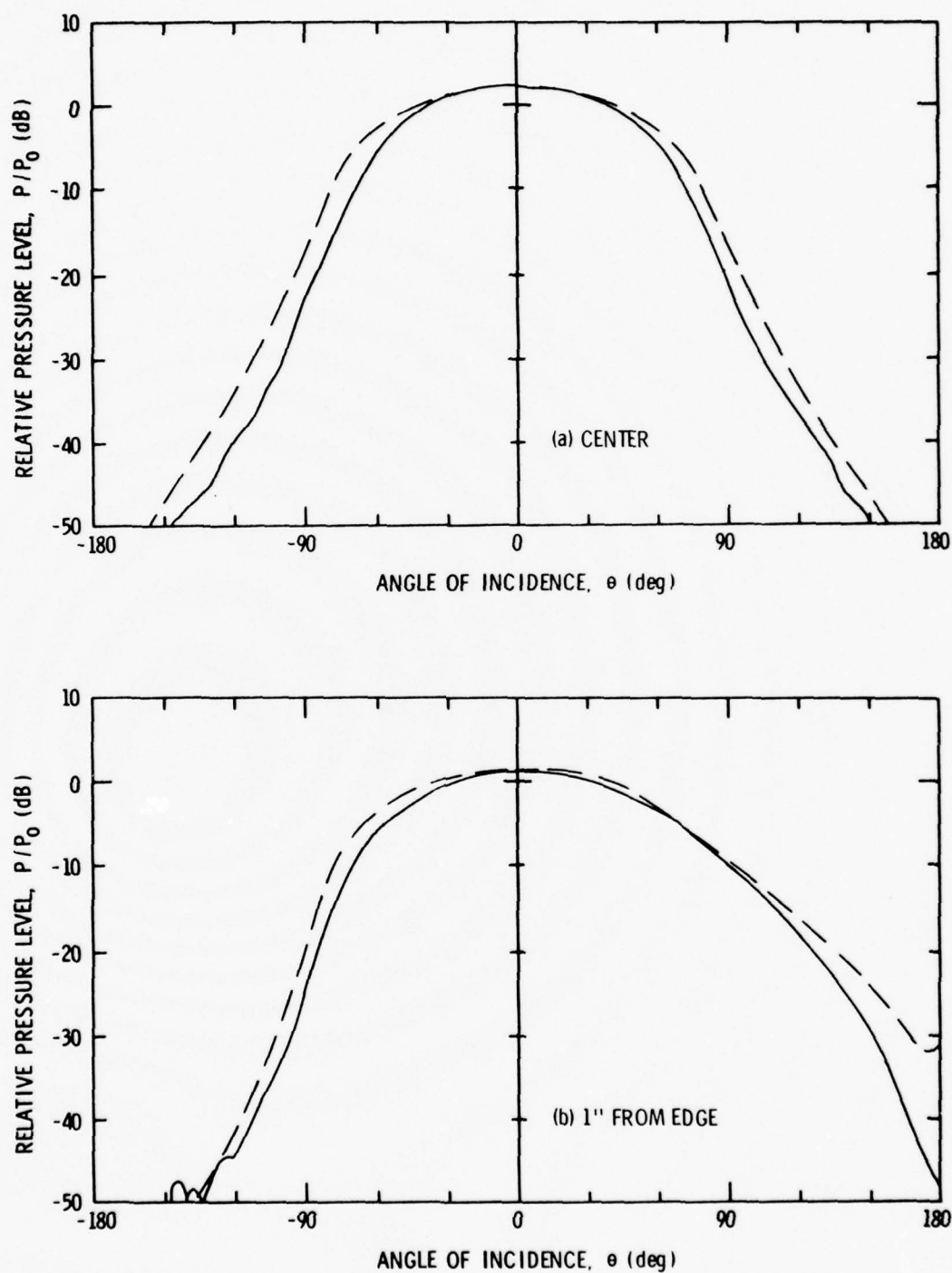


Figure 6.8 Experimental (solid line) and Theoretical (dashed line) Patterns for a Hydrophone on a Soft End-Cap, Soft Cylinder at 20 kHz.

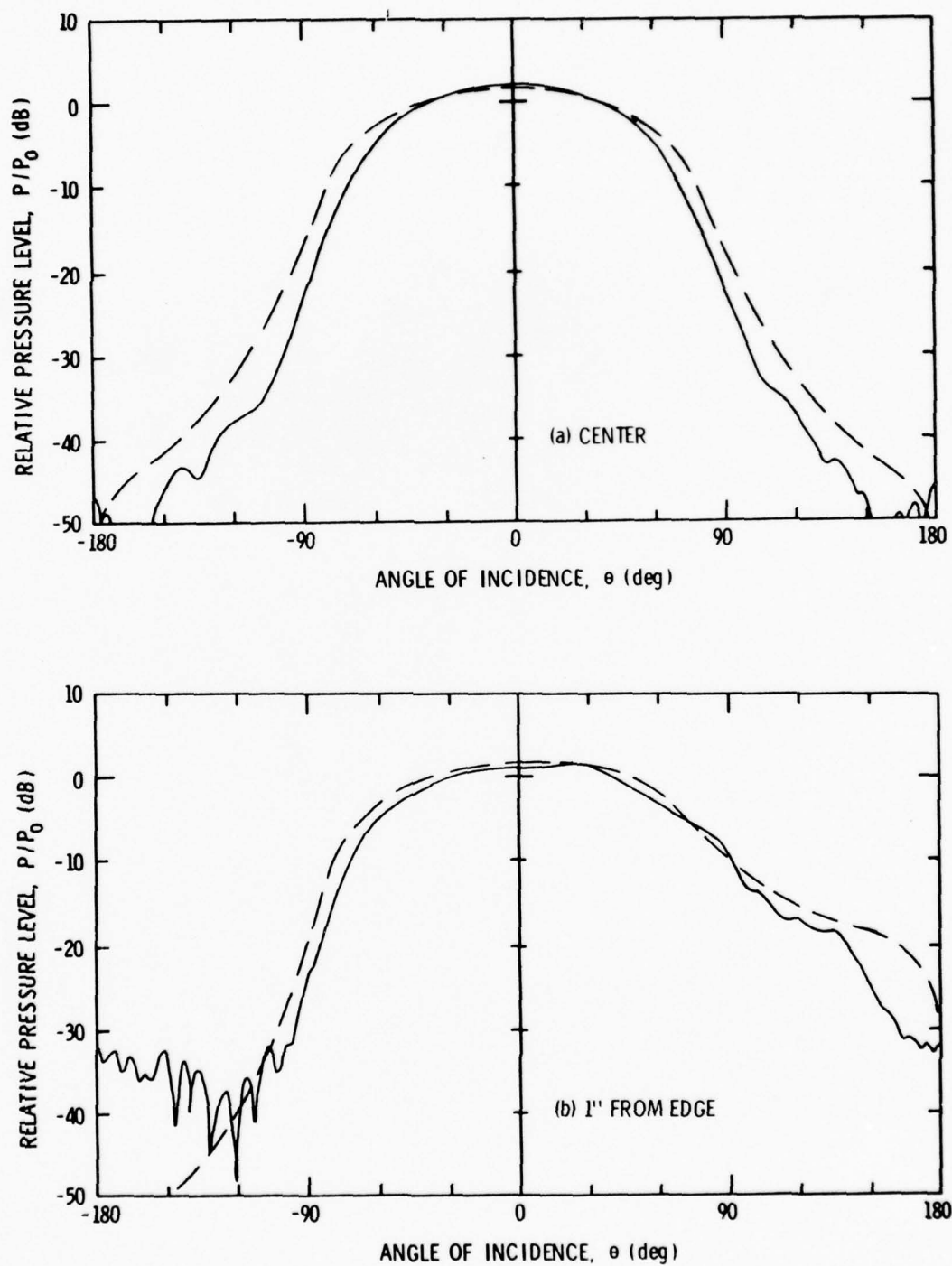


Figure 6.9 Experimental (solid line) and Theoretical (dashed line) Patterns for a Hydrophone on a Soft End-Cap, Rigid Cylinder at 20 kHz.

in Figures 6.10 through 6.12. However, qualitative and some general quantitative comparisons can be made. As the frequency increases, there is a significant increase in the number of diffraction lobes which are present, and the definition or shape of the "major lobe" becomes more pronounced. The term major lobe refers to that portion of a pattern between  $\theta = \pm 90^\circ$  and, hence, is least affected by the diffraction phenomena. At higher frequencies, the baffle is effectively larger (in terms of wavelengths) and the beamwidth of the pattern is expected to decrease. As the transducer moves toward the edge, the response level in that direction increases and the fluctuations tend to decrease. The patterns at both 15 kHz and 20 kHz for the transducer mounted on the edge and 1/2" from the edge have a noticeably higher level in the shadow region. When compared to the pattern of the centrally positioned transducer, the edge pattern is between 5 to 10 dB higher. Patterns at 30 kHz, however, do not show strong increases in shadow region levels as the probe is moved toward the edge.

The same general comments are true for the rigid square. Indeed, there is a great similarity between the two sets of data, the only basic difference being that the rigid square does not exhibit the large ripple in the insonified region as does the rigid disk. Note that the levels of the diffraction lobes at 30 kHz are higher than at the two lower frequencies. If the transmission of sound through the steel plate were dominant, the highest frequency would be expected to have the lowest diffraction lobe level, contrary to the measured results. The experimental data also show that the level of the diffraction lobes decrease from the shadow boundary to  $\theta = 180^\circ$  providing another indication that diffraction

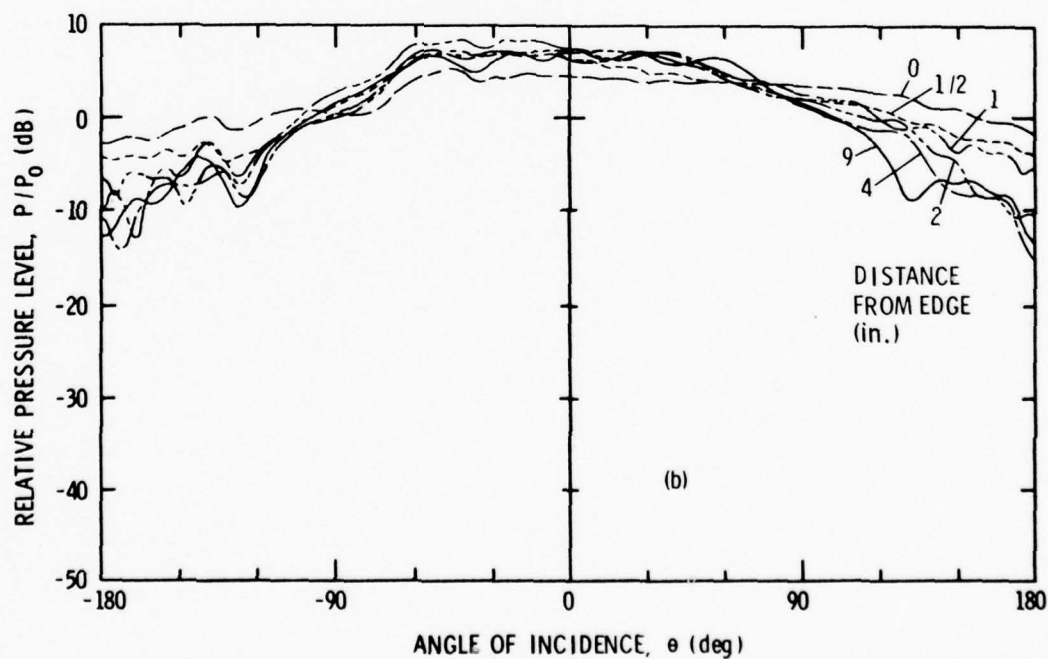
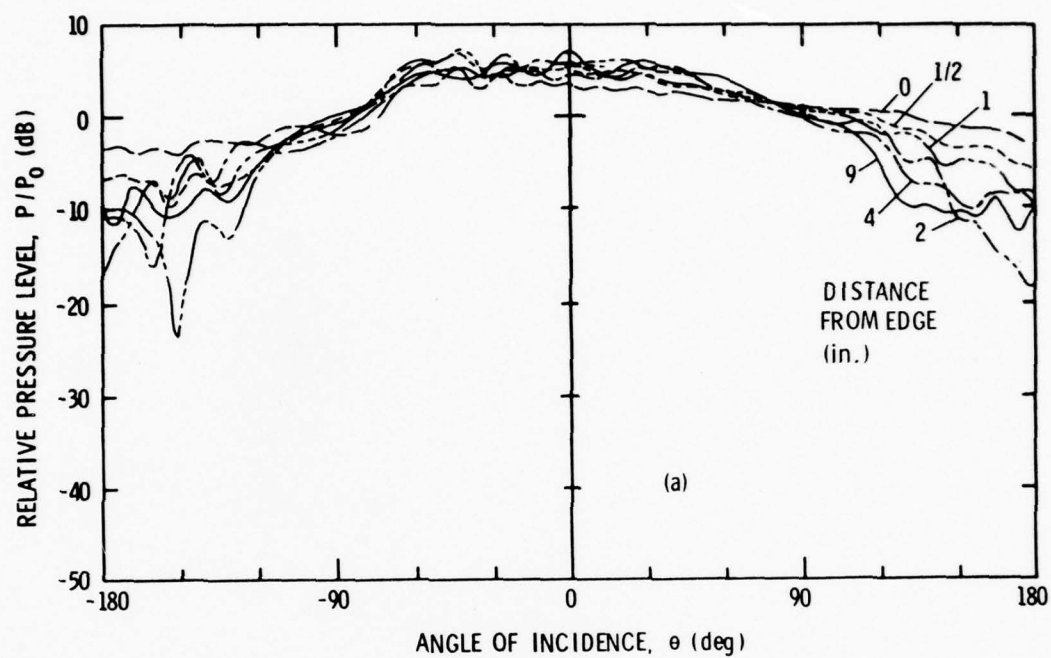


Figure 6.10 Patterns of a Hydrophone on a Rigid Disk (a) and a Rigid Square (b) at 15 kHz.



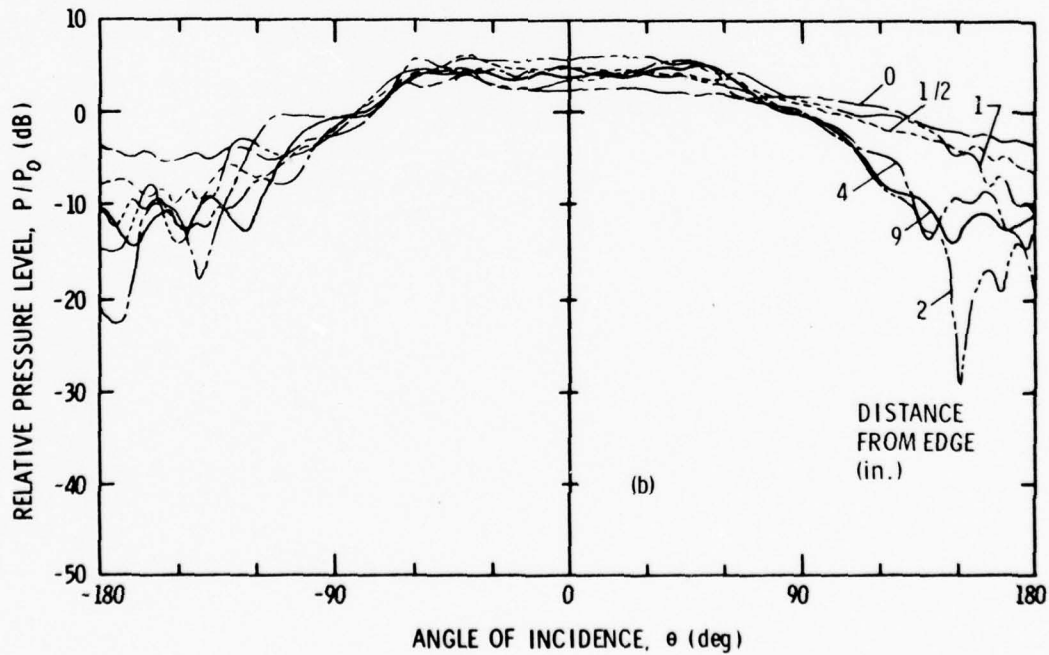
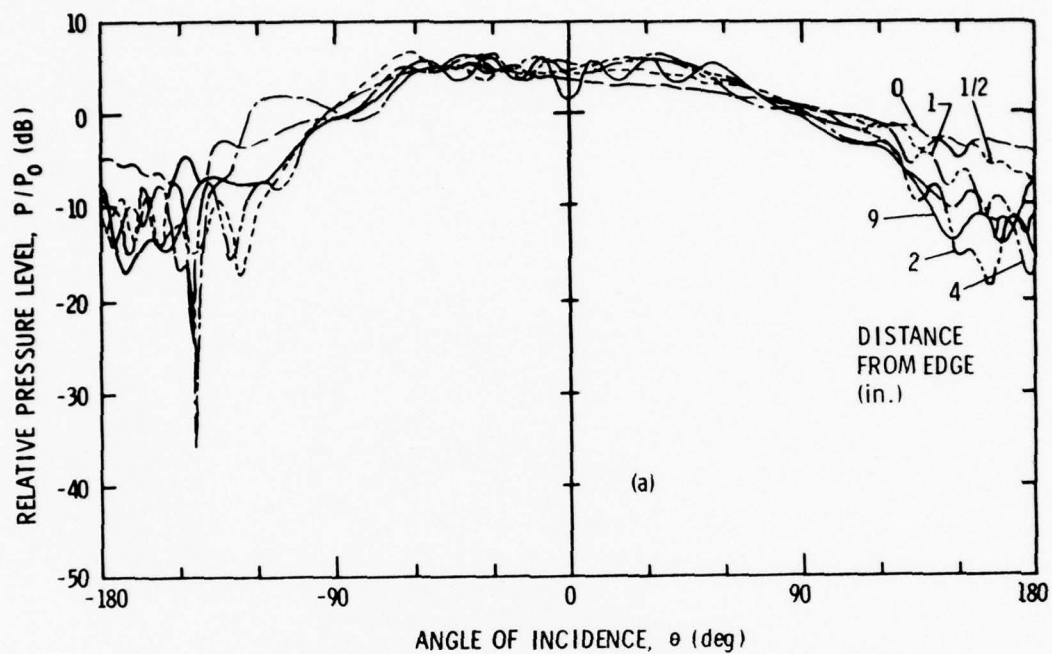


Figure 6.11 Patterns of a Hydrophone on a Rigid Disk (a) and a Rigid Square (b) at 20 kHz.

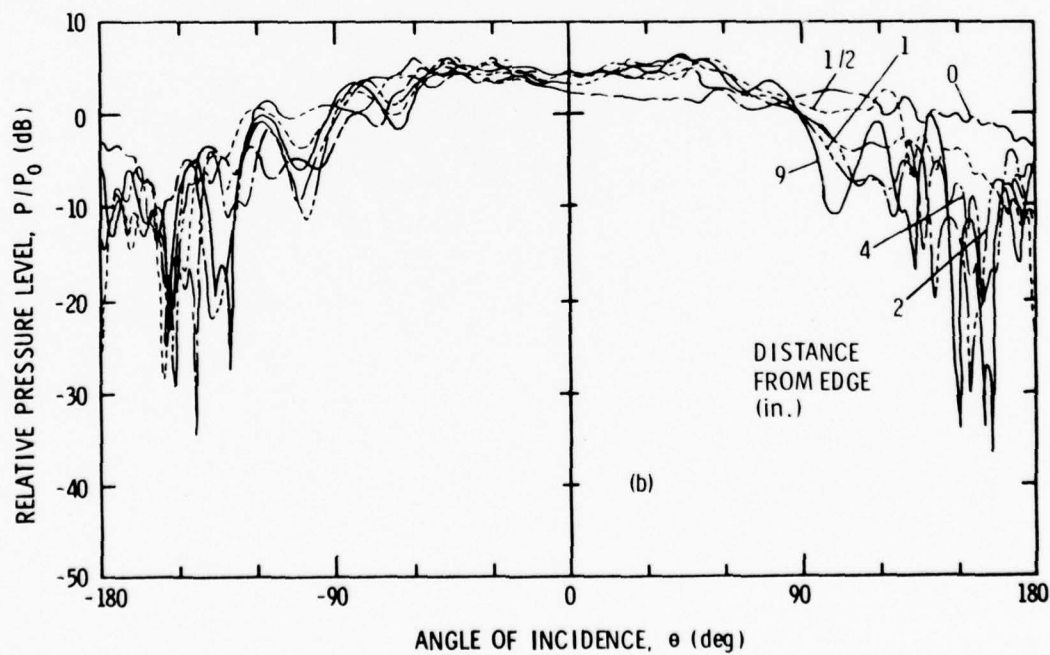
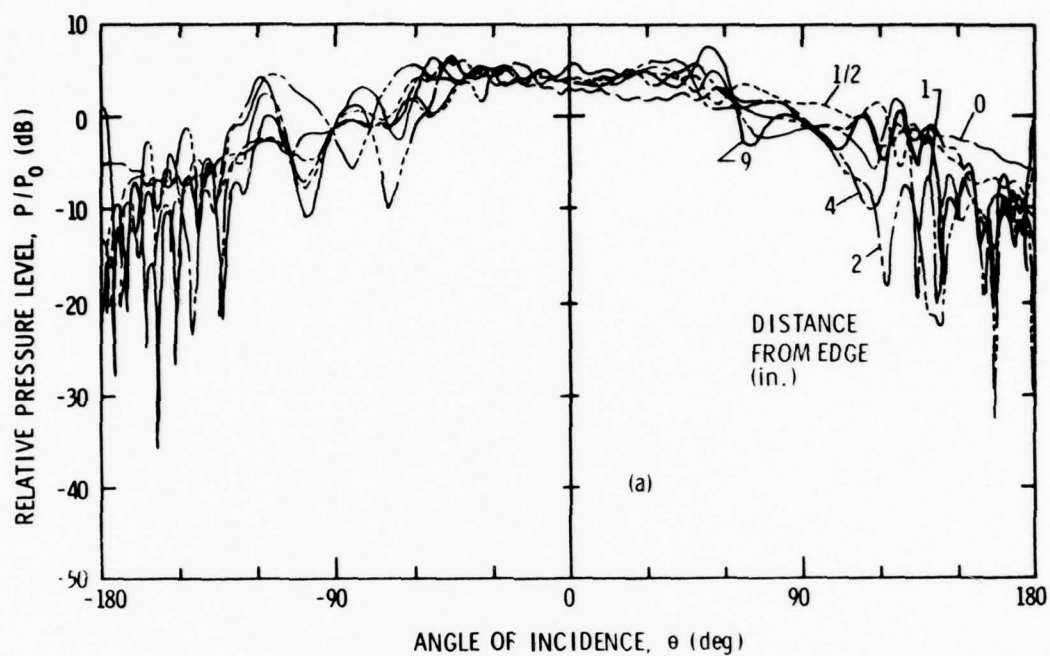


Figure 6.12 Patterns of a Hydrophone on a Rigid Disk (a) and a Rigid Square (b) at 30 kHz.

information is not being masked by transmission through the steel baffle.

### 6.3.2 Soft Baffles

Directivity patterns shown in Figures 6.13 through 6.15 for the soft disk and soft square demonstrate the changes in the patterns as a transducer is moved across a soft surface. The patterns for the soft disk were taken with a surface-mounted hydrophone, whereas the patterns for the soft square were taken with a flush-mounted hydrophone. See Section 3.3.2 for details. Note that the differences in the patterns are negligible. Changes in the patterns as the transducer is moved are much more evident on the soft baffles than on the rigid baffles because the *diffracted field* in the shadow region is reduced to a very low level. The low level of the field incident at the back surface gives the effect of a two-edge diffraction surface and allows easier analysis of the diffracted field.

It is clearly evident that as the probe is moved toward an edge, its response increases in that direction. From the experimental data, it appears that for angles in the shadow region, i.e., angles beyond  $90^\circ$  (excluding points which are diffraction lobe limited), the response level of the transducer increases approximately by equal percentages, or constant dB increments, as its distance to the edge is halved. This is generally true for each of the three frequencies tested. It is also evident that as frequency increases, the skirts of the main lobe become narrower and the level of the diffraction lobes decrease.

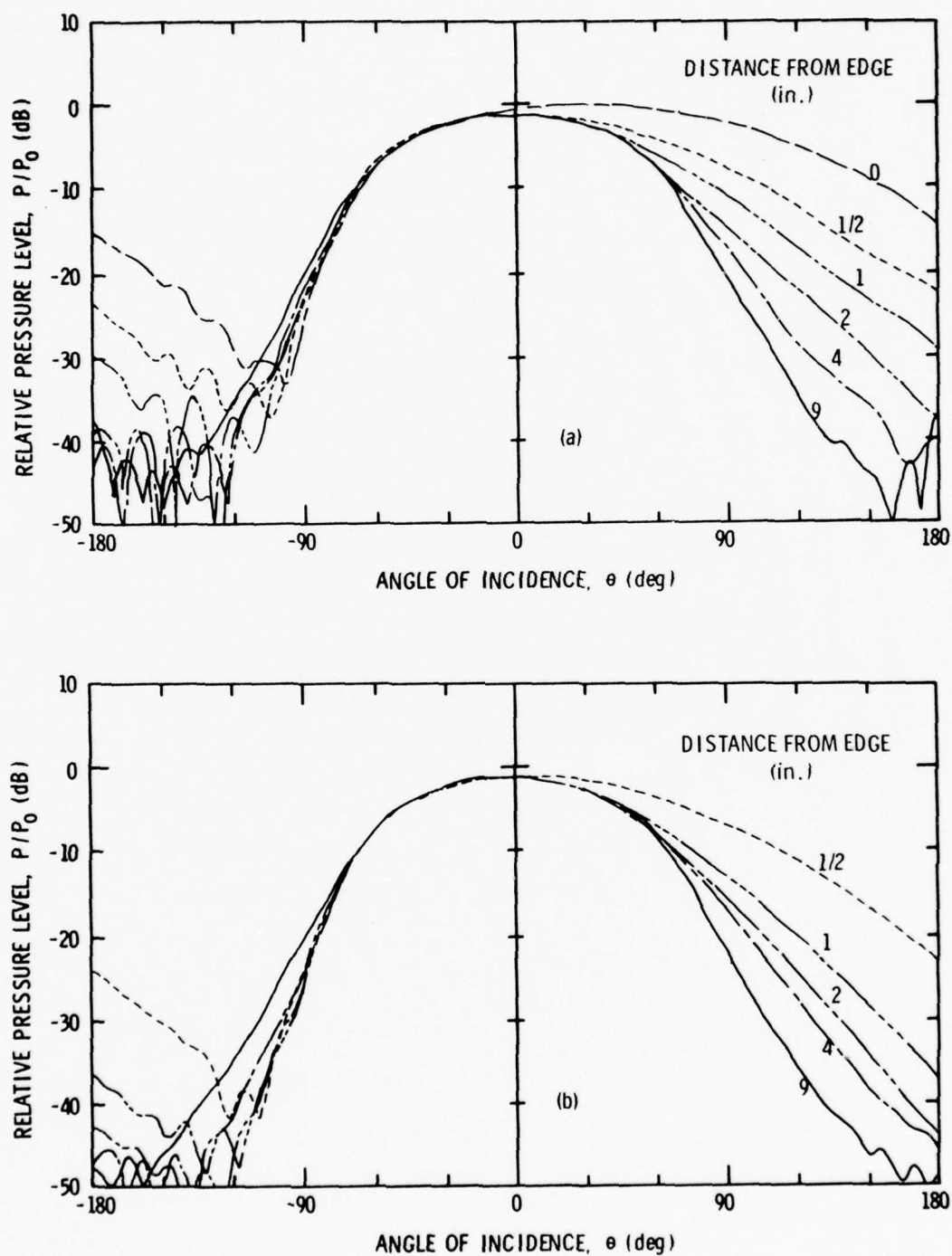


Figure 6.13 Patterns of a Hydrophone on a Soft Disk (a) and a Soft Square (b) at 15 kHz.

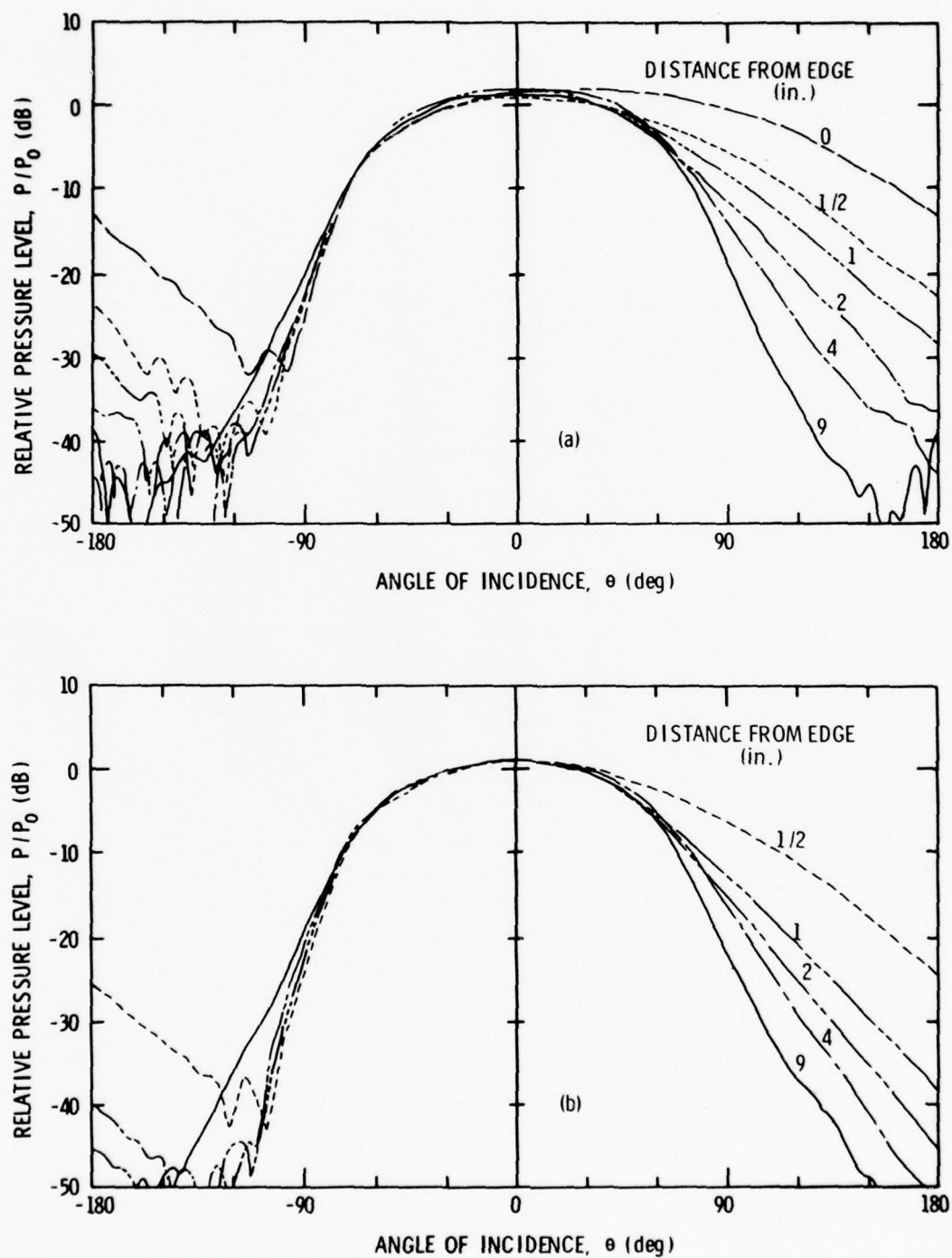


Figure 6.14 Patterns of a Hydrophone on a Soft Disk (a) and a Soft Square (b) at 20 kHz.

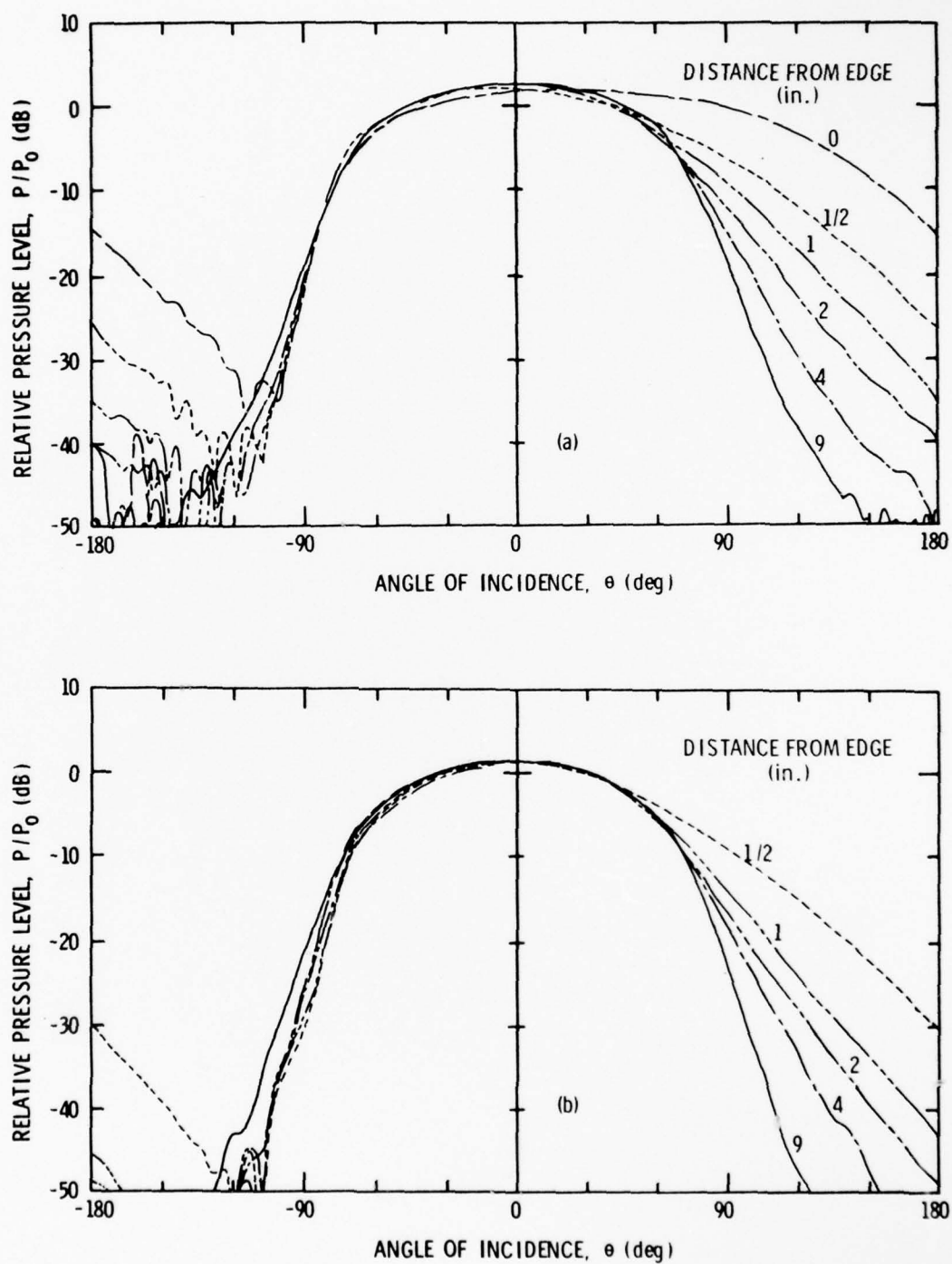


Figure 6.15 Patterns of a Hydrophone on a Soft Disk (a) and a Soft Square (b) at 30 kHz.



## 6.4 Cylindrical Baffles

### 6.4.1 Rigid End-Cap

Directivity patterns for a transducer mounted on a rigid end-cap of a cylinder, Figures 6.16 through 6.18, exhibit a ripple effect in the insonified region very similar to those obtained with the rigid baffles already discussed. The number of ripples across the main lobe and the depth or magnitude of these fluctuations increase with frequency.

Directivity patterns using a rigid end-cap on a soft cylinder, Figures 6.16(b), 6.17(b), and 6.18(b) display a low diffraction lobe level comparable to that of the soft baffles previously described. When the soft cylinder is replaced by a rigid cylinder, Figures 6.16(a), 6.17(a), and 6.18(a), the diffraction lobe level increases, as expected, being approximately 10 dB lower than those of the rigid disk and square. The major lobe is well defined and relatively independent of the impedance of the cylinder. The diffraction lobes, however, can be reduced by about 20 dB by using a soft cylinder in place of a rigid cylinder.

### 6.4.2 Soft End-Cap

Directivity patterns for a transducer mounted on a soft end-cap of a cylinder are given in Figures 6.19 through 6.21. The soft end-cap on a soft cylinder gives rise to the typical patterns obtained on soft surfaces and adds no new information to the observations presented earlier for this type of surface. The diffraction lobes are extremely low, e.g., -60 dB for the 30 kHz case. Truncation of data for some cases is due to the system noise and low signal reception.

The pattern responses with a rigid cylinder are smooth over the major lobe. Near and beyond an angle of  $90^\circ$ , however, the pattern exhibits

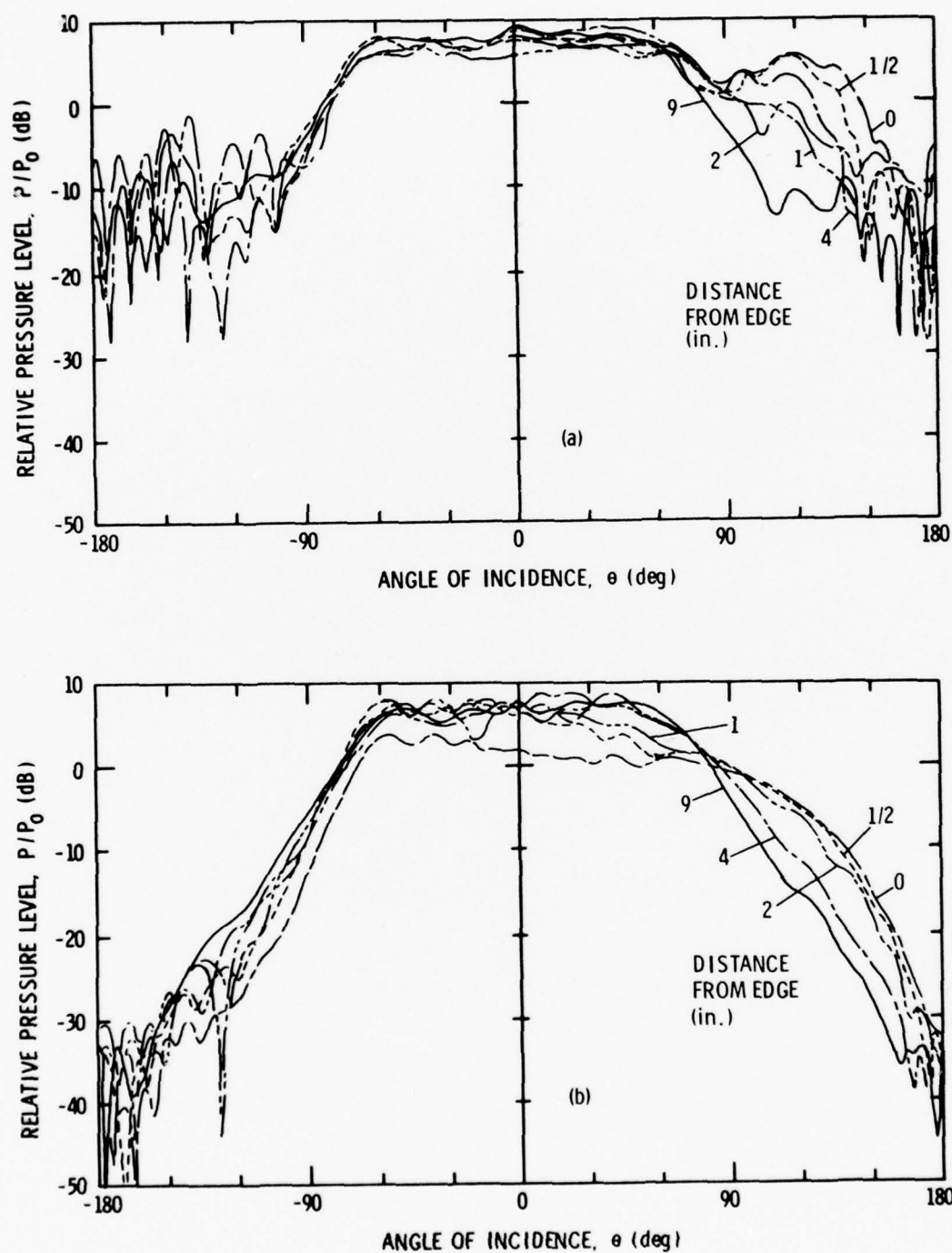


Figure 6.16 Patterns of a Hydrophone on a Rigid End-Cap with a Rigid (a) and a Soft (b) Cylinder at 15 kHz.

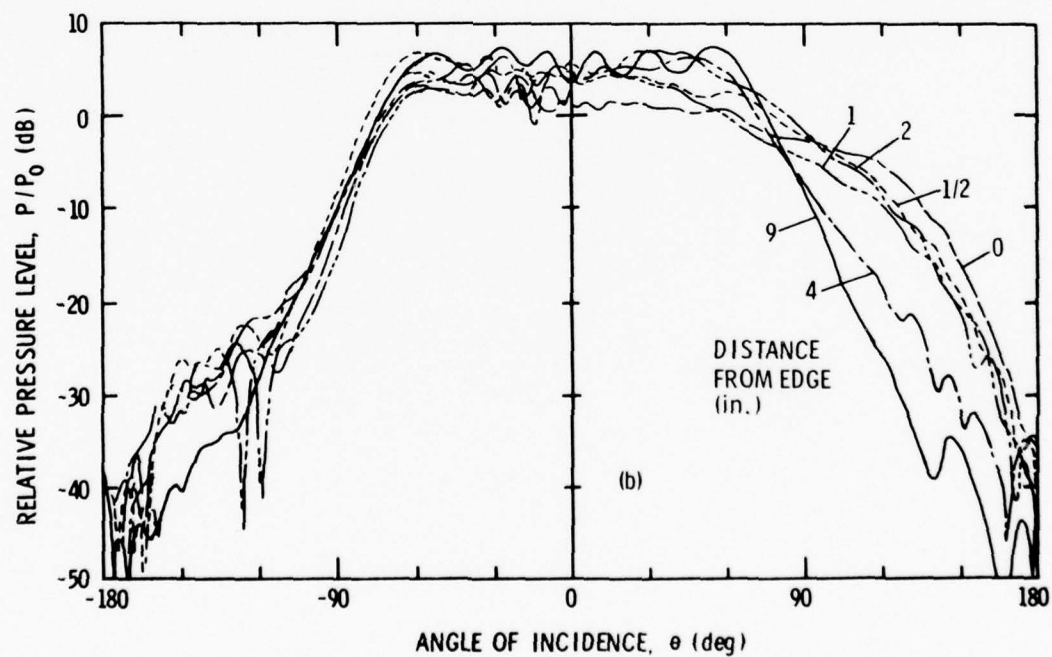
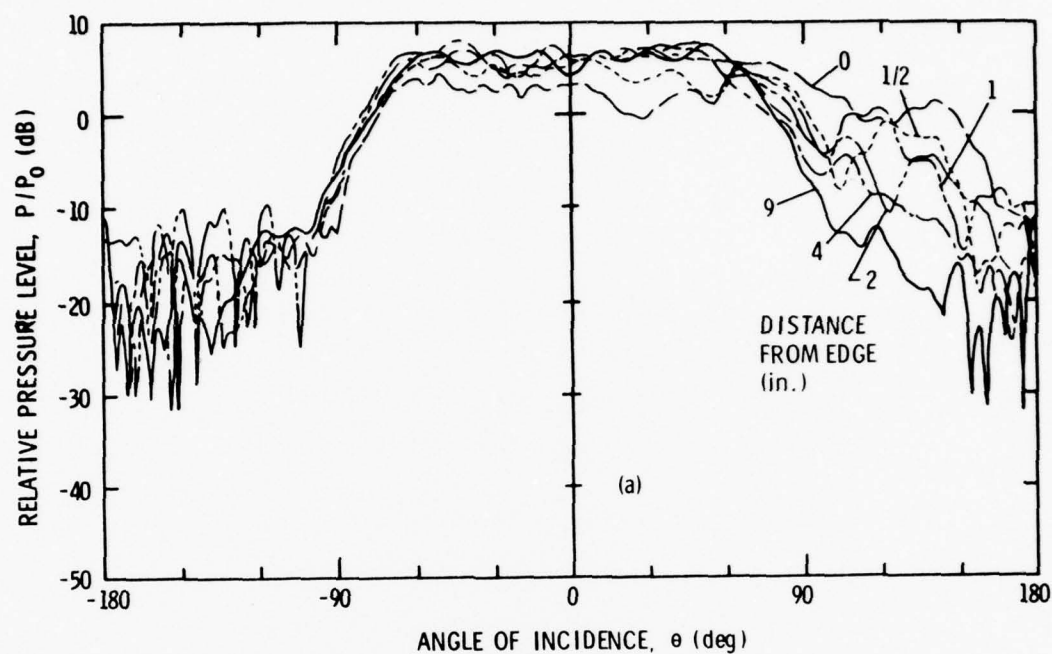


Figure 6.17 Patterns of a Hydrophone on a Rigid End-Cap with a Rigid (a) and a Soft (b) Cylinder at 20 kHz.

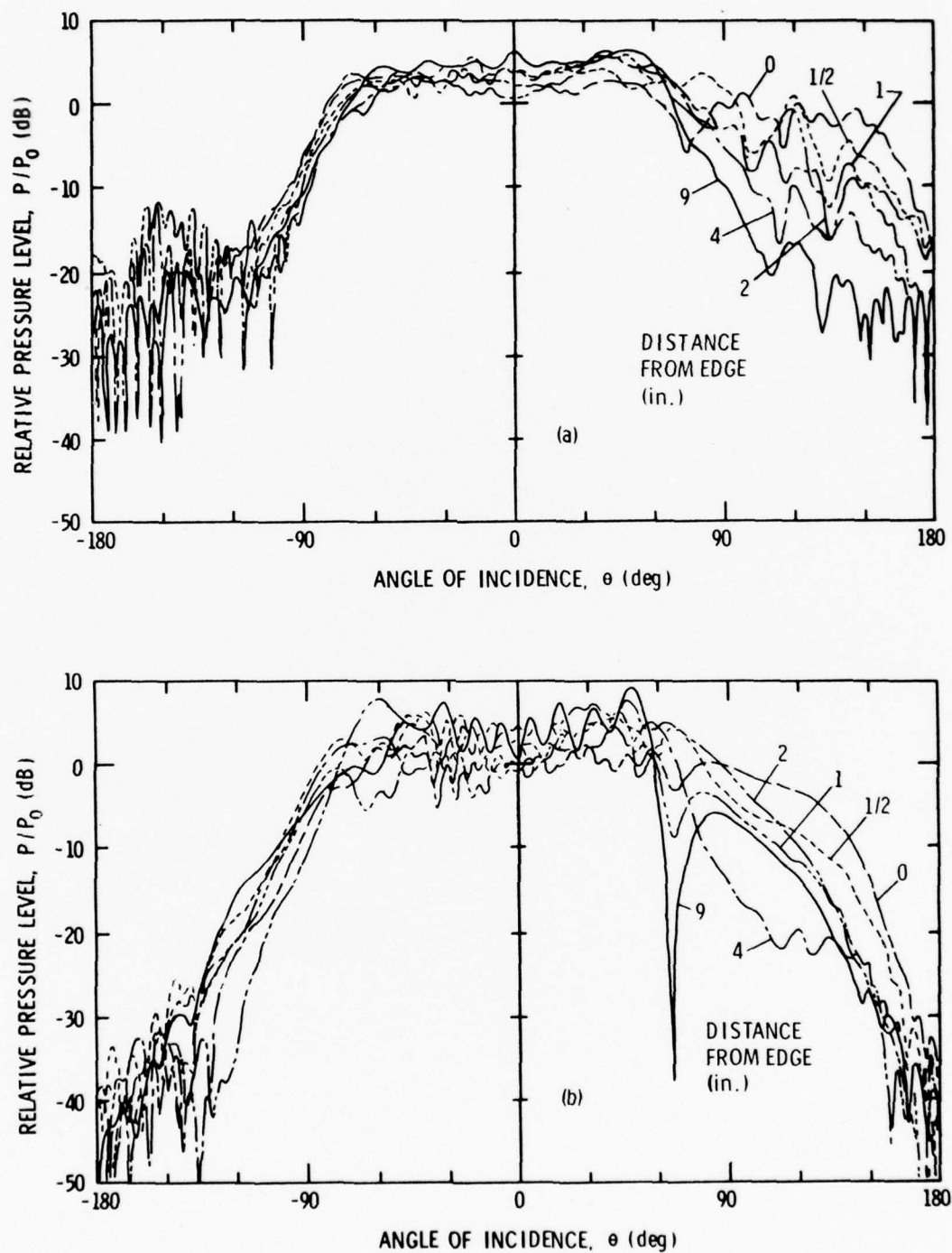


Figure 6.18 Patterns of a Hydrophone on a Rigid End-Cap with a Rigid (a) and a Soft (b) Cylinder at 30 kHz.

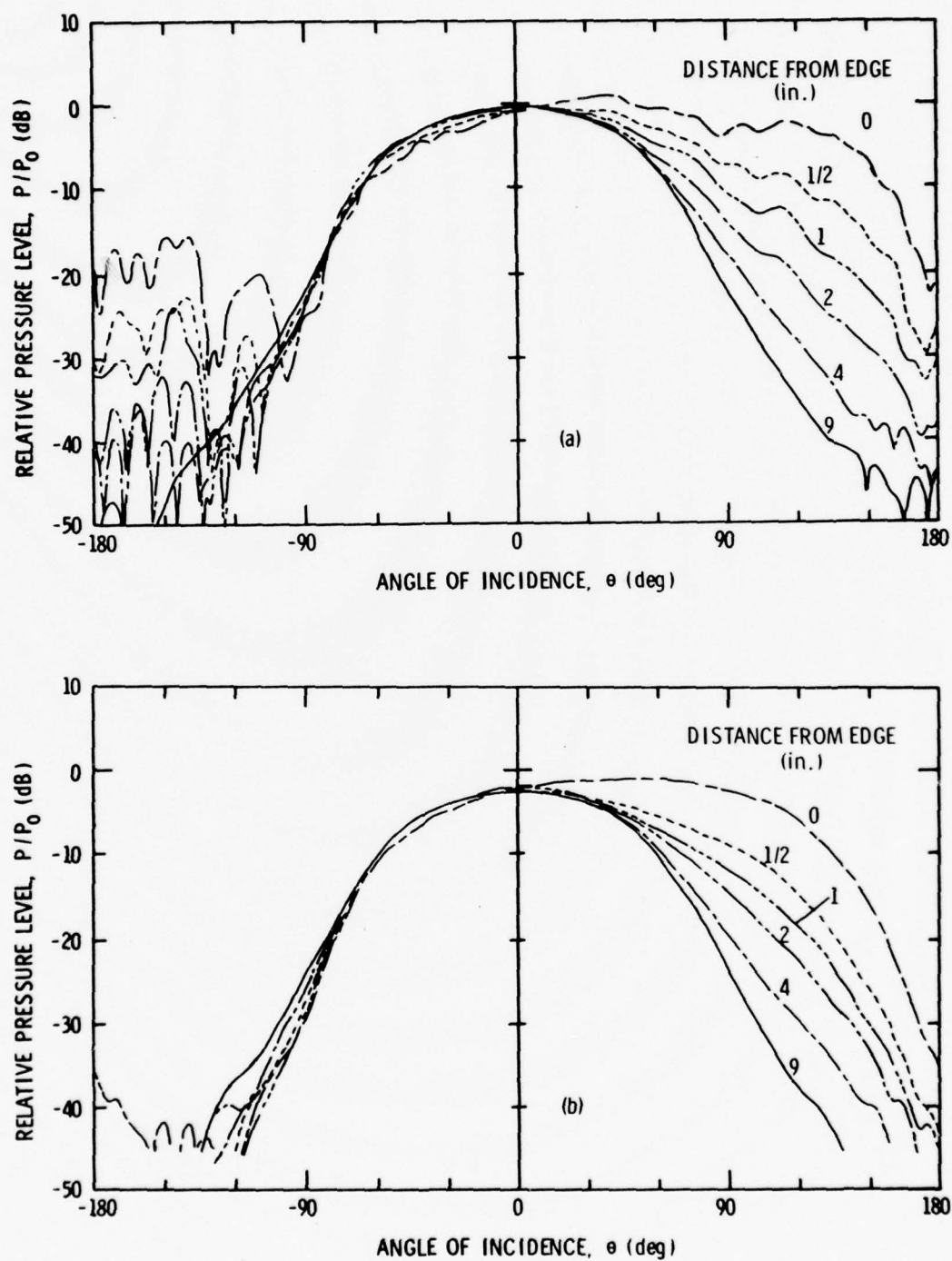


Figure 6.19 Patterns of a Hydrophone on a Soft End-Cap with a Rigid (a) and a Soft (b) Cylinder at 15 kHz.

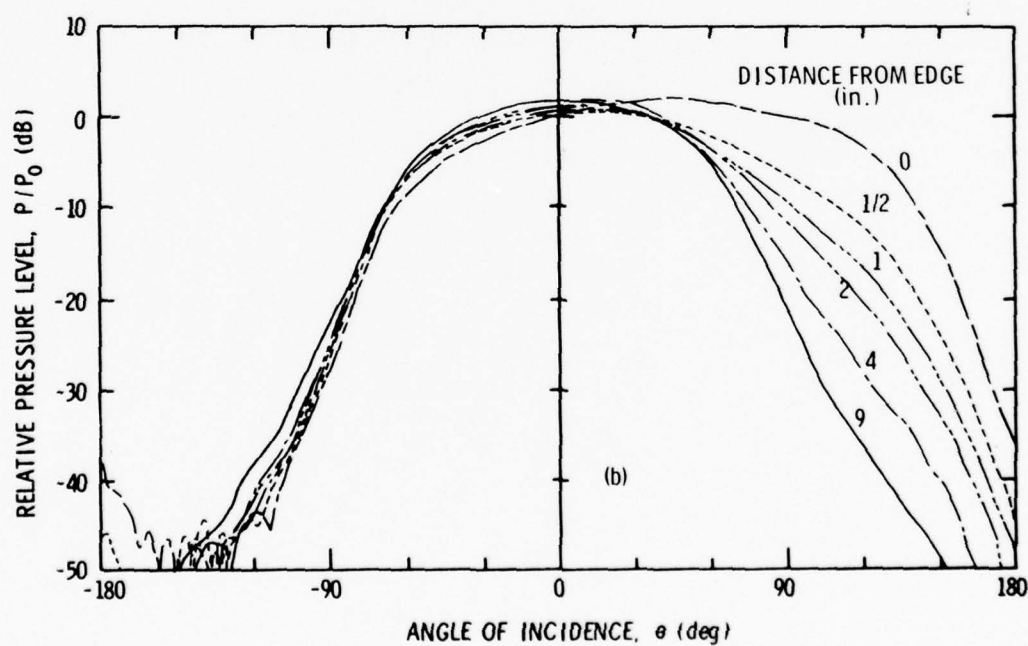
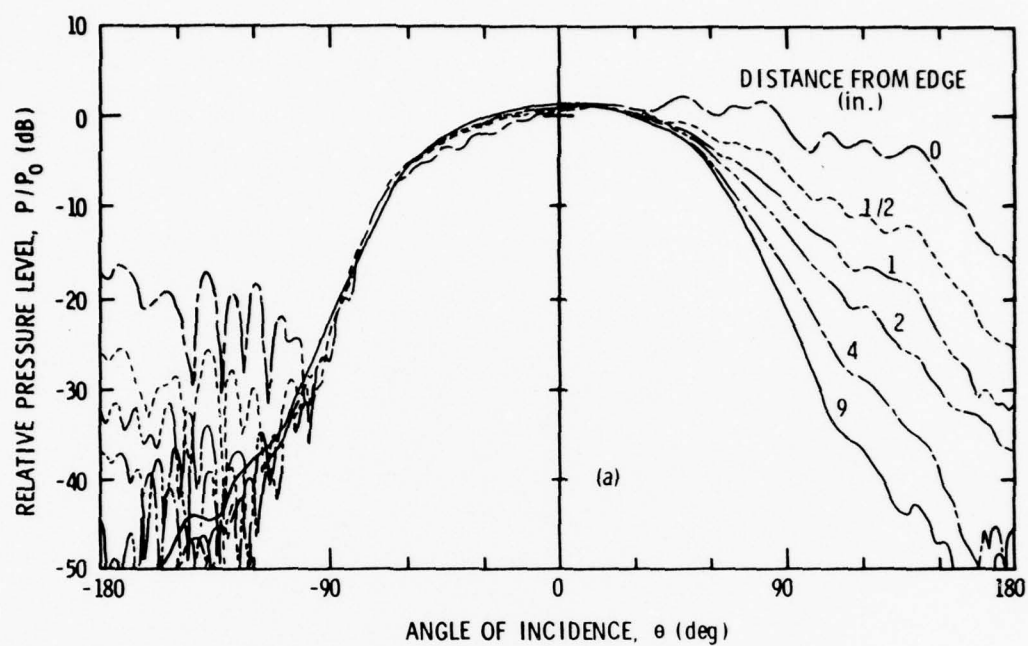


Figure 6.20 Patterns of a Hydrophone on a Soft End-Cap with a Rigid (a) and a Soft (b) Cylinder at 20 kHz.



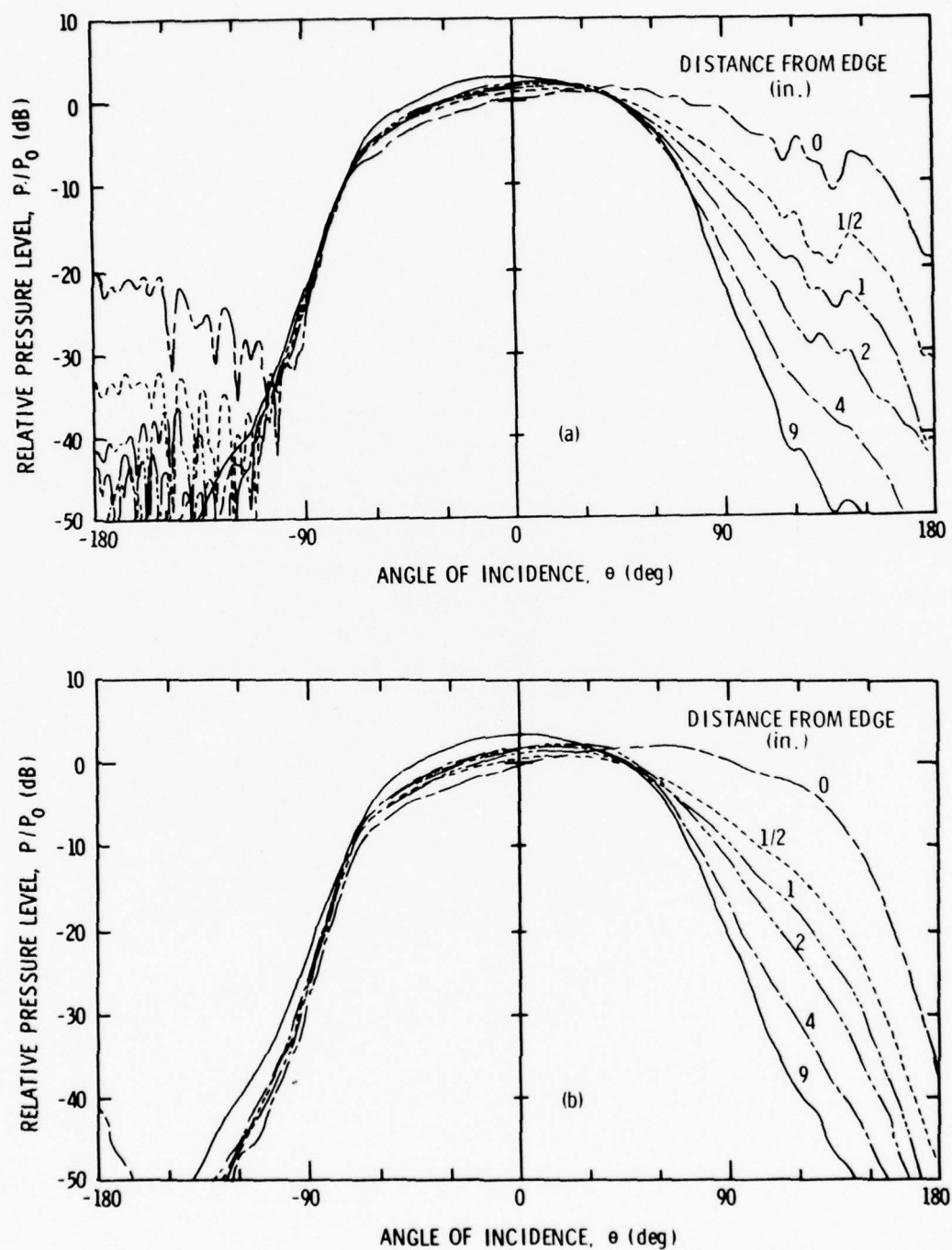


Figure 6.21 Patterns of a Hydrophone on a Soft End-Cap with a Rigid (a) and a Soft (b) Cylinder at 30 kHz.

some ripple effects which become more evident as the frequency increases, although, it should be noted that they are present only on this particular baffle. In addition, the diffraction lobe levels for the patterns obtained on the rigid cylinder are higher than those on the soft cylinder. Again, at higher frequencies, the directivity patterns have narrower major lobes.

It is observed that the baffle which has a soft end-cap and a rigid cylinder has rather high diffraction lobes when the hydrophone is moved toward the edge of the baffle. Hence, it is important that the elements in an underwater transducer array mounted on a soft end-cap and a rigid cylinder baffle are positioned at least one or two wavelengths from the edge. These diffraction lobe levels for patterns obtained with off-center mounted transducers are higher than those obtained on a rigid end-cap, soft cylinder baffle.

## 6.5 Scattering Rings on a Rigid Surface

### 6.5.1 Rigid Ring

Figures 6.22 and 6.23 show that a steel ring around the edge can produce some pattern control on the transducer when it is near the baffle edge. However, there appears to be an increase in response at other angles of incidence which may be a detriment for pattern control.

### 6.5.2 Soft Ring

One can see in Figures 6.24 and 6.25 that the transducer response in the direction of the near edge is dramatically reduced by the addition of a soft ring. However, since the entire pattern is affected, it cannot be concluded that pattern control for an array can be achieved.

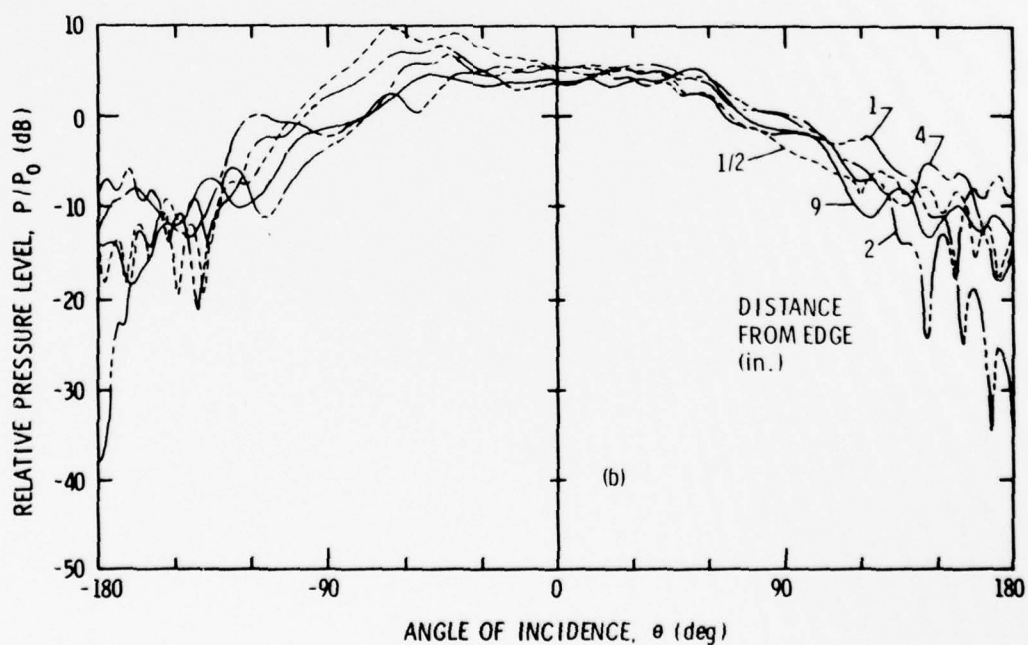
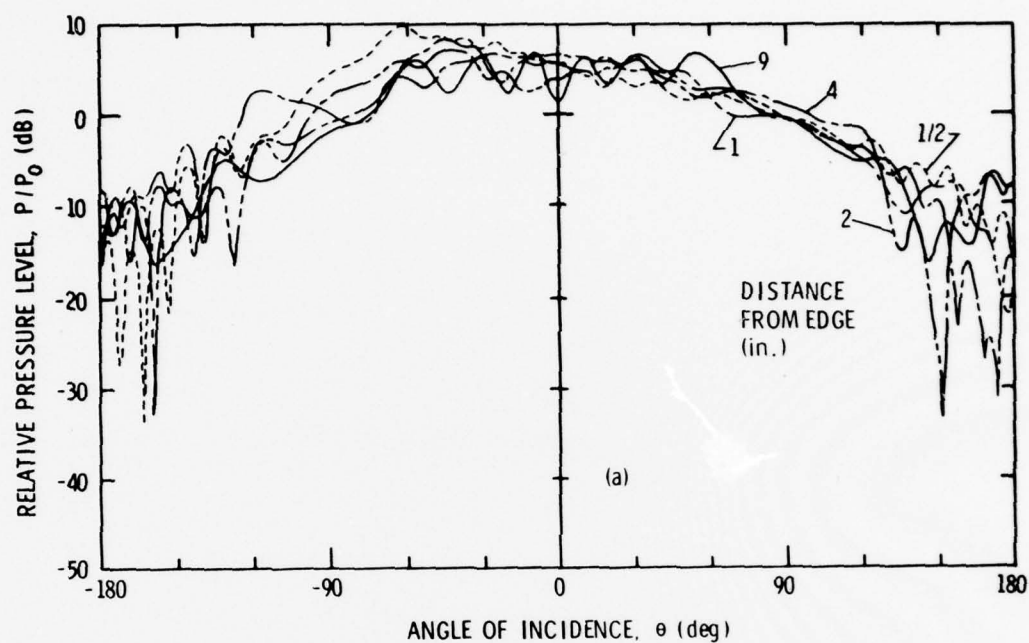


Figure 6.22 Patterns of a Hydrophone on a Rigid Disk (a) and a Rigid Square (b) with a Steel Scattering Bar at 20 kHz.

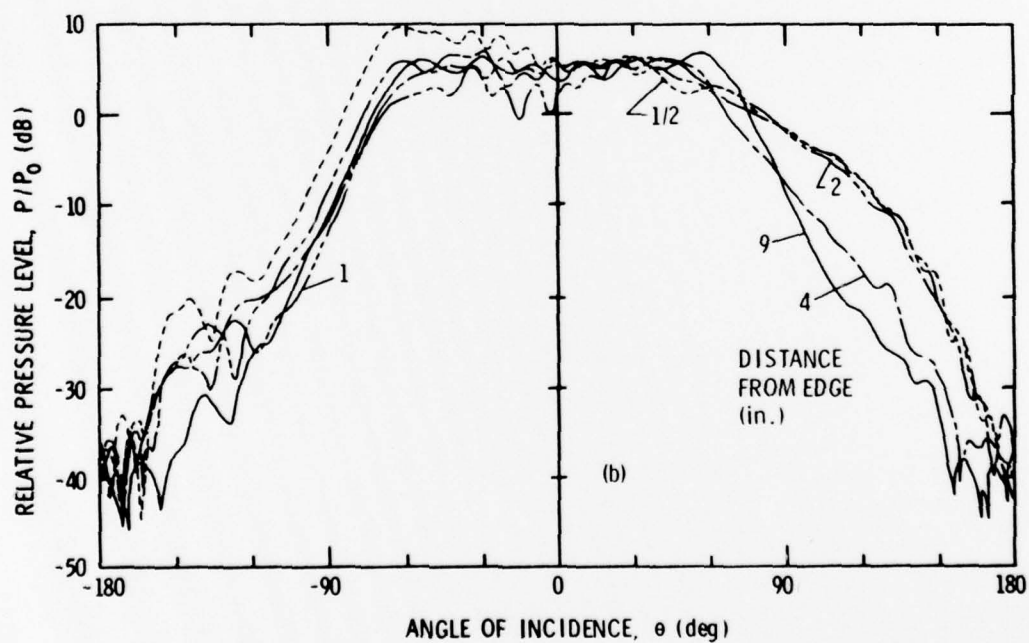
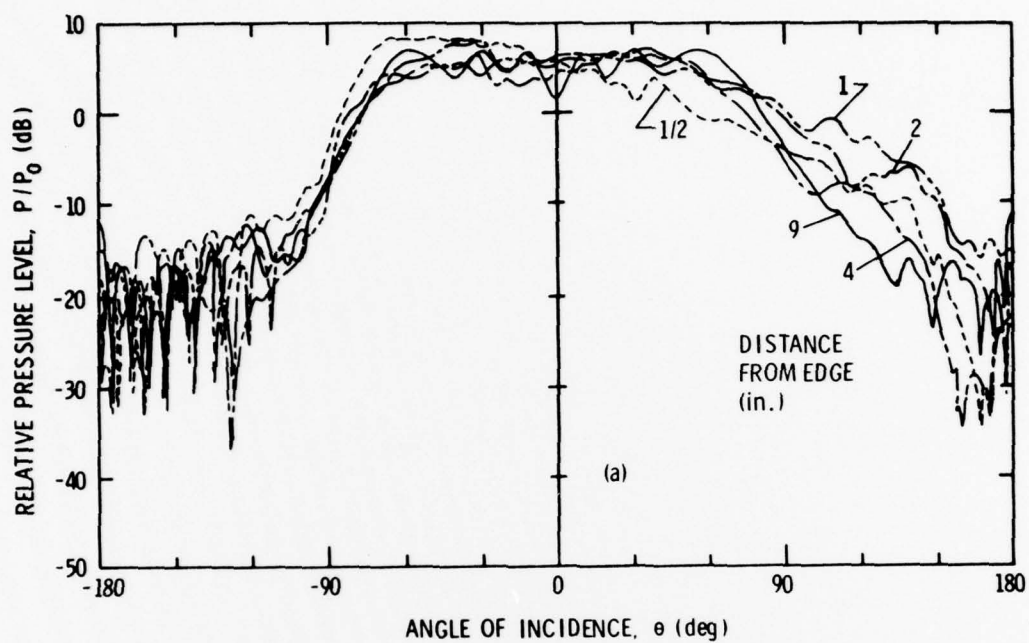


Figure 6.23 Patterns of a Hydrophone on a Rigid End-Cap on a Rigid (a) and a Soft (b) Cylinder with a Steel Scattering Ring at 20 kHz.

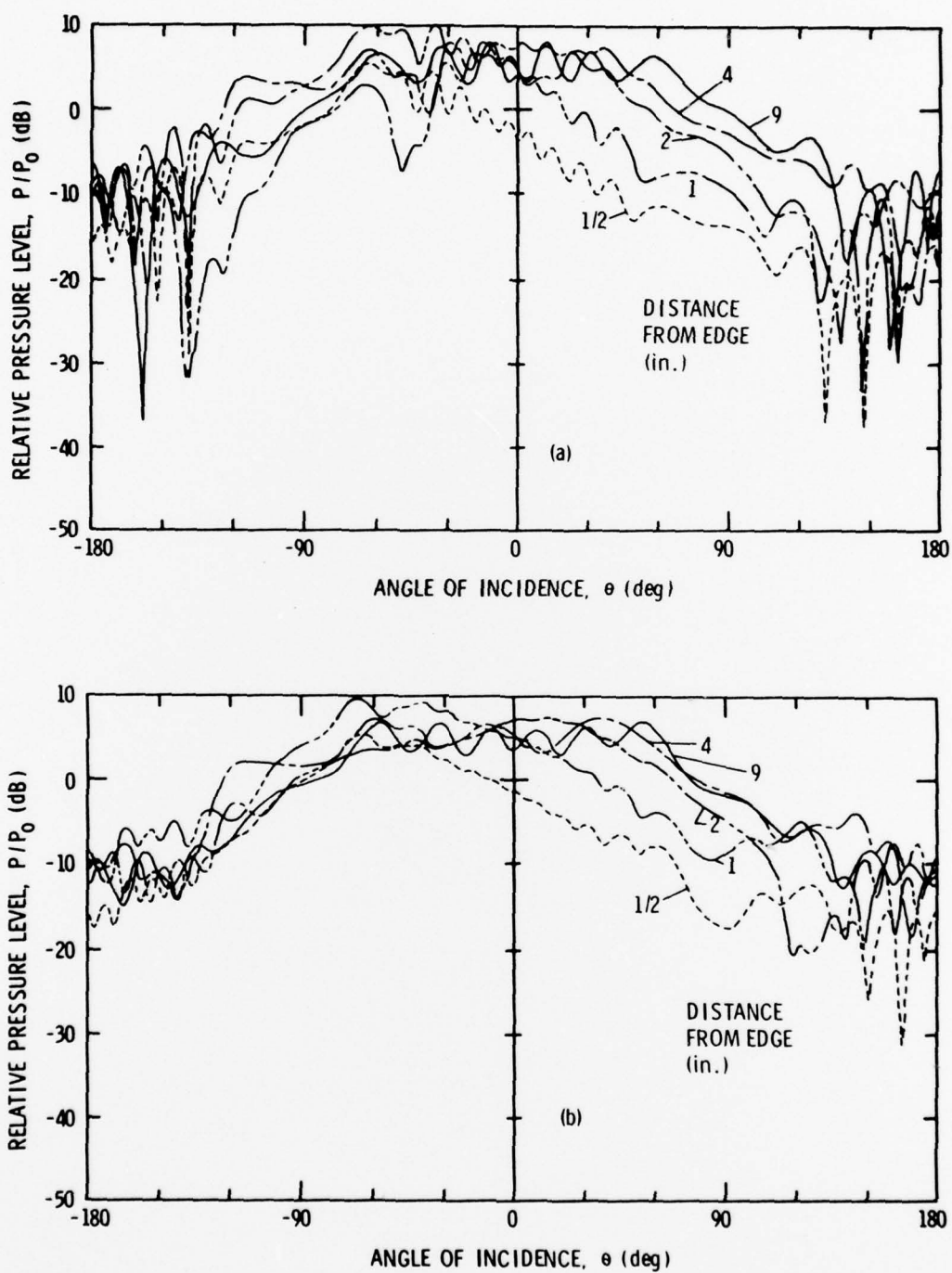


Figure 6.24 Patterns of a Hydrophone on a Rigid Disk (a) and a Rigid Square (b) with a Soft Scattering Bar at 20 kHz.



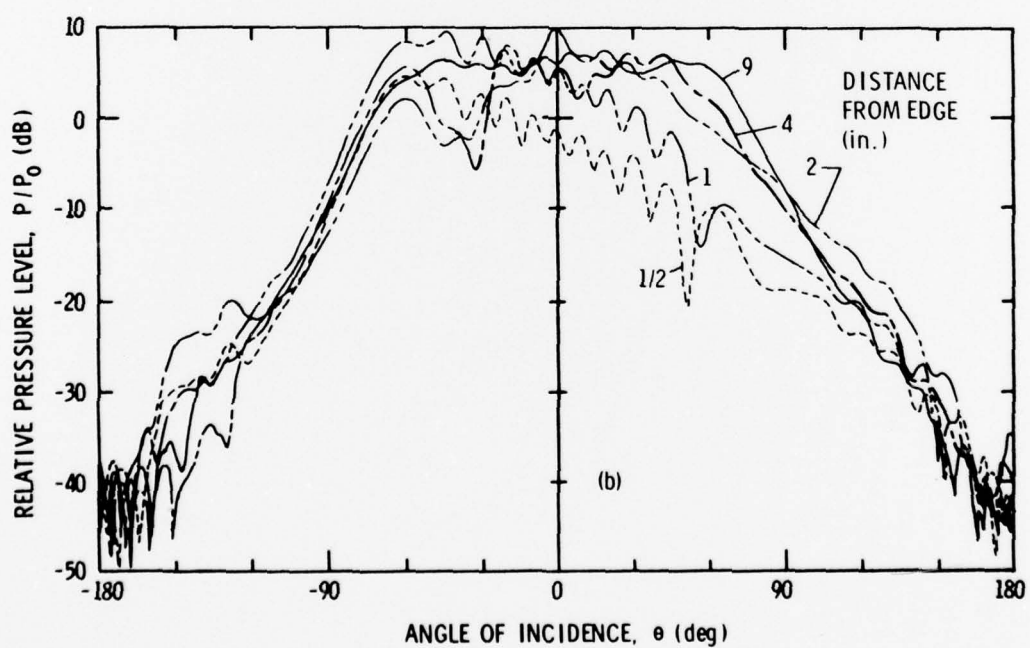
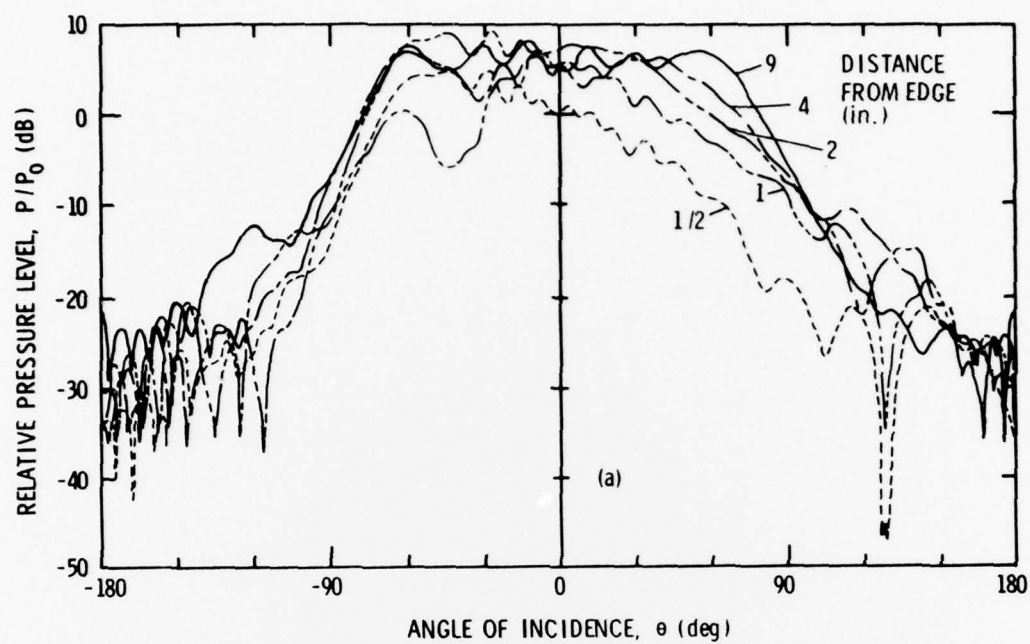


Figure 6.25 Patterns of a Hydrophone on a Rigid End-Cap with a Rigid (a) and a Soft (b) Cylinder with a Soft Scattering Ring at 20 kHz.



In Figure 6.26, the directivity patterns of a transducer  $1/2$ " from the edge of a rigid square baffle are compared with the patterns obtained when each of two impedance bars are introduced. The transducer in this position is adjacent to the bar and, as the curves indicate, the soft bar has a much more significant effect on the response of the transducer than does the rigid bar.

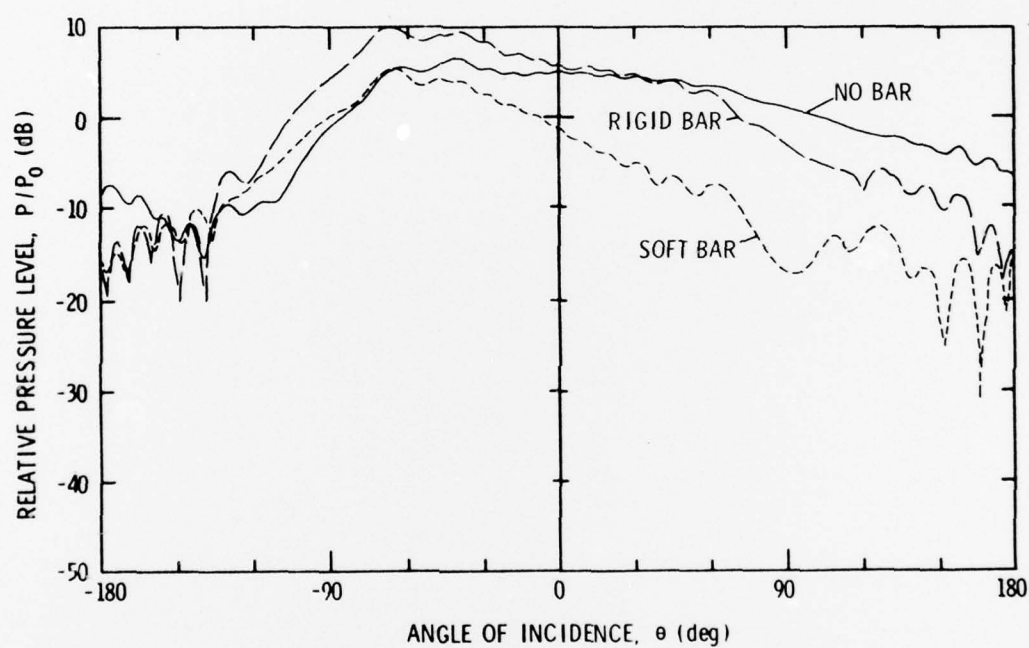


Figure 6.26 Pattern Comparisons for a Hydrophone Mounted Near a Rigid and Soft Scattering Bar on a Rigid Square.

## CHAPTER VII

### SUMMARY AND CONCLUSIONS

Distinct differences are evident between the directivity patterns obtained for a transducer mounted on a rigid surface and one mounted on a soft surface. Patterns produced using rigid baffle surfaces exhibited an interference effect, or ripples, in the insonified region. The number of ripples and their angular positions can be predicted very well by the Geometrical Theory of Diffraction. The number of ripples decrease as the frequency decreases or as the transducer is moved closer to the edge, and conversely. The transducer to edge separation distance should be expressed in wavelengths.

As expected, when a transducer is moved closer to the edge, the level of the diffracted field in the shadow region increases, producing an asymmetric pattern. Patterns generated by using a simplified theoretical model closely match the asymmetric experimental patterns, thus confirming the Geometrical Theory of Diffraction. Pattern asymmetry is analyzed more easily on a soft baffle because the low level diffraction field incident at the back surface gives the illusion of a semi-infinite baffle. Theoretical directivity patterns for the finite baffles were obtained using a two-dimensional, two-edge diffraction model, i.e., a semi-infinite strip, utilizing the Malyuzhinets diffraction coefficient. The Malyuzhinets diffraction coefficient accounts for a finite surface impedance, whereas the Sommerfeld diffraction coefficient is valid only

for rigid or soft surfaces. Whenever any case of mixed boundary conditions is present, i.e., one surface impedance differs from the other, then the Malyuzhinets diffraction coefficient must be used. The two-dimensional, two-edge diffraction model which neglects the back diffraction edges does not appear to result in a serious loss of information. Good agreement between theory and experiment is evident with the calculated patterns matching the ripples and predicting the diffraction lobe level in the shadow region, see Section 6.2.

It should be noticed, however, that the calculated and measured patterns do not match well for near grazing angles when the transducer is greater than a few wavelengths from the edge. The mismatch is not a result of diffraction theory, rather, it is a result of using a material impedance value independent of the angle of incidence. The baffle impedance depends on the angle of incidence of the acoustic field and should be taken into consideration in the calculation of directivity patterns. A method of experimentally obtaining surface impedance as a function of incidence angle is needed.

The impedance of the surface on which the transducer is located has the predominant influence on the directivity pattern. When the impedance is low, a smooth "bell-shaped" directivity pattern with a highly attenuated diffraction field will result. Hence, no ripples are present in the insonified region and very low diffraction lobe levels are present in the shadow region even if the side of the baffle is rigid. As the surface impedance increases from soft to rigid, the level of the diffracted field in the shadow region increases and an interference effect causing ripples becomes evident in the insonified region. However,

if the impedance of the surface on which the transducer is located is high or rigid, the impedance of the side of the baffle does have a pronounced effect on the diffraction lobe level. If the rigid impedance on the side of the baffle is replaced by a soft impedance, the diffraction lobe level can be lowered by as much as 20 dB. In addition to the effect on the diffraction lobe level, surface impedance affects the beamwidth of a transducer element, viz., a soft surface minimizes beamwidth while a rigid surface maximizes beamwidth. It is very important, therefore, to incorporate surface impedance into underwater transducer array or baffle design. These facts will tell a sonar designer that if a specific size baffle is used and if a wide beamwidth pattern is desired, then one should use a rigid baffle. If a narrow beamwidth with low response to the sides is desired, then a soft baffle should be used.

Scattering bars have some interesting effects on directivity patterns. The effect of a soft scatterer on the sharp edge of the impedance wedge appears to lower the diffracted field by 5 to 10 dB while increasing the interference effect in the insonified region. When the soft scatterer is placed on the cylindrical edge of the impedance wedge, the diffracted field is reduced only at a frequency where the wavelength is comparable to the radius of curvature. At higher frequencies, the patterns are not affected by the addition of the soft scatterer. With finite baffles, it was shown that the soft scattering bar has a greater effect on patterns than does the rigid scatterer. The response in the direction of the near edge is reduced, however, the entire pattern is altered so that it cannot be concluded that pattern control (elimination of pattern asymmetry) is achievable. Further study in this area of diffraction is needed.



The power of the Geometrical Theory of Diffraction has been demonstrated, in that it provides a technique of analyzing scattering from complex bodies by breaking them up into simpler forms. Although this is an approximate method for obtaining the terms dominant in acoustic scattering, it provides an insight into the physical mechanisms. When the geometry of an object is large in terms of a wavelength, as are the dimensions of the baffle investigated, then scattering and diffraction are found to be essentially local phenomena. It has also been verified that even at distances of one-third of a wavelength, the theoretically predicted diffracted field is a valid approximation.



## BIBLIOGRAPHY

1. Abramowitz, M., Stegun, I. A., Handbook of Mathematical Functions, Pub., Inc., New York, 1970, 300.
2. Barakat, R., "Diffraction of Plane Waves by an Elliptic Cylinder," J. Acoust. Soc. Am., 35, 1990-1996 (1963).
3. Batey, E. H., et al, "Some Guidelines for Sonar Baffle Designs," Report for The Bureau of Ships by Texas Research Associates, Index No. SF001-03-01, Task 8100 (1962).
4. Chen, L. H., Schweikert, D. G., "Sound Radiation from an Arbitrary Body," J. Acoust. Soc. Am., 35, 1626-1632 (1965).
5. Copley, L. G., "Fundamental Results Concerning Integral Representations in Acoustic Radiation," J. Acoust. Soc. Am., 44, 28-32 (1968).
6. Heaps, H. S., "Diffraction of an Acoustical Wave Obliquely Incident upon a Circular Disk," J. Acoust. Soc. Am., 26, 707-708 (1954).
7. Horton, C. W., Karal, F. C., "On the Diffraction of a Plane Sound Wave by a Paraboloid of Revolution," J. Acoust. Soc. Am., 22, 855-856 (1950).
8. Hutchins, D. L., "Asymptotic Series Describing the Diffraction of a Plane Wave by a Two-Dimensional Wedge of Arbitrary Angle," Ohio State University, Ph.D. Thesis, 1967.
9. Hutchins, D. L., Kouyoumjian, R. G., "Calculation of the Field of a Baffled Array by the Geometrical Theory of Diffraction," J. Acoust. Soc. Am., 45, 485-492 (1969).
10. James, G. L., Geometrical Theory of Diffraction for Electromagnetic Waves, IEE Electromagnetic Waves Series 1, Peter Peregrinus Ltd., Australia, 134-143 (1977).
11. Karp, S. N., Keller, J. B., "Multiple Diffraction by an Aperture in a Hard Screen," Optica Acta (Paris), 8, 61-72 (1961).
12. Keller, J. B., "Diffraction by a Convex Cylinder," IRE Trans. AP-4, 312-321 (1956).
13. Keller, J. B., "Diffraction by an Aperture," J. Applied Phy., 28, 426-444 (1957).

14. Keller, J. B., Lewis, R. M., Seckler, B. D., "Diffraction by an Aperture, II," J. Appl. Phys., 28, 570-579 (1957).
15. Keller, J. B., "Geometrical Theory of Diffraction," J. Optical Soc. Am., 52, 116-130 (1962).
16. Keller, J. B., Ahlywalia, D. S., "Progressive Waves Diffracted by a Smooth Surface," J. Math. and Mech., 19, 515-530 (1969).
17. Kouyoumjian, R. G., Burnside, W. D., "The Diffraction by a Cylinder-Tipped Half-Plane," IEEE Trans. Ant. and Prop., 424-426 (1970).
18. Kouyoumjian, R. G., Hutchins, D. L., Notes on the Field of a Baffled Array, private communication.
19. Kouyoumjian, R. G. Pathak, P. H., "A Uniform Geometrical Theory of Diffraction for an Edge in a Perfectly Conducting Surface," Proc. IEEE, 62, 1448-1461 (1974).
20. Lamb, G. L., Jr., "Diffraction of a Plane Wave by a Semi-Infinite Thin Elastic Plate," J. Acoust. Soc. Am., 31, 929-935 (1959).
21. Leitner, A., "Diffraction of Sound by a Circular Disk," J. Acoust. Soc. Am., 21, 331-334 (1949).
22. Leizer, I. G., "Applicability of the Methods of Geometric Acoustics for the Calculation of Sound Reflection from Plane Surfaces," Soviet Phys. Acoust., 12, 180-184 (1966).
23. Levitas, A., Lax, M., "Scattering and Absorption by an Acoustic Strip," J. Acoust. Soc. Am., 23, 316-322 (1951).
24. Levy, B. R., Keller, J. B., "Diffraction by a Smooth Object," Commun. on Pure and Appl. Math., XII, 159-209 (1959).
25. Lewis, R. M., Boersma, J., "Uniform Asymptotic Theory of Edge Diffraction," J. Math. Phys., 10, 2291-2305 (1969).
26. Lyamshev, L. M., "Sound Diffraction by a Semi-Infinite Elastic Plate in a Moving Medium," Soviet Phys. Acoust., 12, 291-294 (1967).
27. Malyuzhinets, G. D., "Developments in Our Concepts of Diffraction Phenomena (On the 130th Anniversary of the Death of Thomas Young)," Soviet Phys. Uspekhi, 69(2), 749-758 (1959).
28. Malyuzhinets, G. D., "Excitation, Reflection and Emission of Surface Waves from a Wedge with Given Face Impedances," Doklady, 3, 752-755 (1958).
29. McLachlan, N. W., Bessel Functions for Engineers, Oxford Un. Press, London, 55-57 (1961).

30. Morse, P. M., Feshbach, H., Methods of Theoretical Physics, Part I, McGraw Hill Bk. Co., New York, 655 (1953).
31. Officer, C. B., Introduction to the Theory of Sound Transmission, McGraw Hill, Inc., New York, 218-227 (1958).
32. Pauli, W., "On Asymptotic Series for Functions in the Theory of Diffraction of Light," Phys. Rev., 54, 924-931 (1938).
33. Popov, A. V., "Numerical Solution of the Problem of Plane Wave Diffraction of the Rounded Edge of a Semi-Infinite Plate," Soviet Phys. Acoust., 14, 527 (1969).
34. Primakoff, H., Klein, M. J., Keller, J. B., Garstensen, E. L., "Diffraction of Sound Around a Circular Disk," J. Acoust. Soc. Am., 19, 132-142 (1947).
35. Sakharova, M. P., "Influence of the Edge of a Wedge with Vibrating Faces on the Radiated Acoustic Power," Soviet Phys. Acoust., 12, 60-66 (1966).
36. Schenck, H. A., "Improved Integral Formulation for Acoustic Radiation Problems," J. Acoust. Soc. Am., 44, 41-58 (1968).
37. Seckler, B. D., Keller, J. B., "Geometrical Theory of Diffraction in Inhomogeneous Media," J. Acoust. Soc. Am., 31, 192-205 (1959).
38. Seckler, B. D., Keller, J. B., "Asymptotic Theory of Diffraction in Inhomogeneous Media," J. Acoust. Soc. Am., 31, 206-216 (1959).
39. Skydrzyk, E. J., The Foundations of Acoustics, Springer-Verlag, Wein (1971).
40. Spence, R. D., "The Diffraction of Sound by Circular Disks and Apertures," J. Acoust. Soc. Am., 20, 380-386 (1948).
41. Spence, R. D., "A Note on the Kirchhoff Approximation in Diffraction Theory," J. Acoust. Soc. Am., 21, 98-100 (1949).
42. Spence, R. D., Granger, S., "The Scattering of Sound from a Prolate Spheroid," J. Acoust. Soc. Am., 23, 701-706 (1951).
43. Subroutine CS, IBM System/360 Scientific Subroutine Package, Version III, Form GH20-0205-4, 371 (1970).
44. Twersky, V., "On the Non-Specular Reflection of Plane Waves of Sound," J. Acoust. Soc. Am., 22, 539-546 (1950).
45. Twersky, V., "On the Non-Specular Reflection of Sound from Planes with Absorbent Bosses," J. Acoust. Soc. Am., 23, 336-338 (1951).
46. Wiener, F. M., "Sound Diffraction by Rigid Spheres and Circular Cylinders," J. Acoust. Soc. Am., 19, 444-451 (1957).

47. Wiener, F. M., "Notes on Sound Diffraction by Rigid Circular Cones," J. Acoust. Soc. Am., 20, 367-369 (1948).
48. Wiener, F. M., "The Diffraction of Sound by Rigid Disks and Rigid Square Plates," J. Acoust. Soc. Am., 21, 334-347 (1949).
49. Wiener, F. M., "On the Relation Between the Sound Fields Radiated and Diffracted by Plane Obstacles," J. Acoust. Soc. Am., 23, 697-700 (1951).
50. Williams, W. E., "Diffraction by a Disk," Procs. Royal Soc., 267, No. 1328, 77-87 (1962).

DISTRIBUTION

Commander (NSEA 09G32)  
Naval Sea Systems Command  
Department of the Navy  
Washington, D. C. 20362

Copies 1 and 2

Commander (NSEA 0342)  
Naval Sea Systems Command  
Department of the Navy  
Washington, D. C. 20362

Copies 3 and 4

Defense Documentation Center  
5010 Duke Street  
Cameron Station  
Alexandria, VA 22314

Copies 5 through 16